# Calcium carbonate colloidal particles as delivery vehicles to biological systems

Vom Fachbereich Produktionstechnik

der

**UNIVERSITÄT BREMEN**

zur Erlangung des Grades

**Doktor-Inginieur**

genehmigte

Dissertation

von

**Dipl.-Ing. Victor Rafael Lauth**

Gutachter:

Prof. Dr.-Ing. Kurosch Rezwan

Prof. Dr.-Ing. Lutz Mädler

Tag der mündlichen Prüfung: 19.10.2017

To my wife and family.

## Contents

## Summary

Colloidal systems are increasingly being used in consumer products. Special interest is drawn to their application as delivery vehicles. To this end, there is the need of novel synthesis methods to produce colloids with tailored size and morphology in absence of harsh conditions and toxic constituents. One exceptional material for such purposes is calcium carbonate ($CaCO_3$), as it can be synthesized in mild conditions besides being endogenous to the body, safe, biodegradable and biocompatible. Yet, there are still limitations that could hinder its use as a viable delivery system, e.g. shortcomings regarding the morphological and size control, the particle instability in aqueous solutions as well as in the sustained release of encapsulated molecules. In this thesis, these aspects are studied in detail and new strategies are explored for the preparation of suitable colloidal carriers with biocompatible cellular interactions. To this purpose, distinct principles that govern biomineralization and complex coacervation are translated to synthetic systems and assessed in vitro by means of monoculture cellular experiments. These principles include: (1) the use of charged proteins and polymers as the assembling components during the complex coacervation; (2) the use of polyelectrolytes molecules to direct the mesoscale assembly of anisotropic nanoparticles; and (3) the study on how the physical and colloidal properties of $CaCO_3$ systems can control particle-cellular interactions.

The first project studied a combination of complex coacervation and $CaCO_3$ mineralization to produce pH-responsive microcarriers loaded with proteins. Complex coacervation is a phenomenon that occurs when two or more oppositely charged molecules (e.g. negatively-charged poly(acrylic acid) (PAA) and $Ca^{2+}$ ions) form electrostatic complexes in aqueous solution. In this case, the complexation leads to the phase separation of fluid-like coacervate droplets, which are subjected to coalescence and growth. Accordingly, the size of these droplets increases with complexation time. By the addition of sodium carbonate, the droplets are mineralized into stable, amorphous $CaCO_3$ microcarriers. It is hypothesized that charged proteins could also comprise one of the assembling components of the complex coacervate droplets. For that purpose, both positively-charged lysozyme (LSZ) and negatively-charged bovine serum albumin (BSA) are added to the coacervation reaction and their encapsulation and release behavior are assessed. It is shown that positively-charged LSZ strongly binds to the coacervate droplets due to electrostatic attraction, which disturbs the coalescence and growth processes and limits the control of particle size. This results in highly-loaded $CaCO_3$ particles in the micrometer range. On the other hand, negatively-charged

BSA is barely encapsulated due to repulsive forces between BSA molecules and coacervate droplets. As a consequence of low BSA-PAA coordination, the particle size of BSA-loaded carriers is similar to the unloaded ones.

In a second approach, a platform for the synthesis of functional hybrid nanoparticles with tailorable morphology is described based on the controlled mesoscale self-assembly process. In this study, the precipitation of $CaCO_3$ primary nanoparticles can be modulated by the presence of highly-carboxylated carbon dot nanoparticles (CDs). At higher particle concentration, the calcium supersaturation is lowered due to carboxyl-calcium coordination, which avoids the precipitation of microsized crystals in aqueous solution. Moreover, it is shown that the high density of carboxylic groups on the CD surface sequestered enough calcium ions to serve as templates for heterogeneous $CaCO_3$ precipitation. These primary particles afterwards self-assemble into spheres or rods depending on the PAA concentration. At increasing polymer concentration, oriented assembly becomes more prevalent yielding rod-like particles. The hybrid particles show colloidal stability in cell medium and absence of cytotoxicity towards adenocarcinomic cells. Moreover, due to the particles porosity, Rhodamine B can be encapsulated and the release triggered by adjusting the environmental pH.

Besides the two mentioned methods to control size, crystallinity and morphology of calcium carbonate carriers, the understanding of cellular interaction also plays an important role in the design of drug delivery vehicles. The high solubility of $CaCO_3$ in aqueous solutions can hinder its use as a novel delivery system. These particles are shown to either readily dissolve or to phase-transition into more stable phases depending on the ionic strength of the medium, on particle size and on crystallinity. In order to understand how the physical properties, like size, morphology and crystallinity can influence the phase stability and cellular response, four calcium carbonate particle systems commonly described in the literature are assessed with regard to colloidal stability, phase transformation, cytotoxic effects and cellular internalization. In this study, the calcite nanoparticles maintain the morphological features as no phase transformation occurs within the timeframe of the experiments. However, the vaterite particles transform to calcite phase in cell culture medium. This transition is shown to be size-depend and can be effective hindered by supplementing the medium with the protein serum albumin. In regard to the dissolution behavior, the amorphous phase is the only one affected, being more pronounced in the presence of amino acids and phosphate ions. In addition to the stability experiments, the cellular responses against human osteoblasts indicate that increased extracellular and intracellular calcium concentration can improve the cellular viability as well as shows that particle internalization can occur within 24 hours for a large range of particle sizes.

In conclusion, this thesis focuses on the use of essential biomineralization concepts aiming to prepare $CaCO_3$-based delivery vehicles with appropriate size and morphology. The studies focused on the loading ability, colloidal and crystal phase stability as well as cellular outcome. In a general way, the results presented here are of high interest to researchers focused on the aqueous-based synthesis of $CaCO_3$ particles, in the in vitro cellular interactions of $CaCO_3$ and in the design of biodegradable delivery vehicles with improved cellular uptake and viability.

## Zusammenfassung

Kolloidale Systeme werden zunehmend in Konsumgütern eingesetzt. Dabei ist die Anwendung als Wirkstoffträger von besonderem Interesse. Zu diesem Zweck ist die Entwicklung von neuartigen Syntheseverfahren notwendig, mit welchen Kolloide mit maßgeschneiderter Größe und Morphologie in Abwesenheit von harten Bedingungen und Schadstoffen produziert werden können. Ein vielversprechendes Material für solche Zwecke ist Calciumcarbonat ($CaCO_3$), da es unter milden Bedingungen synthetisiert werden kann und für den Körper endogen ist. Weiterhin ist es sicher, biologisch abbaubar und biokompatibel. Dennoch gibt es noch Einschränkungen bezüglich der morphologischen Kontrolle von Partikeln, in der Partikel-Instabilität in wässrigen Lösungen sowie in der Beladungs- und Freisetzungskapazität, die die Verwendung von $CaCO_3$ Nanopartikeln erschwerenkönnten. In dieser Arbeit werden diese Aspekte detailliert untersucht und neue Strategien zur Herstellung geeigneter kolloidaler Träger mit biokompatiblen zellulären Wechselwirkungen untersucht. Dazu werden verschiedene Prinzipien, welche die Biomineralisierung und die komplexe Koazervation bestimmen, in synthetischen Systeme umgesetzt und in vitro beurteilt werden. Diese Prinzipien beinhalten: (1) die Verwendung von geladenen Proteinen und Polymeren als Bausteine während der komplexen Koazervation; (2) die Verwendung von Polyelektrolytmolekülen, um die mesoskalige Anordnung von anisotropen Bausteinen zu leiten; und (3) die Studie darüber, wie die physikalischen und kolloidalen Eigenschaften der $CaCO_3$ Systeme Wechselwirkungen zwischen Partikeln und Zellen kontrollieren.

Das erste Projekt nutzt eine Kombination aus komplexer Koazervation und $CaCO_3$-Mineralisierung, um pH-responsive Mikroträger zu produzieren, die mit Proteinen beladen sind. Komplexe Koazervation ist ein Phänomen, das auftritt, wenn zwei oder mehr entgegengesetzte geladene Moleküle (z. B. negativ geladene Poly(acrylsäure) (PAA) und $Ca^{2+}$-Ionen) elektrostatische Komplexe in wässriger Lösung bilden. In diesen Fällen führt die Bildung von Komplexen zur Phasentrennung von flüssigkeitsähnlichen Koazervat-Tröpfchen, die einer Koaleszenz und einem Wachstum ausgesetzt sind. Dementsprechend nimmt die Größe der Tröpfchen mit der Komplexierungszeit zu. Durch die Zugabe von Natriumcarbonat werden diese Tröpfchen zu stabilen, amorphen $CaCO_3$-Mikroträgern mineralisiert. Es wird vermutet, dass geladene Proteine auch eine der Zusammenbaukomponenten der komplexen Koazervat-Tröpfchen enthalten können. Zu diesem Zweck werden sowohl positiv geladenes Lysozym (LSZ) als auch negativ geladenes Rinderserumalbumin (BSA) der Koazervierungsreaktion

zugegeben und deren Einkapselungs- und Freisetzungsverhalten beurteilt. Es zeigt sich, dass positiv geladenes LSZ aufgrund der elektrostatischen Anziehung stark an die Koazervattröpfchen bindet und damit den Koaleszenz- und Wachstumsprozess stört. Dies führt zu hochbelasteten, großen $CaCO_3$-Partikeln mit minimaler Kontrolle über die Größe. Andererseits ist das negativ geladene BSA aufgrund von Abstoßungskräften zwischen dem geladenen Protein und den Koazervat-Tröpfchen kaum eingekapselt. Als Folge der geringen BSA-PAA-Koordination wird die Partikelgröße von BSA-beladenen Trägern in ähnlicher Weise durch die Komplexierungszeit gesteuert.

In einem weiteren Forschungsansatz wird eine Plattform für die Synthese von funktionellen Hybrid-Nanopartikeln mit maßgeschneiderter Morphologie basierend auf der Kontrolle über die mesoskalige Assemblierung beschrieben. Dafür kann die Ausfällung von $CaCO_3$-Primärnanopartikeln durch die Anwesenheit von hochcarboxylierten Kohlenstoff-Dot-Nanopartikeln (CDs) moduliert werden. Bei höherer Konzentration können diese Partikel die Übersättigung von $CaCO_3$ aufgrund der Carboxyl-Calcium-Koordination senken, was die Ausfällung von mikroskopischen Kristallen in wässrigen Lösungen vermeidet. Darüber hinaus wird gezeigt, dass die hohe Dichte der Carboxylgruppen auf den CD-Oberflächen genügend Calciumionen bindet, um als Templat für die $CaCO_3$-Ausfällung zu dienen, wenn Carbonat zugegeben wird. Diese Primärteilchen assoziieren sich anschließend in Abhängigkeit von der PAA-Konzentration in Kugeln oder Stäbchen. Bei zunehmender Polymerkonzentration dominiert die orientierte Assemblierung, wobei stabförmige Partikel erzeugt werden. Die Hybridpartikel zeigen hohe kolloidale Stabilität im Zellmedium und die Abwesenheit von Zytotoxizität gegenüber Adenokarzinomzellen. Darüber hinaus kann aufgrund der Partikel-Porosität Rhodamin B eingekapselt werden und die Freisetzung durch Anpassung der Umgebungen pH-Wert ausgelöst werden.

Neben den beiden genannten Methoden zur Kontrolle der Größe, der Kristallinität und der Morphologie von Calciumcarbonat-Trägern spielt das Verständnis der zellulären Wechselwirkung eine wichtige Rolle bei der Gestaltung von Wirkstoffträgern. Eine intrinsische Eigenschaft von $CaCO_3$, die ihre Verwendung als Trägersystem behindern kann, hängt mit ihrer Löslichkeit in wässrigen Medien zusammen. Hier wird gezeigt, dass $CaCO_3$-Partikelsich leicht lösen oder eine Phasenumwandlung eingehen hinzu stabileren Phasen in Abhängigkeit von der Ionenstärke des Mediums, der Teilchengrße und der Kristallinität. Um zu verstehen, wie $CaCO_3$-Eigenschaften wie Größe, Morphologie und Kristallinität die kolloidale Stabilität und zelluläre Reaktion beeinflussen können, werden vier oft genutzte Calciumcarbonat-Partikelsysteme, die in der Literatur bereits eingehend beschrieben werden, hinsichtlich der kolloidalen Stabilität,

Phasentransformation, zytotoxischen Effekte und zellulärer Internalisierung beurteilt. Die Calcit-Nanopartikel (90 nm) behalten die morphologischen Merkmale bei, da keine Phasenumwandlung innerhalb des Zeitrahmens der Experimente stattfindet. Allerdings verwandeln sich Vateritpartikel innerhalb von 96 Stunden in Zellkulturmedium zu Calcit. Dies trat bei den 600 nm Partikeln auf, aber nicht für die 1 µm Vateritpartikel und kann durch die höhere Oberfläche und Reaktivität der kleineren Partikel erklärt werden. Darüber hinaus wird gezeigt, dass der Phasenübergang durch die Ergänzung des Mediums mit dem Protein Serumalbumin wirksam verhindert wird. Die Auflösung von amorphen Partikeln ist in Zellmedium mit höherer Ionenstärke stärker ausgeprägt, im Gegensatz zu in Millipore-Wasser. Hier erhöhen Aminosäuren und Phosphatsalze, welche sich im Zellmedium befinden, wahrscheinlich die Auflösungsrate von weniger stabiler $CaCO_3$-Phasen. Die zellulären Reaktionen von menschlichen Osteoblasten gegenüber $CaCO_3$-Partikel zeigen, dass eine erhöhte extrazelluläre Calcium-Konzentration die Zellviabilität erhöht.

Diese Arbeit beschäftigt sich somit mit der Umsetzung grundlegender Konzepte im Zusammenhang mit der Biomineralisierung in der Synthese von $CaCO_3$-basierten Wirkstoffträgern mit kontrollierter Größe, Morphologie, Beladung sowie kolloidaler Stabilität und Stabilität der Kristallphase. Die dargestellten Ergebnisse sind für Forscher von besonderem Interesse, die sich auf die Einkapselung und Freisetzung von Arzneimitteln oder anderen bioaktiven Molekülen konzentrieren, und allgemeiner in der wässrigen Synthese von anorganischen Partikeln mit maßgeschneiderter Anisotropie. Darüber hinaus liefern die Ergebnisse der in vitro-Assessments Einblicke in zelluläre Wechselwirkungen mit $CaCO_3$, die die Gestaltung von Wirkstoffträgern mit verbesserter zellulärer Aufnahme und Viabilitätunterstützen.

## Nomenclature

| | |
|---|---|
| $\alpha_{Phase\,1}$ | Ionic activity product of phase 1 |
| A549 | Adenocarcinomic human alveolar basal epithelial cells |
| ACC | Amorphous calcium carbonate |
| BSA | Bovine serum albumin |
| $CaCO_3$ | Calcium carbonate |
| CDs | Carbon nanodots |
| CNTs | Carbon nanotubes |
| DAPI | 4′,6-Diamidin-2-phenylindol fluorescent dye |
| DDS | Drug delivery systems |
| $d_H$ | Hydrodynamic radius |
| DLVO theory | Theory first defined by Derjaguin, Landau, Vervey, and Overbeek and used to predict the stability of dispersions |
| DMEM | Dulbecco's Modified Eagle Medium |
| $\varepsilon_0$ | Permittivity in vacuum |
| $\varepsilon$ | Dielectric constant |
| EPR | Enhanced permeability and retention effect |
| ENPs | Engineered nanoparticles |
| FCS | Fetal calf serum |
| FL | Fluorescence intensity |
| $F(ka)$ | Henry's function |
| $K_a$ | Equilibrium constant |
| $H$ | Hamaker constant |
| HBSS | Hank's Balanced Salt Solution |
| HOB | Human osteoblast cell line |
| I | Ionic strength of the solution |
| IEP | Isoelectric point |
| $\kappa^{-1}$ | Inverse Debye length |
| $k$ | Boltzmann's constant |
| $ka$ | Debye length |

| | |
|---|---|
| $K_{sp}$ | Solubility product of $CaCO_3$ |
| LSZ | Lysozyme |
| $M_w$ | Molecular weight |
| $N$ | Avogadro's number |
| PAA and PAANa | Poly(acrylic acid) sodium salt |
| PdI | Polydispersity index |
| PEG | Poly(ethylene glycol) |
| PEI | Poly(ethylenimine) |
| $q$ | Modulus of the scattering vector |
| Q.Y. | Fluorescence Quantum Yield |
| RhB | Rhodamine B fluorescent dye |
| RPMI | Roswell Park Memorial Institute medium |
| RT | Room temperature |
| SSA | Specific surface area |
| T | Temperature |
| $U_E$ | Electrophoretic mobility |
| UV | Ultraviolet visible light |
| $V_m$ | Volume of nitrogen |
| W/O or O/W | Water in oil; oil in water emulsion |
| $W_{ld}$ | Double layer force |
| $W_{vdW}$ | Van der Waals attractive force |
| $\rho$ | Density |
| $\eta$ | Viscosity |
| $\sigma_+$ and $\sigma_-$ | The surface charge densities per unit area |
| $\Delta G_{growth}$ | Variation in the free energy due to growth |
| $\Delta G_{nucleation}$ | Variation in the free energy due to nucleation |
| $\Delta G_{Trans\ 1\rightarrow 2}$ | Variation in the Gibbs-free energy during phase-transition |
| $\Delta H_{cryst}$ | Enthalpy of crystallization |
| $\Delta S_{cryst}$ | Entropy of crystallization |
| $\Delta_f$ | Doppler shift |
| $\Gamma$ | Exponential decay rate |

# 1. Introduction and Aims of the Work

## 1.1. General Introduction

The use of engineered nanoparticles (ENPs) in consumer products is becoming increasingly prevalent.[1] As a consequence of the toxicity associated with the high surface area and activity of ENPs,[2] the development of a nanoparticle system that minimizes these harmful effects is highly desirable. One possible approach is the use of biodegradable and biocompatiblecarriers.[3] Lipid-based particles have become the pharmaceutical vehicle of choice with the approval of several liposomal formulations.[4,5] However, due to the limited stability in body and the propensity to leakage, polymeric particles appeared as another viable option.[3,6] Polymers approved by the Food and Drug Administration of the Unities States,[7] like chitosan and poly(lactate), received special attention as they are well tolerated by the body. Yet, in the long term, their degradation products can still cause undesirable side-effects.[7]

Endogenous materials, like calcium phosphate, calcium carbonate and phosphosilicates hold great potential as materials for delivery vehicles.[6] They possess excellent biocompatibility and upon degradation, there is almost no risk of induced toxicity as their ions are already present in the body at high concentrations.[8] In the case of calcium carbonate ($CaCO_3$), its solubility is known to increase under acid environments.[9] This feature has been used to rationalize the use of $CaCO_3$ particle systems in targeting and delivering drugs to solid tumors, as the particles barely release the cargo at neutral physiological pH, while rapidly releasing it at the acidic pH in the tumor microenvironment (pH <6.5).[9-11] The pH-sensitivity combined with its biocompatibility makes $CaCO_3$ of great interest in biomedical research as a nanoengineered platform for the delivery of molecules to biological systems.[9]

Calcium carbonate is already broadly used in industry due to its large availability and low cost of synthesis. It is extensively applied as fillers in paint, plastic, gums and paper,[12-13] as an abrasive in tooth paste,[14] in antacids[10] and as an excipient in effervescent tablets.[14] In biomedical research, besides its aforementioned application as a delivery vehicle based on the pH-sensitive route, this material can be especially interesting to biological systems that either responds to $Ca^{2+}$ ions or to carbonate ions. Accordingly, calcium ions are known to regulate

cell cycle,[15] induce apoptosis,[16] stimulate cell growth and differentiation.[17] Therefore, a boost in the extracellular calcium concentration by $CaCO_3$ carrier dissolution may offer new ways to stimulate bone regeneration[17] or even induce calcium-mediated cytotoxicity.[16] In addition to the release of calcium, the carbonate ions are reported to play a pivotal role in the inhibition of tumor growth by persistent alkalization of solid tumors.[11]

However, some shortcomings to the use of $CaCO_3$ have been identified in terms of its physical properties (size, morphology, water solubility and crystallinity), in the loading and release ability as well as in regard to the instability in water.[18] As shown in Figure 1.1 - item 1, the first limitation is related to the control over the morphology of $CaCO_3$ particles in the sub-micrometer scale. In nature, calcium carbonate occurs in six different morphologies: calcite, vaterite, aragonite, ikaite and monohydrocalcite, as well as hydrated amorphous phases. These crystals are normally large, with a size ranging from 3 to 50 μm, and possess a variety of different crystal morphologies. Despite that, observations of $CaCO_3$ biominerals in mollusk shells[19] and sea urchin spines[20] revealed crystals with unusual shape, and most importantly, smaller particle size (under 3 μm). Inspired by nature, detailed biomineralization studies established the foundation on the control over size, polymorphism and morphology with the help of inorganic ($Mg^{2+}$ ions and polyphosphonate)[19,21] and organic (proteins and macromolecules)[22] additives. These additives can act as antiscalants,[23,24] growth initiators,[25,26] habit modifiers[27,28] or in the stabilization of amorphous phase.[29,30] Based on the principles that regulate the roles of additives in the modification of crystal nucleation and growth, it is possible to design $CaCO_3$-based delivery systems with tailored morphology and size, as reported by a considerable number of publications.[6,12,31-33] However, it is worth mentioning that to date, most synthesis methods do not allow the regulation of the physical properties in the sub-micrometer scale.

The particle size has long been studied as a key parameter to be controlled in delivery systems, as a result of the improved cellular internalization at the nanoscale,[34,35] as well as due to particle escape at the tumor-specific leaky tissues, known as enhanced permeability and retention effect (EPR).[36,37] Recently, the morphology and aspect ratio have come to attention as equally important parameters.[38-40] Anisotropic particles have been shown to benefit from lower phagocytosis clearance, as the internalization by macrophages is dependent on the particle-to-cell orientation.[41] In this context, there is still the need for a synthesis method that would allow for one-pot preparation of anisotropic $CaCO_3$ particles.

Another challenging aspect that needs to be considered is related to the inclusion and release of the cargo molecules (Figure 1.1 - item 2). The

encapsulation of pharmaceutical molecules within particles, offers enough protection from the environment until its release[42] as well as provide the means to for site-specific bioavailability.[43] Common procedures for encapsulation based on $CaCO_3$ particles involve pre-loading methods, like the co-precipitation[44-50] and emulsion-based co-precipitation,[51-53] as well as the post-loading, in which the cargo is physically adsorbed onto porous carriers.[54] As one-pot methods are faster and easier to scale-up, the pre-loading methods are usually preferred. In this context, the complex coacervation is a technique widely used in the food industries for the encapsulation of fish oil[55] and antioxidant oils.[56] Considering that this approach has already been utilized to controlled synthesis of $CaCO_3$ particles in water,[57-58] its use as can potentially allow the encapsulation of charged biomolecules within the precipitated nanoparticles.

The last property evaluated in this thesis is related to the stability of $CaCO_3$ particles in aqueous solutions. Due to the relatively high solubility product in aqueous solution, reports show that $CaCO_3$ particles can be extremely unstable in the presence of water or humidity.[59] In many cases, upon dispersion $CaCO_3$ particles will readily dissolve (Figure 1.1 - item 3i). This dissolution is observed to be phase-dependent, being more pronounced with the less stable phase, like the amorphous phase. Moreover, the presence of calcium chelators, like amino acids and phosphate salts,[60] can potentially accelerate the rate of dissolution. As opposed to dissolution, calcium carbonate particles may also tend to phase-transition to more stable phases (Figure 1, item 3ii), especially at the nanoscale, at which the solubility and reactivity increases due to an enhanced surface to volume ratio.[61] The aforementioned behaviors make these particle systems unstable in water and may hinder their use as delivery system. Given that the thermodynamic driving force for the phase-transformation and dissolution is already well described in terms of the solubility product and the Gibbs free energy,[62] the study on how these properties may affect the cellular interaction is still poorly studied and yet, full of relevance.

Despite being generally regarded as safe, calcium carbonate particles in the size range of 50 nm to 1 μm may cause toxicity when compared to their bulk counterpart.[14] This effect is more pronounced as smaller particles can potentially cross lipid-based cellular membranes[63] and with that, disrupt cellular functions.[64] In general terms, the influences in the cellular response caused by $CaCO_3$ particle systems can be regarded in two different aspects. The first is related to increased extracellular and intracellular calcium concentration due to particle dissolution in medium or within lysosomes.[16,65] Studies revealed contradictories results, as the reported cells show both improved viability[16] or partially died.[14] The second interaction comes from the additives used to control crystallization.[30,58,66] Upon

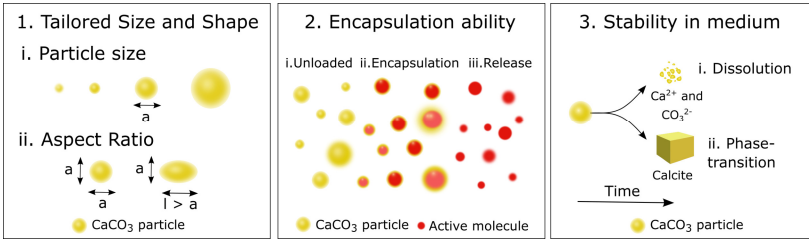


**Figure 1.1:** A summary of the main issues limiting the translation of $CaCO_3$ particles towards the use as delivery vehicles. 1. Shortcomings in controlling the morphology of particles, i.e. size (i) and aspect ratio (ii). 2. The ability to encapsulate and release of the cargo in a controlled manner. 3. The limited particle stability in aqueous solution, in which particles prematurely dissolve releasing their cargo (i), or phase-transform to more stable polymorphs in the micrometer range (ii).

dissolution in medium, organic molecules are released and can possibly cause toxicity by membrane damage.[67] For that, studies that identify the impact of different $CaCO_3$ colloidal systems on the cellular interactions may provide useful for future application.

## 1.2. Aim of the Work

As introduced, $CaCO_3$ particle systems have the potential to be used in health care as delivery vehicles. However, poor control over morphology at the sub-micrometer scale, limited ability to encapsulate and release therapeutic molecules, and particle instability in aqueous solutions could hinder its translation towards viable biomedical systems. In this doctoral thesis, the major focus is on overcoming the aforementioned pitfalls by developing synthesis methods that allow tailored particle size, morphology, and crystallinity; as well as on determining how these properties affect the in vitro biological response.

In order to modulate the particle size and allow the synthesis of protein-loaded $CaCO_3$ carriers, the complex coacervation method is identified as a possible option. For that, the complex coacervation approach is modified to allow the electrostatic coordination of positively and negatively-charged proteins within the coacervate phase, which is then stabilized by the mineralization by subsequent addition of carbonate ions. The following hypotheses will be discussed in more detail in the Chapter 6:

- The charged proteins can comprise one of the assembling components of the complex coacervation due to electrostatic coordination.
- The electrostatic interactions regulate the protein encapsulation efficiency. Accordingly, positively-charged proteins are more likely to be encapsulated at higher efficiencies due to the heterocoagulation with the negatively-charged polyelectrolyte.
- The release of occluded molecules can be triggered by carrier dissolution in acidic environment.

Aiming to control the aspect ratio of $CaCO_3$ particles in a one-pot approach, carbon dots and poly(acrylic acid) are used to mediate the precipitation pathway and allow the formation of both rods and spheres in the sub-micrometer scale. The prepared particles are assessed for the delivery of small fluorescent model molecules to alveolar epithelial cells. Accordingly, the following hypotheses will be discussed in the Chapter 7:

- Carboxylated carbon dots and poly(acrylic acid) can coordinate with calcium ions and potentially reduce $CaCO_3$ supersaturation. As a result of this coordination, these particles serve as templates for the heterogeneous precipitation $CaCO_3$ upon addition of carbonate ions.

- The use of poly(acrylic acid) to stability the particles can induce toxicity and reduce cellular viability.

In chapter 8, calcium carbonate particles with different size, morphology and crystallinity are synthesized and studied based on the changes in the dissolution behavior, colloidal stability and phase-transition in different cell nutrition medium. Moreover, the biological behavior of these particles systems is compared in terms of cytotoxicity and cellular internalization in the in vitro assessments. In this study, the following hypotheses will be highlighted:

- Less thermodynamic stable phases, like amorphous and vaterite phase, may dissolve or phase-transform to calcite phase within the timeframe of the cellular experiments affecting the cellular outcome.
- The phase-transition and dissolution can be more pronounced as the surface-to-volume ratio increases as well as in the presence of calcium chelators.
- Poly(acrylic acid), an additive used to stabilize the amorphous particles, can potentially induce toxicity and reduce cellular viability.

## 1.3. References

1. R. Kessler, *Environ. Health Perspect.*, 2011, **119**, 246–253.

2. H. F. Krug and P. Wick, *Angew. Chemie*, 2011, **123**, 1294–1314.

3. J. Nicolas, S. Mura, D. Brambilla, N. Mackiewicz and P. Couvreur, *Chem. Soc. Rev.*, 2013, **42**, 1147–1235.

4. V. P. Torchilin, *Nat. Rev. Drug Discov.*, 2005, **4**, 145–160.

5. D. Peer, J. M. Karp, S. Hong, O. C. Farokhzad, R. Margalit and R. Langer, *Nat. Nanotechnol.*, 2007, **2**, 751–760.

6. S. Sharma, A. Verma, B. V. Teja, G. Pandey, N. Mittapelly, R. Trivedi and P. R. Mishra, *Colloids Surfaces B Biointerfaces*, 2015, **133**, 120–139.

7. F. Lebre, C. H. Hearnden and E. C. Lavelle, *Adv. Mater.*, 2016, **4,** 5525–5541.

8. T. Shen, Y. Zhang, A. M. Kirillov, B. Hu, C. Shan, W. Liu and Y. Tang, *J. Mater. Chem. B*, 2016, **4**, 7832–7844.

9. S. M. Dizaj, M. Barzegar-Jalali, M. H. Zarrintan, K. Adibkia and F. Lotfipour, *Expert Opin. Drug Deliv.*, 2015, **12**, 1649–1660.

10. R. Raliya, A. Som, N. Shetty, N. Reed, S. Achilefu and P. Biswas, *RSC Adv.*, 2016, **6**, 54331–54335.

11. A. Som, R. Raliya, L. Tian, W. Akers, J. Ippolito, S. Singamaneni, P. Biswas and S. Achilefu, *Nanoscale*, 2016, **8**, 12639–12647.

12. Y. Boyjoo, V. K. Pareek and J. Liu, *J. Mater. Chem. A*, 2014, **2**, 14270–14288.

13. N. K. Dhami, M. S. Reddy and M. S. Mukherjee, *Front. Microbiol.*, 2013, **4**, 1–13.

14. M. Horie, K. Nishio, H. Kato, S. Endoh, K. Fujita, A. Nakamura, S. Kinugasa, Y. Hagihara, Y. Yoshida and H. Iwahashi, *Chem. Biol. Interact.*, 2014, **210**, 64–76.

15. P. Whitfield, James F.; Bird, Ranjana, P.; Chakravarthy, Balu B.; Isaacs, Richards J.; Morley, *J. Cell. Biochem.*, 1995, **22**, 74–91.

16. Y. C. Tseng, A. Yang and L. Huang, *Mol. Pharm.*, 2013, **10**, 4391–4395.

17. E. Tolba, W. E. G. Müller, B. M. Abd El-Hady, M. Neufurth, F. Wurm, S. Wang, H. C. Schröder and X. Wang, *J. Mater. Chem. B*, 2016, **4**, 376–386.

18. Z. Wu, S. Yang and W. Wu, *Nanoscale*, 2016, **8**, 1237–1259.

19. L. B. Gower, *Chem. Rev.*, 2008, **108**, 4551–4627.

20. Y. Politi, T. Arad, E. Klein, S. Weiner and L. Addadi, *Science*, 2009, **306**, 1161–1164.

21. H. Cölfen, *Top Curr Chem*, 2007, **271**, 1–77.

22. S. Kim and C. B. Park, *Adv. Funct. Mater.*, 2013, **23**, 10–25.

23. J. E. Loy, J. Guo and S. J. Severtson, *Ind. Eng. Chem. Res.*, 2004, **43**, 1882–1887.

24. M. M. Reddy and A. R. Hoch, *J. Colloid Interface Sci.*, 2001, **235**, 365–370.

25. A. Tsortos and G. H. Nancollas, *J. Colloid Interface Sci.*, 2002, **250**, 159–167.

26. J. Roqué, J. Molera, M. Vendrell-Saz and N. Salvadó, *J. Cryst. Growth*, 2004, **262**, 543–553.

27. L. Addadi and S. Weiner, *Proc. Natl. Acad. Sci.*, 1985, **82**, 4110–4114.

28. L. Addadi, J. Moradian, E. Shay, N. G. Maroudas and S. Weiner, *Proc. Natl. Acad. Sci. U. S. A.*, 1987, **84**, 2732–6.

29. M. Faatz, F. Gröhn and G. Wegner, *Adv. Mater.*, 2004, **16**, 996–1000.

30. V. Lauth, M. Maas and K. Rezwan, *J. Mater. Chem. B*, 2014, **2**, 7725–7731.

31. G. Begum, T. N. Reddy, K. P. Kumar, K. Dhevendar, S. Singh, M. Amarnath, S. Misra, V. K. Rangari and R. K. Rana, *ACS Appl. Mater. Interfaces*, 2016.

32. S. Guo, M. Yang, M. Chen, J. Zhang, K. Liu, L. Ye and W. Gu, *Dalt. Trans.*, 2015, **44**, 8232–8237.

33. D. B. Trushina, T. V. Bukreeva, M. V. Kovalchuk and M. N. Antipina, *Mater. Sci. Eng. C*, 2015, **45**, 644–658.

34. J. Rejman, V. Oberle, I. S. Zuhorn and D. Hoekstra, *Biochem. J.*, 2004, **377**, 159–69.

35. C. Foged, B. Brodin, S. Frokjaer and A. Sundblad, *Int. J. Pharm.*, 2005, **298**, 315–322.

36. J. W. Nichols and Y. H. Bae, *J. Control. release*, 2014, **190**, 451–64.

37. P. Decuzzi, B. Godin, T. Tanaka, S.-Y. Lee, C. Chiappini, X. Liu and M. Ferrari, *J. Control. Release*, 2010, **141**, 320–327.

38. N. P. Truong, M. R. Whittaker, C. W. Mak and T. P. Davis, *Expert Opin. Drug Deliv.*, 2015, **12**, 129–142.

39. M. B. Fish, A. J. Thompson, C. a. Fromen and O. Eniola-Adefeso, *Ind. Eng. Chem. Res.*, 2015, **54**, 4043–4059.

40. P. Kolhar, A. C. Anselmo, V. Gupta, K. Pant, B. Prabhakarpandian, E. Ruoslahti and S. Mitragotri, *Proc. Natl. Acad. Sci.*, 2013, **110**, 10753–10758.

41. J. a Champion and S. Mitragotri, *Proc. Natl. Acad. Sci.*, 2006, **103**, 4930–4934.

42. R. Challa, A. Ahuja, J. Ali and R. K. Khar, *AAPS PharmSciTech*, 2005, **6**, E329-57.

43. E. Blanco, H. Shen and M. Ferrari, *Nat. Biotechnol.*, 2015, **33**, 941–951.

44. U. Maver, M. Bele and J. Jamnik, *Mater. Res. Bull.*, 2013, **48**, 137–145.

45. Y. Ueno, H. Futagawa, Y. Takagi, a Ueno and Y. Mizushima, *J. Control. Release*, 2005, **103**, 93–8.

46. A. I. Petrov, D. V Volodkin and G. B. Sukhorukov, *Biotechnol. Prog.*, 2005, **21**, 918–25.

47. C.-Q. Wang, J.-L. Wu, R.-X. Zhuo and S.-X. Cheng, *Mol. Biosyst.*, 2014, **10**, 672–8.

48. S. Chen, D. Zhao, F. Li, R.-X. Zhuo and S.-X. Cheng, *RSC Adv.*, 2012, **2**, 1820–1826.

49. T. Borodina, E. Markvicheva, S. Kunizhev, H. Möhwald, G. B. Sukhorukov and O. Kreft, *Macromol. Rapid Commun.*, 2007, **28**, 1894–1899.

50. S. De Koker, B. G. De Geest, S. K. Singh, R. De Rycke, T. Naessens, Y. Van Kooyk, J. Demeester, S. C. De Smedt and J. Grooten, *Angew. Chemie - Int. Ed.*, 2009, **48**, 8485–8489.

51. K. Qian, T. Shi, T. Tang, S. Zhang, X. Liu and Y. Cao, *Microchim. Acta*, 2010, **173**, 51–57.

52. M. Fujiwara, K. Shiokawa, K. Morigaki, Y. Zhu and Y. Nakahara, *Chem. Eng. J.*, 2008, **137**, 14–22.

53. X. He, T. Liu, Y. Chen, D. Cheng, X. Li, Y. Xiao and Y. Feng, *Cancer Gene Ther.*, 2008, **15**, 193–202.

54. N. Qiu, H. Yin, B. Ji, N. Klauke, A. Glidle, Y. Zhang, H. Song, L. Cai, L. Ma, G. Wang, L. Chen and W. Wang, *Mater. Sci. Eng. C*, 2012, **32**, 2634–2640.

55. B. Wang, B. Adhikari and C. J. Barrow, *Food Chem.*, 2014, **158**, 358–365.

56. I. M. Martins, S. N. Rodrigues and F. Barreiro, *J. Microencapsul.*, 2009, **26**, 667–675.

57. S.-C. C. Huang, K. Naka and Y. Chujo, *Langmuir*, 2007, **23**, 12086–12095.

58. P. Kaempfe, V. R. Lauth, T. Halfer, L. Treccani, M. Maas and K. Rezwan, *J. Am. Ceram. Soc.*, 2013, **96**, 736–742.

59. Z. Zou, L. Bertinetti, Y. Politi, A. C. S. Jensen, S. Weiner, L. Addadi, P. Fratzl and W. J. E. M. Habraken, *Chem. Mater.*, 2015, **27**, 4237–4246.

60. N. Tang and L. H. Skibsted, *J. Agric. Food Chem.*, 2016, **64**, 4376–4389.

61. M. Auffan, J. Rose, J.-Y. Bottero, G. V Lowry, J.-P. Jolivet and M. R. Wiesner, *Nat. Nanotechnol.*, 2009, **4**, 634–41.

62. B. V. Parakhonskiy, A. M. Yashchenok, S. Donatan, D. V. Volodkin, F. Tessarolo, R. Antolini, H. Möhwald and A. G. Skirtach, *ChemPhysChem*, 2014, **15**, 2817–2822.

63. W. J. Stark, *Angew. Chemie - Int. Ed.*, 2011, **50**, 1242–1258.

64. S. Moeno, *Chem. Rev.*, 2011, **111**, 3407–3432.

65. B. V. Parakhonsky, M. Zyuzin, A. M. Yashchenok, S. Carregal-romero, J. Rejman, H. Möhwald, W. J. Parak and A. Skirtach, *J Nanobiotechnol*, 2015, **13**, 13–53.

66. R.-Q. Song and H. Cölfen, *Additive controlled crystallization*, 2011.

67. C. Kusonwiriyawong, P. Van De Wetering, J. A. Hubbell, H. P. Merkle and E. Walter, *Eur. J. Pharm. Biopharm.*, 2003, **56**, 237–246.

# 2. Calcium carbonate particles as delivery vehicles

*Overview: In this chapter, a comprehensive overview of the literature involving calcium carbonate as an engineered particle is highlighted. Moreover, a brief description of the main synthesis methods for calcium carbonate nanoparticles is described along with the observations on the phase transformation that can occur in aqueous solutions. This chapter also describes the complex coacervation and the mesoscale self-assembly mechanisms applied to the preparation of synthetic calcium carbonate particles.*

## 2.1. Introduction to calcium carbonate as an engineered material

$CaCO_3$ exists in six different crystal polymorphs, some anhydrous (calcite, aragonite and vaterite) and some hydrated (amorphous, ikaite and monohydrocalcite).[1] Calcite is the most stable phase and can be found in the mollusk shells[2] and sea urchin spines.[3] Aragonite, the second most stable phase, is the main inorganic component of the nacre shell,[4] which is an exquisite hierarchical structure with enhanced mechanical properties used for protection and support. Vaterite is the least stable of the anhydrous polymorphs and can be found for example on the shell of most gastropods. An overview of the main properties of each crystal system is given in table 2.1.

According to table 2.1, the morphology of naturally occurring crystals is fixed. However, with the help of additives, it can be changed from what is reported. In fact, the mineralization of calcium carbonate by microorganism allows the control of crystal size, shape, orientation, phase, texture and location.[2] This occurs via the regulation of the ionic reactants and by the use of additives, which can be either inorganic dopants or organic additives.[5] Common inorganic additives, like Magnesium ions, are present in seawater in seawater at much larger concentrations than calcium ions: 50mM for $Mg^{2+}$ and 12mM $Ca^{2+}$.[2] This ion is known to increase the solubility of calcite and therefore, at higher concentrations, it can favor the formation of the aragonite phase. At lower concentrations, $Mg^{2+}$ can alter the morphology of calcite to a prismatic form.[2]

Morphological control can also be executed with the help of organic additives. Proteins like dentin, collagen and chitin are commonly found occluded in biominerals. The protein concentration can range from the very small quantities in the urchin spines (around 0.02wt%), to an interconnected network in between tablets of nacre sheet, to a collagen matrix in bone (20wt%).[2] The use of organic matrixes allows the nanostructural arrangement of the organic and inorganic

components, which is often organized into hierarchical levels. It is also reported that the mechanical properties of hierarchically-structured materials are enhanced providing better structural support and protection.

The study of biomineralization processes revealed some key organic and inorganic additives that can be used synthetically to mimic the crystallization pathway and with that, allow the morphological and size control. These studies have been reviewed by L. Gower[2], H. Cölfen[6], F. Meldrum[5], and N. Sommerdijk[7] and established the foundation on biomimetic mineralization. The translation of the knowledge acquired on biomineralization to the production of synthetic $CaCO_3$ systems has also been extensively reviewed by H-B. Yao[4] concerning structural properties inspired by nacre, by S. Sharma[8], Y. Boyjoo[9], D. Trushina[10] and D. Volodkin[11] in the micro- and nanometer-sized materials for biological applications and by S. Kim[12] in regard to energy and environmental applications.

Significant effort has been devoted to the use of calcium carbonate in industry. Current industrial applications of calcium carbonate are very simple due to the low mechanical properties. As an example, in paper and paint industries, it is used as fillers and in toothpaste as an abrasive material. However, the use of $CaCO_3$ is slowly shifting towards biological applications, due to its pH-sensitive dissolution, biocompatibility, and degradability. Moreover, novel synthesis techniques allow the encapsulation and release of pharmaceutical ingredients. Given the potential of this material, the following chapters will discuss in detail some key limitations that need to be addressed for the development of tailored $CaCO_3$ particles as carriers to biological systems.

## 2.2. Crystal growth under thermodynamic and kinetic control

In order to explain the typical synthesis routes used to prepare synthetic calcium carbonate particles in the nano- and micrometer range, it is first required the understanding of the role of additives in the nucleation and crystal growth in aqueous solution and how they allow control over the final morphology, crystallinity and particle size.

According to the classical crystallization theory in water in absence of additives,[2,6] in a supersaturated solution containing [$Ca^{2+}$] and [$CO_3^{2-}$] ions, the driving force to precipitation is the degree of supersaturation (S), expressed as $S = \frac{c}{K_{sp}}$, where $c$ is the species concentration and $K_{sp}$ is the solubility product.

**Table 2.1. Overview of different properties of calcium carbonate phases.**

| Properties | Calcite | Aragonite | Vaterite |
|---|---|---|---|
| Crystal system[13] | Trigonal-Rhombohedra | Orthorhombic | Hexagonal |
| Lattice constant | a: 4.991<br>c: 17.062<br>ϒ: 120° | a: 4.959<br>b: 7.964<br>c: 5.738 | a: 4.130<br>c: 8.490<br>ϒ: 120° |
| Natural morphology[5] | Rhombohedra | Needles | Spherical for polycrystalline aggregates |
| Relative enthalpy [14,15,a] | | 0.4 | 3.4 to 3.8 |
| Log $K_{sp}$ [16,17,b] | - 8.4 | - 8.3 | - 7.9 |

n.r. – not reported. [a] Relative enthalpy[18] to calcite (kJ/mol) at 25°C. [b] Logarithmic form of the solubility product constant of $CaCO_3$ particles dispersed in water at 25°C.

In other terms, it can be expressed by the difference in the solute concentration at the supersaturation ($C$) and at equilibrium ($C_s$), $\Delta C = C - C_s$.[19] As the nucleation begins, there is a critical equilibrium radius that determines whether the nuclei are thermodynamically stable or not. If the size is larger than the critical radius, the nuclei grow by ion-by-ion diffusion or layer-by-layer adsorption. While doing so, the overall solute concentration decreases as the solute is being consumed by the nucleation and growth processes. As time elapses, the solute concentration reaches an equilibrium ($C_s$) with the precipitated particles, in which the rates of nucleation and dissolution are equal. This process is schematically presented in the Figure 2.1a.

The precipitation and crystal growth process can also be described in terms of thermodynamic and kinetic control, as illustrated in the figure 2.1b. $\Delta G$ represents the variation in the Gibbs free energy over the course of the precipitation process. At constant temperature ($T$), this can be expressed in terms of the enthalpy of crystallization ($\Delta H_{cryst}$) and entropy of crystallization ($\Delta S_{cryst}$), as $\Delta G = \Delta H_{cryst} - T\Delta S_{cryst}$.[20] Accordingly, two pathways are possible: thermodynamic (A) or kinetic (B).

In the thermodynamic controlled crystal growth, Pathway A, the activation energy for the crystallization can be correlated to the sum of the free energies per unit volume of nucleation ($\Delta G_{nucleation}$) and growth ($\Delta G_{growth}$), as $\Delta G^{A} = \Delta G_{nucleation}{}^{A}$

**Table 2.1** *(continued)*

| Properties | Monohydrocalcite | Ikaite | Amorphous |
|---|---|---|---|
| Crystal system[13] | Trigonal | Monoclinic | n.r. |
| Lattice constant | a: 10.553<br>c: 7.544<br>ϒ: 120° | a: 8.792<br>b: 8.312<br>c: 11.021<br>β: 110.5° | n.r. |
| Natural morphology[5] | n.r. | n.r. | Various |
| Relative enthalpy [14,15,a] | n.r. | n.r. | 24 |
| Log $K_{sp}$ [16,17,b] | -7.6 | -7.4 | -6.3 |

+ $\Delta G_{growth}$ [A]. As reviewed by Meldrum and Cölfen,[5] additives can be used to modify the crystallization by adsorption to the nucleation surface. As a result, the surface energy is lowered, and so is the nucleation rate. This promotes the growth predominantly on the uncoated surfaces.

In contrast to thermodynamic control,[5] Pathway B describes processes in the presence of high concentration of additives, known as kinetically-controlled pathway. This process starts with the formation of precursors phases, which are high soluble and therefore do not require high activation energies, $\Delta G^B$. These precursors are usually highly hydrated, amorphous phases. If the formation of the precursor phase is induced by a polyelectrolyte, it is referred as Polymer-Induced Liquid Precursor (PILP phase). As consequence of the instability of these phases, they are susceptible to phase transformation with low activation energy, $\Delta G_{T1}$, into less hydrated phases but still amorphous in nature: the amorphous calcium carbonate (ACC) phase. Once again, this unstable phase is susceptible to phase-transform to crystalline phases ($\Delta G_{T2}$ and $\Delta G_{T2}$ respectively). Since this is a stepwise process, there is the possibility to manipulate the crystallization in order to favor specific shapes or sizes.[5]

As previously described, the presence of additives changes the mineralization pathway resulting in distinct effects on the crystal nucleation and growth.[7] Common additives have been shown to play different roles in mineralization:[22]

(i) antiscalants hinder mineral growth by disturbing the crystal nucleation.[23,24]

(ii) growth initiators induce local supersaturation and nucleation via ion complexation.[25,26]
(iii) habit modifiers restrain crystal growth by selective adsorption.[27,28]
(iv) stabilization of amorphous, highly hydrated phases (ACC).[29,30]

Accordingly, additives have been shown to play multiple roles at once,[31] which can make the quantitative assessment of their action a challenging task. Gebauer and colleagues[31] showed that simple titration of $Ca^{2+}$ ions provides information on the interaction and influence of different additives in the crystallization process. The results from these experiments allowed the classification of additives in five categories, in which three of them fall within the previously described roles. The other two are the adsorption of ions and the influence on soluble-cluster formation.

Surfactants like cetrimonium bromide (CTAB) and Sodium dodecyl sulfate (SDS)[9,32,33] are shown to have the hydrophilic head groups adsorbed onto specific crystal habits, and the final crystalline phase is attributed to the surfactant orientation and strength of attraction between surfactant and $CaCO_3$ nuclei. Biomolecules such as cellulose,[34,35] silk[36] and starch[37-40] favor the formation of porous vaterite at low additive concentrations as well as increase of the specific surface area.[9] Moreover, amino acids,[41] albumin[11] and lysozyme[42] are shown to be highly incorporated to the crystals (up to 10wt%) and alter their physical properties, for example hardness. Another class of very important additives are polyelectrolytes, like poly(acrylic acid),[30,43] poly(aspartate),[22,44,45] and

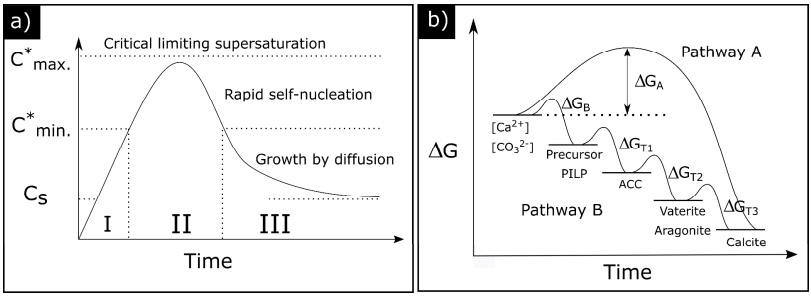


**Figure 2.1:** a) Three stages of classical theory of crystallization.[21] I. prenucleation, II. nucleation, III. growth. $C_{min}$*: minimum concentration for nucleation, $C_{max}$*: maximum concentration for nucleation, $C_s$: solute concentration at equilibrium. b) Pathway A: classical crystallization pathway, Pathway B: kinetically-controlled pathway. Adapted from L. Gower[2] and H. Cölfen.[6]

dendrimers.[46,47] Generally, by increasing the concentration of polyelectrolytes, less stable phases are stabilized, and the crystal morphology seems to be regulated by adsorption-related processes.

In this context, one of the challenging aspects in the biomimetic mineralization is the construction of synthetic materials that resemble their natural counterparts in regard to structure as well as physical properties.[7] For that, the understanding of the interplay between additives and the inorganic phases is essential to prepare useful biomimetic materials with a well-defined morphology.

## 2.3. Phase-transformation and dissolution in aqueous medium

As described in Table 2.1, calcium carbonate exists in different crystalline amorphous phases. Accordingly, all polymorphs have a certain solubility in aqueous solution, which scales with the thermodynamic stability of each crystal phase:[17] more stable phases have a lower the solubility product. In water or humidity, these less stable crystals (or metastable phases) are susceptible to the phase-transition to a more stable polymorph via different mechanisms. The reduction in the Gibbs-free energy is the driving force for such transformation and it can be described by equation 1 as: [48]

$$\Delta G_{Trans\,1\rightarrow 2} = \Delta G_{Phase\,1} - \Delta G_{Phase\,2} = \frac{-RT}{2}\ln\frac{\alpha_{Phase\,2}}{\alpha_{Phase\,1}} \qquad \text{Eq. 1}$$

where $R$ is the gas constant, $T$ is the temperature, $\alpha$ the ionic activity product of each phase, $\Delta G_{Trans\,1\rightarrow 2}$ is the driving force for the phase transition from a less stable phase with Gibbs-free energy $\Delta G_{Phase\,1}$ to a more stable phase with Gibbs-free energy equals to $\Delta G_{Phase\,2}$,. According to the Ostwald Law, at sufficiently high supersaturation, the polymorph that crystallizes first is the most soluble and the least stable.[10,49] This explains why the phase-transformation is a stepwise process, going from less stable polymorphs towards the formation of the stable calcite phase. For more information of the thermodynamic pathway of phase transformation refer the publication by Trushina[10].

In the case of amorphous $CaCO_3$ particles (ACC) in aqueous solution, the transformation of ACC occurs via dissolution-precipitation mechanism.[14,50] Accordingly, the ACC particles dehydrate to less hydrated state, and eventually, crystalline nuclei precipitate via heterogeneous nucleation. This crystalline phase subsequently dissolves and recrystallizes to give space to a more stable phase. Eventually, the calcite phase will be formed. Interestingly, Zou et al.[51] describes that, in aqueous solution, the favoring of the crystalline phase is dependent on the

ACC particle size. Smaller particles (66 nm) favor the transformation to vaterite phase, while larger particles (196 nm) phase-transforms directly to calcite. Konrad et al.[52] reports that the transformation of ACC into crystalline is only triggered after the physisorption of a critical amount of water, thus providing evidence that the solid-state transformation might not play as an important role in the phase-transformation of the amorphous phase.

The phase transformation of less stable crystalline phases to calcite is shown to occur via heterogeneous nucleation and interface-controlled growth. According to Peric and colleagues[1], the transformation from aragonite to calcite crystals occurs preferentially at surface defects (like cleavages or fractures), in which calcite nuclei are formed with an expansion of about 8% in volume. The enthalpy of phase transformation of aragonite-calcite is reported at about -0.3 kJ/mol, indicating that the transformation is an energetically-favored, endothermic process.[14,15] In contrast, the vaterite-calcite transformation occurs with a decrease in volume of about 2% and the enthalpy of phase transformation is around -3.5 kJ/mol.

The phase-transformation rate is known to be depend on the intrinsic nature of the particles (composition and crystal phase)[14] and can largely be accelerated by the presence of water/humidity.[1,15] Besides the intrinsic properties, the environmental conditions, like presence of proteins, amino acids, calcium-chelating moieties and high ionic strength are also known to enhance the transformation rate.[53-55] The role of ionic strength is described by Parakhonskiy and colleagues[56], as the recrystallization to calcite does not occur in ethanol and is accelerated with increased ionic strength. In Millipore water, the phase-transition starts at around 48 hours of incubation, while for phosphate saline buffer (PBS) at around 5 hours.

Another important consideration is the dissolution behavior of these particles in water. This can be specially a problem, if the released ions can induce toxicity in cellular studies.[57] In the case of weak salts, like $CaCO_3$, the solubility is highly dependent on the pH. This is governed by the equilibrium equation 2, which already considers the hydrolysis of the carbonate ion:[13]

$$S^2 = K_{sp}\left(1 + \frac{[\mathrm{H}^+]}{K_{a2}} + \frac{[\mathrm{H}^+]^2}{K_{a1}\,K_{a2}}\right) \qquad \text{Eq. 2}$$

where $K_{sp}$ is the solubility product of $CaCO_3$ phase that vary from $3.7\times10^{-9}$ to $8.7\times10^{-9}$ $M^2$ at 25 °C for different phases, $K_{a1}$ and $K_{a2}$ are the equilibrium constants set as $2.5\times10^{-4}$ $M^2$ and $5.61\times10^{-11}$ $M^2$ at 25 °C respectively (equilibrium equations are described on section 10.1). Accordingly, the solubility is highly

dependent on the pH, as plotted in the Figure 2.2. This instability at acidic pHs can actively be used to trigger the dissolution of $CaCO_3$ particles in solid tumors.[13] In cancer therapy, it is well documented that the tumor pH is more acidic than that in the blood due to increased production of and slow exportation of lactate and $CO_2$.[58]

It is also important to mention that the instability in aqueous solution is more pronounced at the nanoscale since both the solubility and reactivity are enhanced with increasing surface free energy.[56,57,59] Diedrich and colleagues[60] described the relationship in terms of particle size, surface area, and dissolution rate for nanoscale materials. Accordingly, for spherical particles this effect can be described using the modified Kelvin equation, as:

$$\frac{s}{s_0} = \exp\left[\frac{4\,\gamma\,\bar{V}}{RT\,d}\right] \qquad \text{Eq. 3}$$

where $s_0$ and s designate the solubility of a particle of infinite diameter and of diameter $d$, respectively, $\gamma$ refers to the surface free energy, and $\bar{V}$ stands for the solid phase molecular volume. Accordingly, the solubility of the particles increases at the nanoscale. This is experimentally demonstrated[60] using amorphous $SiO_2$ particles, in which by reducing the average particle size from 177 nm to 25 nm, the normalized dissolution rates are 0.3 log units faster.[60]

## 2.4. Synthesis route for $CaCO_3$ engineered particles

Based on the biomineralization principles, different synthesis methods have been developed. The most common routes are based on the use organic additives. These techniques can be sorted into four main approaches[9] as described in Figure 2.3. Each one of the routes will result in different morphologies, size and crystal phase.

Spontaneous precipitation reactions rely on the use of additives at high concentration to control the properties of the final crystal. In this technique, by mixing the two supersaturated solutions, one rich in calcium ions and the other in carbonate ions, particles precipitate within a few hours and are collected via centrifugation or freeze-drying. Experimental parameters, such as pH, temperature, $[Ca^{2+}]$:$[CO_3^{2-}]$ ratio, additive concentration and additive type, can be varied to obtain the desired polymorph, morphology and size of particles. [9]

One important modification of the spontaneous precipitation involves the combination with solvents, like polyols[56,61-65] and polyglcerol.[66] A review by D. Trushina[10] and colleagues shows that the use of alcohols can facilitate the

formation of vaterite crystals due to the strong electric interaction of OH-groups with the vaterite surface, which reduces the surface energy of this phase and makes it thermodynamically more stable than aragonite or calcite. Moreover, the high local viscosity of compounds like glycerol can significantly limit the rate of diffusion and effectively slow down the particle growth.

In the slow carbonation reactions, $CO_3^{2-}$ ions are introduced via the slow hydrolysis of dimethyl carbonate (DMC) or ammonium carbonate ($(NH_4)_2CO_3$) under alkaline conditions. As the addition of carbonate is dependent on both hydrolysis reaction and diffusion, typically long reaction times are involved.[9] Both the aforementioned techniques are usually considered bio-inspired, as the additives of choice mimic the biomineralization processes. As reviewed by Y. Boyjoo and colleagues,[9] these techniques result in a mixture of different polymorph (ACC, calcite, vaterite and aragonite) and the size ranges from nano to micrometer size.

$CaCO_3$ particles are also produced by microemulsions. The use of reverse water in oil (W/O) emulsions allows for the synthesis of particles with narrow particle size distribution in the nano-range,[9] owing to the physical constraints created by the micelles during the mineralization. As the crystallization occurs within water micelles stabilized by surfactant or polymer in the oil phase, the oil/water interface act like a cage which controls the nucleation and growth, resulting in nanosized, monodispersed particles.[8] Similarly to the precipitation and carbonation reactions, the morphology and crystal phase of the final $CaCO_3$ particles can be controlled by the $[Ca^{2+}]$:$[CO_3^{2-}]$ ratio, pH, temperature, additional additives as well as by the surfactant-to-water ratio.[9]

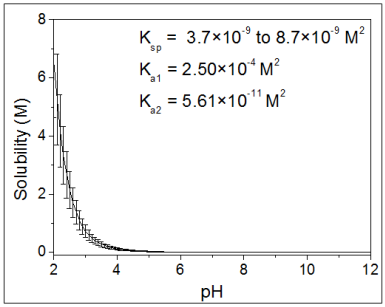


**Figure 2.2:** The pH-dependent solubility of calcium carbonate at varying pHs. $K_{a1}$ and $K_{a2}$ are the equilibrium constants of $H_2CO_3$ and $HCO_3^-$. $K_{SP}$ is the solubility product of $CaCO_3$. Equilibrium equations can be found on Appendix 10.1.

The $CO_2$-bubbling technique allows the production of $CaCO_3$ particles by flushing carbon dioxide through a slaked lime solution, $Ca(OH)_2$.[9] Due to the basic nature of the slaked lime solution, the synthesis occurs at high pH, yielding most commonly the calcite phase with rhombohedral morphology. According to [9], the final particles are highly aggregated, specially due to the nanometer-sized obtained. Typical parameters used to control the process are: temperature, stirring speed, supersaturation, gas volumetric flow rate and reaction time.

In summary, most of the fabrication methods are one-pot processes that enable the synthesis of both nano- and micrometer sized $CaCO_3$ particles with various morphologies and polymorphs. These synthetic particles have been tested in a wide range of applications, from fillers to more complex delivery systems. In the next section, it will be highlighted a few techniques used for the encapsulation of molecules within the $CaCO_3$ particles systems.

### 2.4.1. Encapsulation methods for $CaCO_3$ particles

It has long been suggested that $CaCO_3$ can be potentially used as a drug carrier due to its biocompatibility and biodegradability, low cell cytotoxicity and cost-effectiveness.[67] For that, it is required that a cargo should be encapsulated within the particles and released in a controlled fashion to the environment. According to

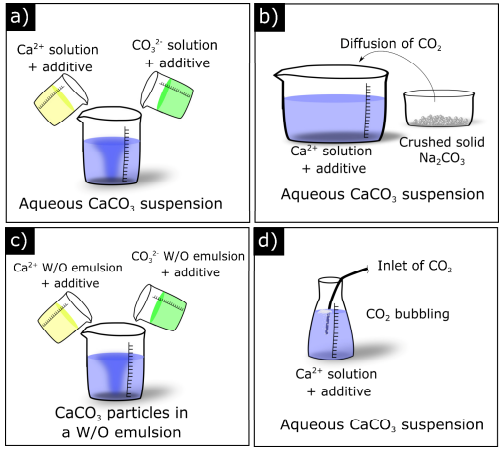


**Figure 2.3:** Commonly described synthesis routes for the preparation of $CaCO_3$ particles from solution: a) spontaneous precipitation, b) slow diffusion, c) emulsion, d) $CO_2$ bubbling. Adapted from [9].

Sharma[8], the low encapsulated amount of e.g. therapeutic molecules that can be achieved by calcium carbonate and phosphate is one of the major limitations that need to be addressed. As reviewed by Volodkin[11], two methods have been developed to encapsulate the cargo using $CaCO_3$ carriers: pre-loading techniques (co-precipitation and microemulsion methods) and post-loading techniques (adsorption and immobilization).

The most common method for the encapsulation of molecules is the co-precipitation method.[68-73] As previously reviewed,[8] this technique involves the spontaneous precipitation of the $CaCO_3$ phase from an aqueous solution already containing the cargo to be encapsulated. As an example, Chen and colleagues[69] used this technique produced 100 nm-particles loaded with DNA and doxorubicin (DOX), at a loading content of 1.3wt% and an encapsulation efficiency of more than 90%. Utilizing the same technique, Koker et al.[73] reports the synthesis of 3 μm-particles loaded with ovalbumin.

Similarly, the emulsification process is another very common technique at the laboratory scale for the preparation nanoparticles due to the wide range of morphologies and good encapsulation efficiencies.[42,74-76] Fujiwara and colleagues[75] described the synthesis of mesoporous capsules with a diameter of around 5 μm. These particles were tested for the encapsulation of bovine serum albumin, ovalbumin, papain, lysozyme and DNA. The encapsulation efficiencies largely varied depending on protein size and charge, but BSA was encapsulated with the highest efficiency, 92%, while LSZ the worst one, with an efficiency of about 0.01%.

Post-loading methods rely on the high porosity of the samples for good encapsulation efficiencies.[39,77-81] According to Sharma,[8] the encapsulation efficiency of post loading techniques are, in many cases, still low compared to the use of soft nanoparticles, like liposomes and hydrogels. For optimized cargo adsorption, the parameters like particle size, crystalline, specific surface area and morphology need to be tailored. As previously reviewed,[10] vaterite particles specially benefit from high porosity and nanostructured surface, which allows them to adsorb large proteins with high efficiency. Accordingly, proteins like catalase, insulin, aprotinin, and protamine adsorb at different efficiencies at the vaterite surface due to varied thermodynamic protein affinity.[81] This can be experimentally determined by calculating the Gibbs free energy derived from the adsorption isotherms. Moreover, positively-charged catalase and insulin bind strongly to the vaterite microspheres due to the electrostatic attractive forces. The opposite occurs for aprotinin and protamine.

The chemical immobilization strategy has been reported for the loading calcium carbonate nanoparticles.[82] In this technique, α-amylase was covalently-immobilized on glutaraldehyde-activated, silanized $CaCO_3$ particles at around 200 mg/g of nanoparticles. It must be noted that due to the silanization reaction, the silica coating alters the surface chemistry of the particles, which can modify the cellular interactions and the biodegradability. Recently developed, the solvent-exchange method is another technique that allows the loading of $CaCO_3$ cores with an amount exceeding that for the physiosorption.[11] For that, a solution containing the $CaCO_3$ particles and the protein to be encapsulated is set to a pH equal to the isoelectric point of the protein (IEP). As a result, large quantities of protein spontaneously precipitate in the pores of the particles, as this is a surface-mediated process.

## 2.5. Complex coacervation

The description of coacervation was introduced by Bungenberg de Jong in 1929.[83] Two main types of coacervation have been described and differ by the phase separation mechanism. *Simple* coacervation is achieved when a homogeneous solution of charged macromolecules undergoes liquid-liquid phase separation, giving rise to a polymer-rich, dense phase and polymer-depleted supernatant,[84] in which both liquid phases are incompatible, immiscible and are in equilibrium. The mechanism involves the partial desolvation or dehydration of macromolecules, by e.g. addition of salts or alcohol.[85,86] *Complex* coacervation is induced by electrostatic interaction and comprises two or more oppositely charged colloids.

Both techniques are widely used in the food industries to encapsulate fish oil[87] and in cosmetics, to encapsulate antioxidant oils.[88] Recent research reported the

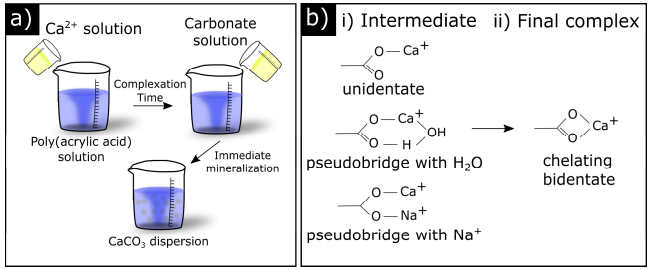


**Figure 2.4:** a) Illustration of the coacervate-directed method. b) Intermediate and final stage of electrostatic coordination between PAA and $Ca^{2+}$ ions. Adapted from [94].

encapsulation and delivery of growth factors,[89] genes,[90,91] as well as proteins.[92] Furthermore, coacervates are currently being investigated for their role in protocell formation and as models of protocell assembly.[93]

As mentioned before, polyelectrolytes are also useful additives to modulate the mineralization of $CaCO_3$. It was first hypothesized by Huang and colleagues[94] that polyelectrolytes could primarily form complex coacervate droplets upon complexation with calcium ions, and later be mineralized by addition of carbonate ions. This approach, known as controlled-addition method, is described in Figure 2.4a. Firstly, poly(acrylic acid) (PAA) in dispersed in aqueous solution, to which a solution containing $Ca^{2+}$ ions is added. Accordingly, PAA can coordinate with positively-charged $Ca^{2+}$ ions. The structure of the coordination is proposed in three different intermediate types, as depicted in Figure 2.4b. This coordination, or ion pairing is endothermic and is entropically driven.[95] As a result of the complexation, it is suggested that PAA molecules become more hydrophobic and phase-separate, forming polymer-rich, liquid-like particles known as complex coacervate droplets.[94] Due to hydrated nature, these droplets grow by the Ostwald-Ripening process, a time-dependent process in which bigger particles grow in expense of smaller ones by successive aggregation and coalescence. This means that the particle size of the droplets could be controlled by complexation time. By adding sodium carbonate to the droplets-containing solution, the fluidic particles are mineralized into stable and colloidally stable calcium carbonate particles. This process was further developed to be produce micromolded amorphous parts,[96] and then modified for the encapsulation of proteins.[30]

With the controlled-addition method,[94] monodispersed $CaCO_3$ particles with controlled size are obtained. Further reports on the basis of complex coacervation and mineralization focused on the preparation of micromolded ceramic components[96] and even PAA/$Ca^{2+}$ hydrogels that can be reversibly molded into transparent films.[43] In this thesis, complex coacervation is studied as both a method to encapsulate proteins within $CaCO_3$ particles as well as to modulate the particle size, as will be described in chapter 6.

## 2.6. Mesoscale self-assembly and colloidal crystals

As previously described, additives not only affect the nucleation but also the growth of $CaCO_3$ particles. Many studies report the formation of 3D arrays of isooriented single crystal particles, refereed as mesocrystals.[97] This term was first coined by Cölfen[98] and has a certain similarity with the concept of colloidal crystals. The difference is that mesocrystals have a well-defined structure at the atomic level, while colloidal crystals do not.[99] The term mesocrystal is generally

used in the biomineralization community referring to crystals formed by mesoscale transformation,[97] while colloidal crystal is often used by the colloidal assembly community referring to crystals created by oriented assembly.[100]

According to the classical growth mechanism, which can also occur in the presence of additives, the growth of the nucleated primary nanoparticles occurs by the ion-by-ion addition mechanism, which results in the formation of rough, irregularly-shaped single crystals loaded with the polymer additive (Figure 2.5, b).[101] In the case of mesocrystal formation, growth occurs under a multistep kinetically driven reaction. In this pathway, the crystallization follows a stepwise process that starts with the nucleation of primary nanoparticles. Their growth occurs by the assembly of particles or complexes to the primary nanoparticles, referred to as mesoscale transformation, which can occur rapidly and unoriented, or, in some specific cases, it can be oriented by the adsorption of macromolecules onto specific crystallographic growth planes of primary nanoparticles (Figure 2.5, a).[97,102] This ordered structure is a result of nanoparticle-macromolecule interactions, which allows the assembly to take place in a mutually oriented fashion forming higher-order superstructures.[97] The primary nanoparticles that form the superstructure can either fuse to form one single crystal or remain at the nanoscale, depending on the binding affinity between nanoparticles and macromolecules.[98] If oriented assembly takes place with crystallites that do not

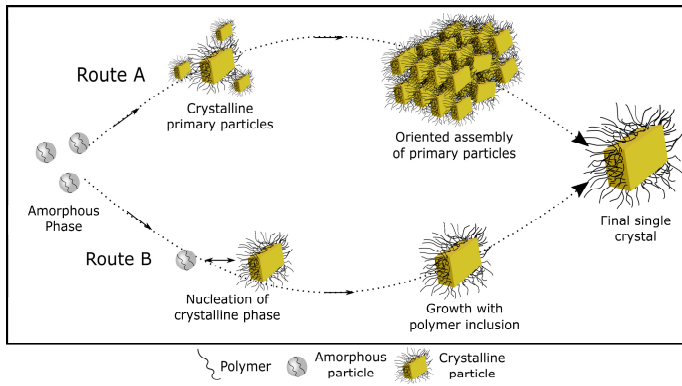


**Figure 2.5:** Schematic growth of calcite in the presence of polymeric additives. a) Oriented-self assembly of primary building blocks, which then fuse to create a single crystal loaded with polymer additive. b) Classical crystallization via ion-by-ion addition to the single crystal surface, in which, due to the occlusion of additives, the morphology is irregular and the roughness is more pronounced.[104]

fuse together, the resulting superstructures are often referred to as mesocrystals.[66] On the other hand, if the primary particles fuse, they can form a single crystal.[66,97,103]

Both processes of mesoscale assembly[105] and directed colloidal assembly[100] can be used for the preparation of novel particle systems. One interesting example is the nacre, which is formed from mutually perfectly crystallographically aligned aragonite tablets.[6] This hierarchical structure provides improved mechanical properties and has served as inspiration for the fabrication ultra-strong artificial nanocomposites.[6] Another example is the strategy that uses non-spherical building blocks to produce anisotropic colloidal crystals described on Chapter 7.[106]

## 2.7. References

1. J. Peric, M. Vucak, R. Krstulovic, L. Brecevic and D. Kralj, *Thermochim. Acta*, 1996, **277**, 175–186.

2. L. B. Gower, *Chem. Rev.*, 2008, **108**, 4551–4627.

3. Y. Politi, T. Arad, E. Klein, S. Weiner and L. Addadi, *Science*, 2009, **306**, 1161–1164.

4. H.-B. Yao, J. Ge, L.-B. Mao, Y.-X. Yan and S.-H. Yu, *Adv. Mater.*, 2014, **26**, 163–188.

5. F. C. Meldrum and H. Cölfen, *Chem. Rev.*, 2008, **108**, 4332–4432.

6. H. Cölfen, *Top Curr Chem*, 2007, **271**, 1–77.

7. N. a J. M. Sommerdijk and G. De With, *Chem. Rev.*, 2008, **108**, 4499–4550.

8. S. Sharma, A. Verma, B. V. Teja, G. Pandey, N. Mittapelly, R. Trivedi and P. R. Mishra, *Colloids Surfaces B Biointerfaces*, 2015, **133**, 120–139.

9. Y. Boyjoo, V. K. Pareek and J. Liu, *J. Mater. Chem. A*, 2014, **2**, 14270–14288.

10. D. B. Trushina, T. V. Bukreeva, M. V. Kovalchuk and M. N. Antipina, *Mater. Sci. Eng. C*, 2015, **45**, 644–658.

11. D. Volodkin, *Adv. Colloid Interface Sci.*, 2014, **207**, 306–24.

12. S. Kim and C. B. Park, *Adv. Funct. Mater.*, 2013, **23**, 10–25.

13. S. M. Dizaj, M. Barzegar-Jalali, M. H. Zarrintan, K. Adibkia and F. Lotfipour, *Expert Opin. Drug Deliv.*, 2015, **12**, 1649–1660.

14. V Radha, T. Z. Forbes, C. E. Killian, P. U. P. a Gilbert and A. Navrotsky, *Proc. Natl. Acad. Sci. U. S. A.*, 2010, **107**, 16438–16443.

15. T. Ogino, T. Suzuki and K. Sawada, *Geochim. Cosmochim. Acta*, 1987, **51**, 2757–2767.

16. L. Brecevic and D. Kralj, *Croat. Chem. Acta*, 2007, **80**, 467–484.

17. L. N. Plummer and E. Busenberg, *Geochim. Cosmochim. Acta*, 1982, **46**, 1011–1040.

18. D. Zhao, Y. Zhu, F. Li, Q. Ruan, S. Zhang, L. Zhang and F. Xu, *Mater. Res. Bull.*, 2010, **45**, 80–87.

19. B. L. Cushing, V. L. Kolesnichenko and C. J. O. Connor, 2004, **104**, 3893–3946.

20. P. G. Vekilov, *AIP Conf. Proc.*, 2010, **1270**, 60–77.

21. T. Sugimoto, *Adv. Colloid Interface Sci.*, 1987, **28**, 65–108.

22. B. J. McKenna, J. H. Waite and G. D. Stucky, *Cryst. Growth Des.*, 2009, **9**, 4335–4343.

23. J. E. Loy, J. Guo and S. J. Severtson, *Ind. Eng. Chem. Res.*, 2004, **43**, 1882–1887.

24. M. M. Reddy and A. R. Hoch, *J. Colloid Interface Sci.*, 2001, **235**, 365–370.

25. A. Tsortos and G. H. Nancollas, *J. Colloid Interface Sci.*, 2002, **250**, 159–167.

26. J. Roqué, J. Molera, M. Vendrell-Saz and N. Salvadó, *J. Cryst. Growth*, 2004, **262**, 543–553.

27. L. Addadi and S. Weiner, *Proc. Natl. Acad. Sci.*, 1985, **82**, 4110–4114.

28. L. Addadi, J. Moradian, E. Shay, N. G. Maroudas and S. Weiner, *Proc. Natl. Acad. Sci. U. S. A.*, 1987, **84**, 2732–6.

29. M. Faatz, F. Gröhn and G. Wegner, *Adv. Mater.*, 2004, **16**, 996–1000.

30. V. Lauth, M. Maas and K. Rezwan, *J. Mater. Chem. B*, 2014, **2**, 7725–7731.

31. D. Gebauer, H. Cölfen, A. Verch and M. Antonietti, *Adv. Mater.*, 2009, **21**, 435–439.

32. Z. Chen and Z. Nan, *J. Colloid Interface Sci.*, 2011, **358**, 416–422.

33. Y. Zhao, S. Li, L. Yu, Y. Liu, X. Wang and J. Jiao, *J. Cryst. Growth*, 2011, **324**, 278–283.

34. F. Zhang, X. Yang and F. Tian, *Mater. Sci. Eng. C*, 2009, **29**, 2530–2538.

35. S. Kirboga and M. Öner, *Powder Technol.*, 2013, **249**, 95–104.

36. L. Liu, X. Zhang, X. Liu, J. Liu, G. Lu, D. L. Kaplan, H. Zhu and Q. Lu, *ACS Appl. Mater. Interfaces*, 2015, **7**, 1735–1745.

37. C. Wang et al., *Sci. Rep.*, 2016, **6**, 24490.

38. Y. Zhao, Y. Lu, Y. Hu, J.-P. Li, L. Dong, L.-N. Lin and S.-H. Yu, *Small*, 2010, **6**, 2436–42.

39. W. Wei, G.-H. Ma, G. Hu, D. Yu, T. McLeish, Z.-G. Su and Z.-Y. Shen, *J. Am. Chem. Soc.*, 2008, **130**, 15808–15810.

40. X. Ying, C. Shan, K. Jiang, Z. Chen and Y. Du, *RSC Adv.*, 2014, **4**, 10841–10844.

41. Y.-Y. Kim, J. D. Carloni, B. Demarchi, D. Sparks, D. G. Reid, M. E. Kunitake, C. C. Tang, M. J. Duer, C. L. Freeman, B. Pokroy, K. Penkman, J. H. Harding, L. A. Estroff, S. P. Baker and F. C. Meldrum, *Nat. Mater.*, 2016, in press, DOI: 10.1038/nmat4631.

42. X. Wang, H. Sun, Y. Xia, C. Chen, H. Xu, H. Shan and J. R. Lu, *J. Colloid Interface Sci.*, 2009, **332**, 96–103.

43. S. Sun, L.-B. Mao, Z. Lei, S.-H. Yu and H. Cölfen, *Angew. Chemie Int. Ed.*, 2016, 1–6.

44. H. Cölfen and M. Antonietti, *Langmuir*, 1998, **14**, 582–589.

45. L. . Gower and D. . Tirrell, *J. Cryst. Growth*, 1998, **191**, 153–160.

46. J. Donners, B. R. Heywood, E. W. Meijer, R. J. M. Nolte and N. A. J. . Sommerdijk, *Chem. - A Eur. J.*, 2002, **8**, 2561–2567.

47. J. M. Donners, E. W. Meijer, R. J. M. Nolte, C. Roman, A. P. H. J. Schenning, N. A. J. M. Sommerdijk and B. R. Heywood, *Chem. Commun.*, 2000, 1937–1938.

48. B. V. Parakhonskiy, A. M. Yashchenok, S. Donatan, D. V. Volodkin, F. Tessarolo, R. Antolini, H. Möhwald and A. G. Skirtach, *ChemPhysChem*, 2014, **15**, 2817–2822.

49. S. Khoshkhoo and J. Anwar, *J. Phys. D. Appl. Phys.*, 1993, **26**, B90–B93.

50. C. Rodriguez-Navarro, K. Elert and R. Ševčík, *CrystEngComm*, 2016, **18**, 6594–6607.

51. Z. Zou, L. Bertinetti, Y. Politi, A. C. S. Jensen, S. Weiner, L. Addadi, P. Fratzl and W. J. E. M. Habraken, *Chem. Mater.*, 2015, **27**, 4237–4246.

52. F. Konrad, F. Gallien, D. E. Gerard and M. Dietzel, *Cryst. Growth Des.*, 2016, **16**, 6310–6317.

53. M. P. Monopoli, C. Åberg, A. Salvati and K. A. Dawson, *Nat. Nanotechnol.*, 2012, **7**, 779–786.

54. K. Sawada, *Pure Appl. Chem.*, 1997, **69**, 921–928.

55. F. Meder, S. S. Thomas, L. W. Fitzpatrick, A. Alahmari, S. Wang, J. G. Beirne, G. Vaz, G. Redmond and K. A. Dawson, *ACS Nano*, 2016, **10**, 4660–4671.

56. B. V. Parakhonskiy, A. Haase and R. Antolini, *Angew. Chemie Int. Ed.*, 2012, **51**, 1195–1197.

57. M. Horie, H. Kato, K. Fujita, S. Endoh and H. Iwahashi, *Chem. Res. Toxicol.*, 2012, **25**, 605–619.

58. J. Yu, X. Chu and Y. Hou, *Chem. Commun. (Camb).*, 2014, **50**, 11614–30.

59. M. Auffan, J. Rose, J.-Y. Bottero, G. V Lowry, J.-P. Jolivet and M. R. Wiesner, *Nat. Nanotechnol.*, 2009, **4**, 634–41.

60. T. Diedrich, A. Dybowska, J. Schott, E. Valsami-jones and E. H. Oelkers, *Environ. Sci. Technol.*, 2012, **4909**.

61. D. B. Trushina, S. N. Sulyanov, T. V. Bukreeva and M. V. Kovalchuk, *Crystallogr. Reports*, 2015, **60**, 570–577.

62. D. Zhao, J. Jiang, J. Xu, L. Yang, T. Song and P. Zhang, *Mater. Lett.*, 2013, **104**, 28–30.

63. X. Zhao, S. Ng, B. C. Heng, J. Guo, L. Ma, T. T. Y. Tan, K. W. Ng and S. C. J. Loo, *Arch. Toxicol.*, 2013, **87**, 1037–1052.

64. D. B. Trushina, T. V. Bukreeva and M. N. Antipina, *Cryst. Growth Des.*, 2016, **16**, 1311–1319.

65. M. Cocquyt, B. Pinchasik, D. Khalenkow, H. Mo, M. Konrad and A. Skirtach, *ACS Appl. Mater. Interfaces*, 2016, **8**, 14284–14292.

66. R.-Q. Song and H. Cölfen, *Adv. Mater.*, 2010, **22**, 1301–1330.

67. R. Kurapati and A. M. Raichur, *J. Mater. Chem. B*, 2013, **1**, 3175.

68. C.-Q. Wang, J.-L. Wu, R.-X. Zhuo and S.-X. Cheng, *Mol. Biosyst.*, 2014, **10**, 672–8.

69. S. Chen, D. Zhao, F. Li, R.-X. Zhuo and S.-X. Cheng, *RSC Adv.*, 2012, **2**, 1820–1826.

70. Y. Ueno, H. Futagawa, Y. Takagi, a Ueno and Y. Mizushima, *J. Control. Release*, 2005, **103**, 93–8.

71. M. L. De Temmerman, J. Demeester, F. De Vos and S. C. De Smedt, *Biomacromolecules*, 2011, **12**, 1283–1289.

72. U. Maver, M. Bele and J. Jamnik, *Mater. Res. Bull.*, 2013, **48**, 137–145.

73. S. De Koker, B. G. De Geest, S. K. Singh, R. De Rycke, T. Naessens, Y. Van Kooyk, J. Demeester, S. C. De Smedt and J. Grooten, *Angew. Chemie - Int. Ed.*, 2009, **48**, 8485–8489.

74. K. Qian, T. Shi, T. Tang, S. Zhang, X. Liu and Y. Cao, *Microchim. Acta*, 2010, **173**, 51–57.

75. M. Fujiwara, K. Shiokawa, K. Morigaki, Y. Zhu and Y. Nakahara, *Chem. Eng. J.*, 2008, **137**, 14–22.

76. X. He, T. Liu, Y. Chen, D. Cheng, X. Li, Y. Xiao and Y. Feng, *Cancer Gene Ther.*, 2008, **15**, 193–202.

77. A. I. Petrov, D. V Volodkin and G. B. Sukhorukov, *Biotechnol. Prog.*, 2005, **21**, 918–25.

78. G. B. Sukhorukov, D. V. Volodkin, A. M. Gunther, A. I. Petrov, D. B. Shenoy and H. Mohwald, *J. Mater. Chem.*, 2004, **14**, 2073.

79. D. V Volodkin, N. I. Larionova and G. B. Sukhorukov, *Biomacromolecules*, 2004, **5**, 1962–1972.

80. C. Wang, C. He, Z. Tong, X. Liu, B. Ren and F. Zeng, *Int. J. Pharm.*, 2006, **308**, 160–167.

81. N. G. Balabushevich, a. V. Lopez de Guerenu, N. a. Feoktistova and D. Volodkin, *Phys. Chem. Chem. Phys.*, 2015, **17**, 2523–2530.

82. Y.-H. Won, H. S. Jang, D.-W. Chung and L. a. Stanciu, *J. Mater. Chem.*, 2010, **20**, 7728.

83. B. de Jong and H. R. Kruypz, *Proc. K. Ned. Akad. Wet.*, 1929, **32**, 849–856.

84. V. K. Aswal and J. Kohlbrecher, 2005, **21**, 149–160.

85. R. Arshady, *Polym. Eng. Sci.*, 1990, **30**, 905–914.

86. J. Nicolas, S. Mura, D. Brambilla, N. Mackiewicz and P. Couvreur, *Chem. Soc. Rev.*, 2013, **42**, 1147–1235.

87. B. Wang, B. Adhikari and C. J. Barrow, *Food Chem.*, 2014, **158**, 358–365.

88. I. M. Martins, S. N. Rodrigues and F. Barreiro, *J. Microencapsul.*, 2009, **26**, 667–675.

89. H. K. Awada, N. R. Johnson and Y. Wang, *Macromol. Biosci.*, 2014, **14**, 679–686.

90. K. . Leong, H.-Q. Mao, V. . Truong-Le, K. Roy, S. . Walsh and J. . August, *J. Control. Release*, 1998, **53**, 183–193.

91. Y. Yuan, J. Tan, Y. Wang, C. Qian and M. Zhang, *Acta Biochim Biophys Sin*, 2009, **41**, 515–526.

92. N. Ray, T. Ambe and Y. Wang, *Acta Biomater.*, 2014, **10**, 40–46.

93. S. Mann, *Acc. Chem. Res.*, 2012, **45**, 2131–2141.

94. S.-C. C. Huang, K. Naka and Y. Chujo, *Langmuir*, 2007, **23**, 12086–12095.

95. D. Priftis, N. Laugel and M. Tirrell, *Langmuir*, 2012, **28**, 15947–57.

96. P. Kaempfe, V. R. Lauth, T. Halfer, L. Treccani, M. Maas and K. Rezwan, *J. Am. Ceram. Soc.*, 2013, **96**, 736–742.

97. H. Cölfen and S. Mann, *Angew. Chemie - Int. Ed.*, 2003, **42**, 2350–2365.

98. H. Cölfen and M. Antonietti, *Angew. Chemie Int. Ed.*, 2005, **44**, 5576–5591.

99. L. Bergström, E. V. Sturm (née Rosseeva), G. Salazar-Alvarez and H. Cölfen, *Acc. Chem. Res.*, 2015, 1505-1514.

100. M. Grzelczak, J. Vermant, E. M. Furst and L. M. Liz-Marzán, *ACS Nano*, 2010, **4**, 3591–3605.

101. J. J. De Yoreo, P. U. P. A. Gilbert, N. A. J. M. Sommerdijk, R. L. Penn, S. Whitelam, D. Joester, H. Zhang, J. D. Rimer, A. Navrotsky, J. F. Banfield, A. F. Wallace, F. M. Michel, F. C. Meldrum, H. Colfen and P. M. Dove, *Science*, 2015, **349**, 6760-6765.

102. A.-W. W. Xu, Y. R. Ma, H. Colfen and H. Coelfen, *J. Mater. Chem.*, 2007, **17**, 415–449.

103. H. Cölfen and M. Antonietti, *Angew. Chemie - Int. Ed.*, 2005, **44**, 5576–5591.

104. Y. Kim, A. S. Schenk, J. Ihli, A. N. Kulak, N. B. J. Hetherington, C. C. Tang, W. W. Schmahl, E. Griesshaber, G. Hyett and F. C. Meldrum, *Nat. Commun.*, 2014, **5**, 1–14.

105. Y. Liu, Y. Zhang and J. Wang, *CrystEngComm*, 2014, **16**, 5948–5967.

106. V. Lauth, B. Loretz, C. M. Lehr, M. Maas and K. Rezwan, *Chem. Mater.*, 2016, **28**, 3796–3803.

# 3. Colloidal stability of engineered nanoparticles

*Overview: This chapter introduces the concept of the DLVO theory, which describes the interparticle interactions in aqueous solutions. The theory uses the van der Waals and electrostatic forces to estimate the stability of a suspension. Moreover, it describes the formation of surface charge due to ionization of surface groups and relates it to the zeta-potential and colloidal stability.*

## 3.1. Introducing the DLVO Theory

Understanding the interactions between particles in aqueous solutions is of importance in material science, as it allows researchers to understand and better control the stability of particles in a medium by improving surface charge densities and by particle surface functionalization.[1] The DLVO theory treats the colloidal stability in terms of the balance of attractive van der Waals forces and repulsive electrical double-layer forces.[2] With the superposition of these forces, both the stability and aggregation behavior in aqueous solutions can be estimated.[2] In practical terms, dynamic light scattering (DLS) experiments can be used to monitor the particle size and zeta-potential, and the results are used to validate the DLVO theory. The original DLVO theory does not encompass all forms of interactions though. For a better correlation between theory and experimental data, other repulsive forces, e.g. hydration forces, as well as specific attractive forces (e.g. depletion, hydrophobic or magnetic forces) are considered in the extended DLVO theory.

## 3.2. Total energy of interaction

The DLVO theory, first defined by Derjaguin, Landau, Vervey and Overbeek, was developed to describe the colloidal stability and aggregation of a suspension. This theory is used to rationalize the forces acting on particles and surfaces[3] based on two additive contributions: van der Waals and double layer interactions.

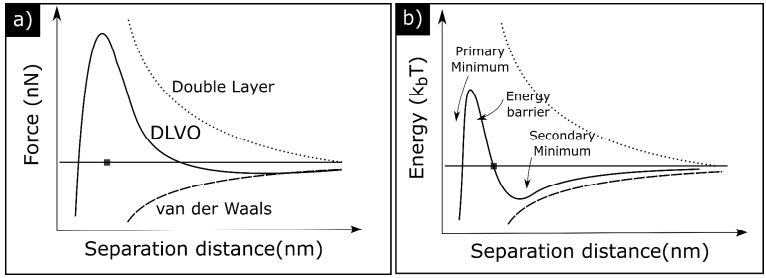


**Figure 3.1:** Illustration of forces (a) and potential energy (b) between two positively-charged particles as a function of the separation distance. Adapted from [5].

The van der Waals attractive force ($W_{vdW}$) results from the interaction of induced, instantaneous, or permanent dipoles generated at the inter-atomic bonds, which can destabilize a colloidal system. The total $W_{vdW}$ is referred to as the sum of three types of dipole-dipole interactions (Keesom force), dipole induced dipole interactions (Debye force), and fluctuating dipole-induced dipole interactions (London force).[4] The $W_{vdW}$ can be simplified as: $W_{vdW} = -\frac{H}{12\,\pi h^2}$, where $H$ is the Hamaker constant and $h$ defines the distance between the particles. The Hamaker constant depends on the material and medium properties[2] and can be experimentally determined by surface force apparatus with typical values ranging around $10^{-21}$ to $10^{-19}$ J.

The double layer interaction ($W_{dl}$) act as a repulsive force and with that, helps the stabilization of a suspension. Most particles in water environments carry some surface charge due to the ionization or dissociation of surface groups. The overlapping of the electric double layer of two particles induces a repulsive force caused by osmotic interactions between conterions.[4] This can be approximated as $W_{ld} = -\frac{2\,\sigma_+\sigma_-}{\varepsilon_0\varepsilon\kappa}\exp(-\kappa h)$, in which $\sigma_+$ and $\sigma_-$ are the surface charge densities per unit area, $\varepsilon_0$ is the permittivity of vacuum, $\varepsilon$ the dielectric constant of water and $\kappa$ the inverse Debye length. The latter is given by $\kappa^{-1} = \frac{0.3\,nm}{\sqrt{I}}$, where I is the ionic strength of the solution.

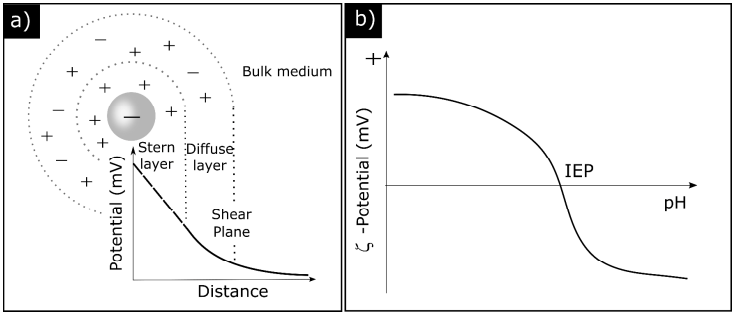


**Figure 3.2:** a) Illustration of the electric double layer model showing the Stern, the Diffuse layer, as well as the shear plane where the zeta-potential is measured. Adapted from [4]. b) Representation of the zeta-potential of $CaCO_3$ particles dispersed in ultra-pure water. The isoelectric point (IEP) represents the pH in which the net charge is equivalent to zero. Adapted from [7].

The combination of these forces can be viewed in terms of the interparticle forces (nN) or potential energy ($k_bT$) (Figure 3.1). Positive forces and potential energies represent repulsive interactions, which provide the stabilization for particles dispersed in water. Accordingly, at infinity and at short distances, van der Waals attractive forces dominate the interactions, while at intermediate distances, the double layer forces are more pronounced. Looking at the potential energy (Figure 3.1b), there are two regions where energy is minimized, which correspond to the points where the net forces are equal to zero. The first one is referred to as the primary minimum and at larger distances, there is the secondary minimum. The energy minima depict particle distances where flocculation or aggregation can occur, whereas the energy maximum represents the energy barrier that prevent particles from coming into contact.[4] To provide colloidal stability, it is necessary the energy maximum to be much larger than the thermal energy of the particles, which usually is in the order of magnitude of $k_bT$.[1]

According to DLVO theory, there is a dependency between the balance of forces and the ionic strength due to screening effects caused by counter ions present in solution.[2,5] At low ionic strength or high surface charge densities, the repulsive forces are less screened and the interaction is dominated by the double layer contribution. At high salt levels, the interaction is dominated by the attractive van der Waals forces,[2] which explains the poor stability in a high ionic concentration medium. In this context, the insight provided by the DLVO theory allows researchers to better control the stability of particles by improving surface

charge densities, changing the environmental conditions or functionalizing the particle surface.

### 3.3. The electric double layer and zeta-potential

Inorganic colloidal particles establish a surface charge in aqueous media.[6] Usually, the protonation or deprotonation of surface groups as a result of the environmental pH is one of the different mechanisms responsible for inducing the surface charge. As reviewed elsewhere,[4] oxide particles present hydroxyl groups at their surface that can deprotonate and establish negative charges, or protonate, yielding positive charges. Similarly, amino groups can protonate and carboxyl groups deprotonate, leading to positively charged $-NH_3^+$ and negatively charged $-COO^-$ groups.

As a result from the colloidal surface charge, an electric field is established around colloidal particles in aqueous solution.[4] This is able to trap a layer of oppositely charged counter-ions around the particles, commonly known as electric double layer (Figure 3.2a). This double-layer is comprised of a first layer of counter-ions, the so-called Stern layer, and the Diffuse layer, which consists of both mobile cations and anions. A common parameter to characterize colloids in solution is the zeta potential ($\Psi_\zeta$). This parameter is represented in Figure 3.2a, as the electrostatic potential measured at the shear plane between the double layer and the bulk medium.[4]

For particles with amphoteric surfaces, the surface charge of a particle is dependent on the pH of the suspension (Figure 3.2b).[4] At pH values near the isoelectric point (IEP), which is defined as the pH in which the charge is equal to zero, the overall surface charge reduces and with that, so does the repulsive $W_{dl}$ force which leads to particle aggregation. For $CaCO_3$ in Millipore water, the measured IEP is around 6, proving that a stable suspension is just possible at basic environments. In acid conditions, as previously shown, the particles rapidly dissolve. Moreover, the stability of a suspension is commonly associated by high zeta potential, with a magnitude higher than 30 mV.

## 3.4. References

1. T. Tadros, *Colloid Stab. role Surf. forces, Part I*, 2010, **1**, 1–22.

2. Y. Xia, B. Gates, Y. Yin and Y. Lu, *Adv. Mater.*, 2000, **12**, 693–713.

3. G. Trefalt, F. J. M. Ruiz-Cabello and M. Borkovec, *J. Phys. Chem. B*, 2014, **118**, 6346–6355.

4. T. L. Moore, L. Rodriguez-Lorenzo, V. Hirsch, S. Balog, D. Urban, C. Jud, B. Rothen-Rutishauser, M. Lattuada and A. Petri-Fink, *Chem. Soc. Rev.*, 2015, **44**, 6287–6305.

5. J. N. Israelachvili, *Intermolecular and Surface Forces*, 2011, vol. 53.

6. A. E. Nel, L. Mädler, D. Velegol, T. Xia, E. M. V Hoek, P. Somasundaran, F. Klaessig, V. Castranova and M. Thompson, *Nat. Mater.*, 2009, **8**, 543–557.

7. V. Vergaro, P. Papadia, S. Leporatti, S. A. De Pascali, F. P. Fanizzi and G. Ciccarella, *J. Inorg. Biochem.*, 2015, **153**, 284–292.

# 4. $CaCO_3$ particles and their cellular interactions

*Overview: Chapter 4 first describes the principles of drug delivery and then highlights relevant papers that use calcium carbonate colloids as delivery vehicles, followed by a description of the colloidal properties, like size, morphology, and surface charge, and their influences on the cellular response. In addition, the formation of protein-corona is described and its effect in the particle stability is highlighted. Finally, a brief overview is also given on the surface functionalization of $CaCO_3$ carriers.*

## 4.1. Principles of drug delivery

The development of effective ways to deliver molecules to targeted tissues using nanoparticle systems can improve the therapeutic outcome of several clinical diseases, including cancer,[1,2] cystic fibrosis[3] and other infectious diseases.[4] Over the past 3 decades, researchers assessed the role of nanoparticles in the delivery of proteins, genes and therapeutic drugs.[5] A critical assessment of the results obtained in this field is given in this section, along with a description of drug delivery systems (DDS) for controlled and sustained release, as well as the controversy on the enhanced permeation and retention effect (EPR effect).

The rationale behind the use of nanoparticles as delivery systems comes from the idea of a "magic bullet",[6,7] first idealized by Nobel Prize winner Paul Ehrlich. It describes a drug that is able to selectively target and hinder the growth of infected/tumor cells without harming healthy cells. In a way, a particulate system could potentially do as described as long as its physical and chemical properties are well adjusted. The first strategy is inspired by microorganisms, which are already designed for the interaction with selected cells in our body.[5] By mimicking the physical and chemical properties of virus and bacteria, nanoparticle systems might be able to interact with cells in a similar way. As reviewed by Yoo and colleagues,[5] particle systems are reported to be functionalized with external viral capsid structures and peptides for immune recognition. In this context, Nicolas and co-workers[6] reviewed possible ways for particle functionalization with ligands aiming specific cell targeting. Due to easy functionalization, lipid-based particles emerged as the pharmaceutical vehicle of choice with the approval of several liposomal formulations.[8,9] In addition to lipid, polymers like chitosan and poly(lactate)[6,10,11] also received special attention as they are well tolerated by the body.

Besides the functionalization ability, delivery systems based on the particles also benefits from the protection against premature degradation in the body as well as from the solubilization of hydrophobic molecules, as reviewed by Peer[9] and colleagues. This review also shows that particle distribution can passively target solid tumors by the so called EPR effect.[9] This effect describes the extravasation of particles from "leaky" blood vessels into the tumor tissue. As normal tissues have intact blood vessels, the drainage of particles occurs predominately around solid tumors.[12] Despite a huge body of work based on this effect,[13] the passive targeting still did not translated to clinical formulations.[7,14]

Nanoparticle-based drug delivery systems are designed to release the cargo molecules in a controlled manner, aiming to reach the minimum therapeutic concentration for extended periods.[15] The release of molecules can occur by at least three different mechanisms: *i.* diffusion through the carrier;[16] *ii.* carrier erosion or dissolution;[17] *iii.* osmotic-controlled release, in which the release is controlled by the diffusion of water from the body to the interior of the carrier. In this context, more than one mechanism can occur simultaneously. Attempting to improve on the delivery ability, recent reports show the design of smart nanocarriers based on biodegradable hydrogels,[1,18] lipids and inorganic materials,[14] which are capable of sensing the environment and triggering the release accordingly.[19]

It is worth point out that despite decades of research, the improvements to actual clinical delivery formulations are marginal.[2] Critical assessments on this topic[2,4,20,21] showed that in order to advance on the already established delivery systems, researchers need to focus on improving the encapsulation and delivery efficiencies, targeting abilities, in vitro models and theoretical simulations, and especially, improve clinical trials. In addition, Lepeltier and colleagues[4] and Pelaz and colleagues[20] highlight that the focus of nanoscience should not be limited to cancer research, but also towards infectious diseases and biological devices.

### 4.1.1. Delivery of biomolecules using calcium carbonate colloids

In the case of $CaCO_3$, the potential application as drug delivery system benefits from the high biocompatibility and also the pH-sensitivity of this material.[22] In this section, a literature overview is given on the use of $CaCO_3$ as carriers of large biomolecules and low molecular-weight pharmaceutical agents.

Biomolecules, like amino acids, proteins and peptides, consist of chains of amino acids folded into a specific three-dimensional structure, which provides its biological activity.[23] Due to their biological activity and chemical and enzymatic instability,[24,25] the delivery of biomolecules can be very challenging. The delivery

vehicles provide protection from the environment while also avoiding their degradation and loss of activity.

As reviewed by Sharma and co-workers,[10] biomolecules delivery is a safe approach for treating genetic diseases or cancer and can also be used in vaccination and imaging. $CaCO_3$ sub-micrometer particles (300 nm in diameter) prepared by direct precipitation have shown to improve the delivery of insulin transdermally in both normal and diabetic mice.[26] At the nanoscale, another report[27] shows that 70 nm lipid-coated $CaCO_3$ particles are successfully loaded with a therapeutic peptide by the double-emulsion technique and were tested with a lung cancer cell line. Accordingly, this system can also retard tumor growth in vivo. At the microscale, Fujiwara and colleagues[28] described the synthesis of mesoporous capsules with a diameter of around 5 µm. These particles successful encapsulated and released albumin and lysozyme. Kon et al.[29] reports the synthesis of hybrid particles prepared by the direct precipitation technique which are capable of encapsulating both Amylase and gold nanoparticles. Figure 4.1a displays the sustained release profile of Amylase within 24 hours as well as the calculated enzymatic activity, which remained fairly constant at around 90%. This paper is a prime example on how useful $CaCO_3$ particles can be for the long-term delivery of biomolecules with minimal loss of activity.

The delivery of low molecular-weight drugs can also benefit from the protection and site-targeting offered by nanoparticles, e.g. in cancer treatment.[10] As reviewed by Dizaj and colleagues,[30] calcium carbonate particles have been tested for the encapsulation and release of anti-neoplastic drugs, like doxorubicin,[31-34]

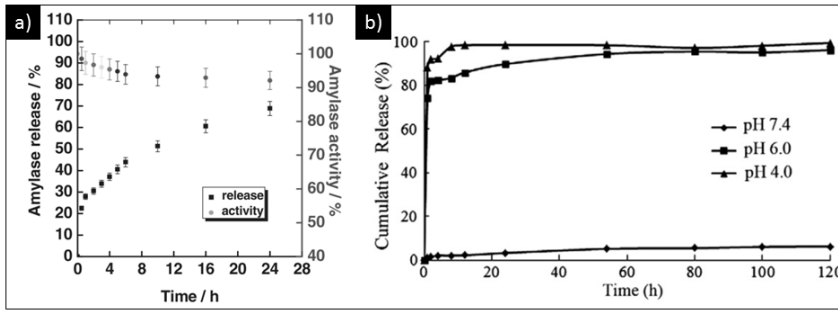


**Figure 4.1:** a) The release and activity profile of amylase from $CaCO_3$ hybrid particles. Reproduced with permission [29]. b) Camptothecin release profile from $CaCO_3$ at different pHs. Reproduced with permission [39].

etoposide,[35] methotrexate,[36,37] and camptothecin.[38,39] Moreover, the sustained release of small anti-microbial gentamicin molecules have also been reported.[40,41] The release profile of gentamicin occurs within 120 hours at pH 7.4 (Figure 4.1b). At pH 6 and 4, the release is completed in under 5 hours. Considering the differences in the release profile that occurs at acidic and neutral pH, the sensitive release can play major role in intracellular delivery to acidic endosomes as well as to acidic cancer microenvironments.

## 4.2. Assessing the in vitro cellular response

In order to gain insight on the effect of the colloidal properties on the cellular response, it is first essential to understand what these responses are and how they can be measured in vitro. Usually, particles are seeded to a model cell line by means of a suspension or an aerosol formulation depending on the desired administration route to be simulated.[42-44] In this thesis, the particles are added to the cells as a particle suspension dispersed in appropriate cell culture medium (Figure 4.2). The particles are subjected to diffusive and sedimentation forces,[45] and with that, are transported to the cells where they can interact and the cellular outcome is assayed. One of the possible cellular responses is cytotoxicity, which is the quality of being toxic to cells. Toxicity can encompass a variety of cell fates, such as necrosis,[46] halt of cell growth and even apoptosis.[44] Among several different techniques to quantify the cytotoxicity of biomaterials, in this thesis, the mitochondrial activity and cell membrane damage assays are chosen. Another possible interaction of nanoparticles and cells is the internalization, which is characterized by the crossing of a cellular membrane.[44] In the case of fluorescently-labeled particles, the cellular internalization can be assessed by means of fluorescence microscopy. Otherwise, the internalized nanoparticles can be analyzed by transmission microscopy of biological samples.[47] Taking into consideration the standard techniques that make possible the assessment of cellular response, most studies have focused on the effect of three colloidal properties: particle size, surface charge and morphology.[13]

### 4.2.1. The effect of particle size

Due to their small size, engineered nanoparticles can interfere with several biological functions, like biodistribution, clearance by macrophages[48] and escape from blood circulation through the leaky tissues in solid tumors.[13] Moreover, particles in the size range of 5 nm to 1 μm can potentially interact with cells as they are in the same size range as the structures that regularly interact with cells, like proteins, extracellular matrix fibers, bacteria and viruses.[49,50] Furthermore, at

this scale, it is recognized that colloids can cross lipid-based membranes,[51] and in some cases, disrupt normal cellular functions.[47]

Recent in vitro studies describe the relevance of particle size on toxicity, cellular uptake and inflammatory response.[52,53] It is reported that the use of latex beads with size ranging from 50 to 500 nm revealed that both the mechanisms of internalization as well as the localization of particles within murine tumor B16 cell line are size-dependent.[54] Accordingly, the beads smaller than 200 nm are internalized by the clathrin-mediated mechanism, while larger particles are internalized via the caveolae mechanism.

Another study on the internalization of polystyrene particles in human astrocytoma and human lung carcinoma cell lines shows that 40 nm particles are internalized faster than 100 nm.[55] Moreover, at the nanometer scale, it is now a general consensus that smaller particles (2 and 6 nm) are internalized at higher quantities than larger (around 15 nm) particles.[56] It is also reported that 64 nm polystyrene nanoparticles can drive the inflammatory response of in A549 cell line to a higher extent than larger 202 and 535 nm particles.[57] All these findings corroborate to the idea that the undesirable effects of engineered nanoparticles, like cytotoxicity and inflammatory responses, are size-dependent.

Considering that the particle size an important parameter to be controlled in

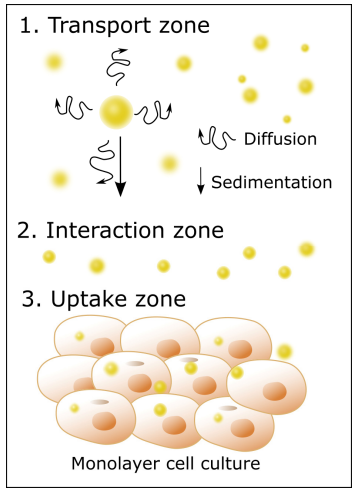


**Figure 4.2:** Representation of the different zones involved in the in vitro assessment of cellular interactions. (1) The particles in a suspension are transported to the monolayer of cells by sedimentation and diffusion forces, where they can interact (2) resulting in either toxicity or improved cell viability. (3) Another possible interaction is the particle internalization within the uptake zone.

delivery system, the particle aggregation in medium should be considered when designing the system. As reviewed by W. Stark,[51] particles in suspension are subjected to Brownian motion and as a result of interparticle collisions, the agglomeration rate, $\frac{dn_t}{dt}$, is primarily dependent on the square of nanoparticle number concentration ($n_t$), according to equation 4:

$$\frac{dn_t}{dt} = -\frac{4\,k_bT}{3\,\mu\,W}{n_t}^2 \qquad \text{Eq. 4}$$

where $W$ is the Fuchs stability ratio, $k_bT$ thermal energy and $\mu$ viscosity. According to equation 4, the agglomeration rate does not directly depend on particle size, but on the number concentration. This explains why nanoparticle suspensions tend to agglomerate faster than microparticle suspensions even when having the same particle mass concentration. The aggregation will reduce the mobility of the particles, and as a result, it can potentially alter the size-dependent toxicity profile described above.

### 4.2.2. The effect of particle shape

Viruses and bacteria are a prime example on how morphology can mediate the in vivo interactions and functions. As reviewed by Albanese,[50] viruses occur in a variety of different shapes, like icosahedral, bullet-shaped, or rod-shaped or have even asymmetric morphology. Accordingly, it is recognized that the geometries dictate their ability to infect specific cell types and may alter their residence time inside the cell.

In regard to synthetic particles, their design and function in vivo can benefit from the understanding gained from biological systems. It is now a general consensus that the uptake of particles by cells scales with aspect ratio.[58,59] Parakhonskiy et al.[60] reports that the frequency of internalized calcium carbonate particles into non-phagocytic cells increases with elongated particles in the micrometer range. The same holds true for the internalization of particles in the nanometer scale. According to Huang and colleagues,[61] mesoporous silica particles with larger aspect ratios (2 – 4), were taken up in larger amounts and had faster internalization rates.

It is worth mentioning that the aforementioned behavior varies according to cell type. In the case of macrophages, the engulfment of anisotropic particles is orientation-dependent. The control over macrophages uptake is especially interesting in pulmonary application, as the major mechanism of defense in the

lungs against exogenously inhaled particles is by macrophage clearance. As reviewed by Champion and colleagues,[62] large polystyrene particles (within 1 to 5 μm) are rapidly taken up by macrophages (Figure 4.3, c). However, particles with anisotropic geometry may hinder the macrophage engulfment depending on the attachment orientation. Moreover, it has been reported[62] that ellipsoidal particles attached to a macrophage at the pointed end are internalized within a few minutes while attached to flat side, the particles are not internalized over extended periods. As a result, the particle anisotropy is a feature that can possibly hinder rapid macrophage clearance of synthetic particles but can improve uptake by non-phagocytic cells.[62,63]

### 4.2.3. The effect of particle charge

The particle charge also plays an important role on cellular influences, as reviewed elsewhere.[64–66] The general consensus dictates that charged particles are more toxic than neutral forms and also that positively-charged particles act more toxic than negatively-charged ones.[64,65] The same holds true for cellular uptake, in which the positively charged particles have enhanced association with the negatively charged cell membranes, which results in particle internalization.[67] It is shown that at the micrometer scale, uptake of polystyrene particles by dendritic cells is improved with particles that display a positive net charge.[68] However, it is worthwhile mentioning that research has also shown that anionic nanoparticles can be internalized at a faster rate than their positive counterparts depending on the mechanisms of internalization.[64] In regard to phagocytic cells, the internalization occurs preferentially with negatively charged particles.[65] This can be associated with the fact that macrophages evolved to ingest of bacteria, which display a net negative charge. Moreover, according to Lee and colleagues,[15] an increase in the magnitude of surface charge also favors the uptake of chitosan nanoparticles by macrophages.

The generalization of such effects may not always hold true as a result of different nanoparticle surface chemistry as well as cell types.[6765] Moreover, the charge of the particles is highly dependent on the pH, ionic strength and on the presence of ions or molecules that can physically adsorb at the particle surface. Consequently, analytical measurements for surface charge determination should be performed in a nutrition medium that mimics the pH as well as the main constituents of serum, like proteins, amino acids and ionic strength.

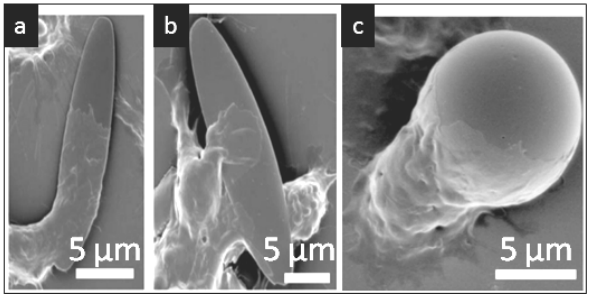


**Figure 4.3:** Macrophages uptake depends on orientation for asymmetrical exogenous particles (a, b), while is just size dependent for spherical particles (c). Reproduced with permission [62].

## 4.3. The formation of protein-corona

Engineered nanoparticles have high zeta-potential in water, which allows them to form stable dispersions. However, upon dispersion in cell nutrition medium, the suspension loses its stability as a result of high protein content and high ionic concentration. The adsorption of charged proteins onto particles is known as protein-corona.[69] Accordingly, the protein-corona can not just affect colloidal stability in medium but also significantly alters the cellular interactions.[70–73]

The process of corona formation occurs due to an increase in the entropy upon adsorption of proteins onto the surface of the particles.[70] As shown in Figure 4.4, proteins attach to or detach from the particle surface with varying rates according to their equilibrium constants ($k_n$).[74] This process can be difficult to predict, as it varies depending on the intrinsic physicochemical properties of the particles, like size, surface functionalization, hydrophobicity and surface roughness.[70] Moreover, this is a dynamic process, both in terms of corona composition and also in regard to the strength to which the proteins are attached to the particles.[70]

In order to gain insight on the variation of surface charge and aggregation behavior as a result of protein-corona formation, Limbach and colleagues[75] assessed the zeta-potential of common engineered oxide nanoparticles in both Millipore water and serum-supplemented nutrition medium. As reported, the colloidal stability scales with the magnitude of the zeta-potential: the higher the zeta-potential, the more stable is the suspension and less likely to occur aggregation. For suspensions in Millipore water at pH 7.4, the zeta-potential covers a wide range of zeta potential, ranging from -25 to +55 mV. However, upon

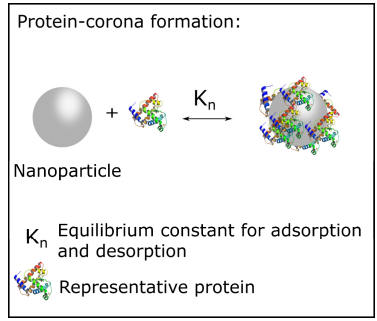


**Figure 4.4:** Representation of protein-corona formation in serum-supplemented medium. Adapted from [74].

redispersion in cell culture medium, the nanoparticles undergo protein adsorption, which results in comparable low surface charge density, under -25 mV, and favors rapid agglomeration.

In regard to the effect on the cellular interactions, positively-charged particles are known to strongly bind to proteins in the medium, which can reduce cellular uptake due to particle aggregation.[67] According to Shahabi and colleagues[76], the presence of protein in cell culture medium caused a shift in surface charge of mesoporous silica particles from +36 mV to -10 mV as a result from the formation of a protein-corona. The particles are internalized at a lower number when compared to the absence of a protein-corona.

In the case of calcium carbonate, the protein corona plays an important role not just on colloidal stability but also on phase-transformation. Svenskaya et al.[77] reports the formation of a protein-corona in a suspension of $CaCO_3$ particles with an average size of 900 nm incubated in cell culture medium supplemented with 10% inactivated fetal bovine serum (FBS). Accordingly, the major highlight of this paper is the description that the particles phase-transformation is suppressed because of the corona surface stabilization up to 168 hours. In a similar study on the composition of the protein-corona, $CaCO_3$ has its isolectric point around pH 6,[78] which means that this material is negatively charged at physiological pH. Consequently, there is a preferential adsorption of positively-charged proteins, like immunoglobulin, apolipoprotein, thrombin and fibrinogen.[79]

## 4.4. Approaches for surface functionalization

As the primary contact between cells and nanoparticles occurs via the particles surface, it is possible to control their interactions by tailoring the surface properties.[71] One interesting example of this interplay can be found in particles delivered by intravenous infusion: functionalized particles with poly(ethylene glycol) (PEG), also referred as PEGylation, can hinder the opsonization and therefore avoid immune recognition and premature clearance.[80] Moreover, the functionalization of particles with antibodies enables active targeting of specific cells by nanoparticles.[80]

Surface modification using calcium carbonate can be complicated, as this material can dissolve at acidic pH or phase-transform to more stable polymorphs in buffers and solvents. Most common techniques used for the functionalization of $CaCO_3$ particles have been reviewed elsewhere,[10,81] and are depicted in Figure 4.5. The methods for surface functionalization can be sorted in three distinct categories: the chemical modification by silane coupling agents or covalent binding (a), the adsorption of polyelectrolytes (b) and the use of additives during mineralization (c).

The coupling of silane agents at the calcium carbonate surface is an efficient method and occurs by a condensation-like polymerization, in which hydroxyl groups at the particle surface react with the coupling agent. In this controlled reaction, the particles are capped with the organic compound. As the organic chains can have different functional groups and chain lengths, this technique is very useful for improving stability in medium as well as for anchoring further functionalization moieties. Silanization is reported to improve colloidal stability by steric hindrance provided by large silane molcules.[82,83] Other functionalization methods based on covalent binding have been reported for $CaCO_3$ particles, for example: the EDC/NHS cross-linking of carboxylates with primary amines to functionalize particles with rabies virus glycoprotein peptide[84] and the biotin-avidin binding method[34] to functionalize the particles with a specific aptamer for cancer cells.

One limitation of the chemical modification technique is that the particles need a high concentration of specific surface groups, otherwise the reactions will not occur or occur at low yields. Moreover, in the case of silanization, due to the monolayer of silane formed around the particles, the nature of the particle is changed, which can affect nanoparticle-cellular interactions and degradability.

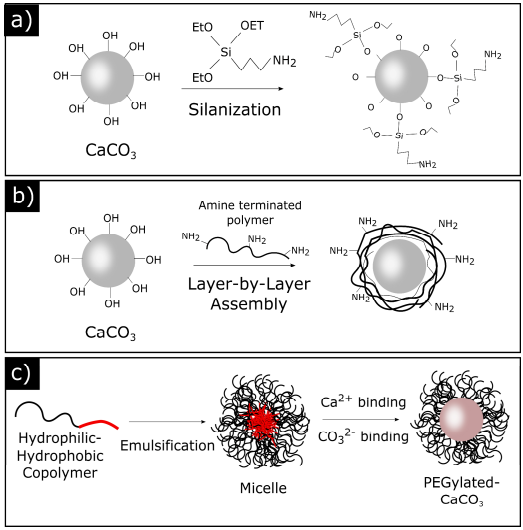


**Figure 4.5:** Surface functionalization approaches for $CaCO_3$ particles: a) Chemical modification by silanization. Adapted from [83]. b) Layer-by-layer adsorption of polyelectrolytes (e.g. poly(ethylenimine)) with opposed charge to the particle surface. Adapted from [90]. c) Modification by inclusion of additives during mineralization. Hydrophilic-hydrophobic copolymers form micelles in water. After mineralization, the hydrophilic tales (poly(ethylene glycol)) provide steric stabilization. Adapted from [88]

Another possible way to modify the surface of particles is based on the physisorption of polyelectrolytes. Poly(ethylenimine) (PEI) was reported to improve the stability of $CaCO_3$ particles in medium upon physisorption.[85] In a similar way, the layer-by-layer technique[86] uses templates for the successive adsorption of polyelectrolytes with opposite charge (Figure 4.5b). The primary aim of this technique is the formation of a cohesive polymeric capsule upon template dissolution. However, if the template is not dissolved, core-shell particles are formed.[60,87] The control of the surface charge by polymer adsorption is reported to improve cellular uptake[60] as well as to regulate hydrophobicity of carriers by adsorption of muco-adhesive polymer and surfactants.[87] As a large variety of organic molecules can be absorbed, they can provide additional chemical activity and a variety of different surface groups for further functionalization. However, due to the weak electrostatic interaction, these adsorbed molecules are likely to desorb in changing conditions.

One of the most promising techniques to functionalize $CaCO_3$ is by using additives during the mineralization process. Different types of additives have been described on Chapter 2. However, now these additives not just control the mineralization but also provide the surface functionality (Figure 4.5c). Copolymers are very useful in this case because one part of the polymer can modify the precipitation while the other provides the surface functional groups. Copolymers like Poly(ethylene glycol)-b-poly(L-aspartic acid) (PEG–PAsp)[88] are reported to both mediate the $CaCO_3$ mineralization and provide the stealth protection of PEG molecules. Similarly, a tri-block copolymer was reported to provide coronal PEG, poly(L-aspartic acid) (PLA) as the crystallization-mediator, and the hydrophobic poly(L-phenylalanine) (PPhe) as the hydrophobic core.[89] The resulting particles are used to deliver hydrophobic docetaxel to a cancer cell line.

## 4.5. Biomedical applications of calcium carbonate particles

A large body of work is being generated with a focus on calcium carbonate colloids for biological applications. Here, a few selected and promising areas of research are highlighted. As shown in Chapter 2, the solubility product of this material greatly increases in acidic environments. The released carbonate ions are studied as a potential pH buffer.[91,92] Som et al.[91] prepared $CaCO_3$ nanoparticles that exhibited the ability to persistently neutralize the extracellular tumor microenvironment. As a result of this pH neutralization, a halt in growth of solid tumors is reported. Following the same idea, Raliya and co-workers[92] showed that vaterite nanoparticles can maintain neutral gastric pH values three times longer than commercially available antacids.

Another topic of research is related the preparation of bioactive scaffolds for osteogenic bone implants and tissue engineering as a result of optimal $CaCO_3$ biodegradation.[93,94] Microparticles are reported to be prepared in bulk quantities and used either as a suspension or shaped into the desired scaffolds. In the case of bone implants,[93] microparticles comprised of both amorphous and vaterite phases, are used to promote osteogenic activity due to the release of calcium ions. It is highlighted that these implants are highly osteogenic when prepared with the pure calcite phase, which turns out to be biologically inert. Moreover, Affolter-Zbaraszczuk and colleagues[94] reported a system for tissue engineering using hybrid organic-inorganic materials with promising build-up of any type of targeted tissue. This system is optimized by the presence of extracellular matrix components like gelatin, hyaluronic acid, fibronectin, which in combination with $CaCO_3$ microparticles allows substantial cell adhesion and growth. An advantage of using

scaffolds prepared out of this material in comparison to hydroxyapatite is the complete degradation within 3 months when placed in a bone defect.[95]

Recently, $CaCO_3$ particles are also studied as an ultra-sound contrast agent. For this application, particles with size ranging from 150 - 220 nm are synthesized either by the direct precipitation technique with addition of block-copolymers[88,96] and alginate[97] or by emulsification.[84] The systems are based on the release of $CO_2$ upon $CaCO_3$ dissolution in acidic environment, e.g. in tumor microenvironments. The released $CO_2$ enhances the ultra sound signal, acting as a contrast agent. Since $CaCO_3$ particles do not normally dissolve at physiological pH, this system holds potential for tumor imaging.

Another potential use of calcium carbonate particles is in the photodynamic and photothermal therapy, which are emerging alternatives for the treatment of tumors and bacterial biofilms.[98] In the photodynamic therapy, a light-sensitive molecule is irradiated with a laser source, which leads to an electronic excitation of the photoactive dye. As a result, singlet oxygen species are produced and elicit cell and bacteria death.[98] Commonly used photosensitizers are chlorin E6[88,99] and sulfonated aluminum phthalocyanines, which are encapsulated within $CaCO_3$ particles and released at the target site.[77] Similarly for photothermal therapy, localized heat is generated by light absorption in the near infrared wavelength, which causes cell death. For that, light sensitive materials are encapsulated, like polyaniline (PANI)[38] or even functional nanoparticles, like iron oxide[100] or gold.[101]

## 4.6. References

1. Z. Fang, L.-Y. Wan, L.-Y. Chu, Y.-Q. Zhang and J.-F. Wu, *Expert Opin. Drug Deliv.*, 2015, **12**, 1943–53.

2. J. H. Adair, M. P. Parette, E. I. Altinoğlu and M. Kester, *ACS Nano*, 2010, **4**, 4967–4970.

3. O. Ciofu, T. Tolker-Nielsen, P. Jensen, H. Wang and N. Hoiby, *Adv. Drug Deliv. Rev.*, 2014, **85**, 7–23.

4. E. Lepeltier, L. Nuhn, C.-M. Lehr and R. Zentel, *Nanomedicine (Lond).*, 2015, **10**, 3147–3166.

5. J.-W. Yoo, D. J. Irvine, D. E. Discher and S. Mitragotri, *Nat. Rev. Drug Discov.*, 2011, **10**, 521–35.

6. J. Nicolas, S. Mura, D. Brambilla, N. Mackiewicz and P. Couvreur, *Chem. Soc. Rev.*, 2013, **42**, 1147–1235.

7. J. W. Nichols and Y. H. Bae, *J. Control. release*, 2014, **190**, 451–64.

8. V. P. Torchilin, *Nat. Rev. Drug Discov.*, 2005, **4**, 145–160.

9. D. Peer, J. M. Karp, S. Hong, O. C. Farokhzad, R. Margalit and R. Langer, *Nat. Nanotechnol.*, 2007, **2**, 751–760.

10. S. Sharma, A. Verma, B. V. Teja, G. Pandey, N. Mittapelly, R. Trivedi and P. R. Mishra, *Colloids Surfaces B Biointerfaces*, 2015, **133**, 120–139.

11. F. Lebre, C. H. Hearnden and E. C. Lavelle, *Adv. Mater.*, 2016, 5525–5541.

12. E. Pérez-Herrero and A. Fernández-Medarde, *Eur. J. Pharm. Biopharm.*, 2015, **93**, 52–79.

13. E. Blanco, H. Shen and M. Ferrari, *Nat. Biotechnol.*, 2015, **33**, 941–951.

14. S. Mura, J. Nicolas and P. Couvreur, *Nat. Mater.*, 2013, **12**, 991–1003.

15. W.-H. Lee, C.-Y. Loo, D. Traini and P. M. Young, *Expert Opin. Drug Deliv.*, 2015, **5247**, 1–18.

16. B. P. Bastakoti, K. C. W. Wu, M. Inoue, S. I. Yusa, K. Nakashima and Y. Yamauchi, *Chem. - A Eur. J.*, 2013, **19**, 4812–4817.

17. Y. Guo, J. Zhang, L. Jiang, X. Shi, L. Yang, Q. Fang, H. Fang, K. Wang and K. Jiang, *Chem. Commun. (Camb).*, 2012, **48**, 10636–8.

18. Y. Qiu and K. Park, *Adv. Drug Deliv. Rev.*, 2012, **64**, 49–60.

19. V. P. Torchilin, *Nat. Rev. Drug Discov.*, 2014, **13**, 813–827.

20. B. Pelaz, C et al., *ACS Nano*, 2017, **11**, 2313–2381.

21. S. Wilhelm, A. J. Tavares, Q. Dai, S. Ohta, J. Audet, H. F. Dvorak and W. C. W. Chan, *Nat. Rev. Mater.*, 2016, **1**, 16014.

22. Y. Boyjoo, V. K. Pareek and J. Liu, *J. Mater. Chem. A*, 2014, **2**, 14270–14288.

23. C. P. Ricardo and A. Teixeira, *Moléculas Biológicas estrutura e propriedades*, .

24. R. Challa, A. Ahuja, J. Ali and R. K. Khar, *AAPS PharmSciTech*, 2005, **6**, E329-57.

25. D. S. Pisal, M. P. Kosloski and S. V. Balu-Iyler, *NIH Public Access*, 2011, **99**, 1–33.

26. M. Higaki, M. Ameyama, M. Udagawa, Y. Ueno, Y. Yamaguchi, Igarashi, T. Ishihara and D. Mizushima, *Diabetes Technol. Ther.*, 2006, **8**, 369–374.

27. S. K. Kim, M. B. Foote and L. Huang, *Cancer Lett.*, 2013, **334**, 311–8.

28. M. Fujiwara, K. Shiokawa, K. Morigaki, Y. Zhu and Y. Nakahara, *Chem. Eng. J.*, 2008, **137**, 14–22.

29. F. Kong, H. Zhang, X. Zhang, D. Liu, D. Chen, W. Zhang, L. Zhang, H. A. Santos and M. Hai, *Adv. Funct. Mater.*, 2016, **26**, 6158–6169.

30. S. M. Dizaj, M. Barzegar-Jalali, M. H. Zarrintan, K. Adibkia and F. Lotfipour, *Expert Opin. Drug Deliv.*, 2015, **12**, 1649–1660.

31. P. Liang, D. Zhao, C. Q. Wang, J. Y. Zong, R. X. Zhuo and S. X. Cheng, *Colloids Surfaces B Biointerfaces*, 2013, **102**, 783–788.

32. J. Li, H. Jiang, X. Ouyang, S. Han, J. Wang, R. Xie, W. Zhu, N. Ma, H. Wei and Z. Jiang, *ACS Appl. Mater. Interfaces*, 2016, **8**, 30027–30036.

33. Y. Zhao, L. N. Lin, Y. Lu, S. F. Chen, L. Dong and S. H. Yu, *Adv. Mater.*, 2010, **22**, 5255–5259.

34. C. Zhou, T. Chen, C. Wu, G. Zhu, L. Qiu, C. Cui, W. Hou and W. Tan, *Chem. - An Asian J.*, 2015, **10**, 166–171.

35. H. Peng, K. Li, T. Wang, J. Wang, J. Wang, R. Zhu, D. Sun and S. Wang, *Nanoscale Res. Lett.*, 2013, **8**, 321.

36. C. F. Dai, W. Y. Wang, L. Wang, L. Zhou, S. P. Li and X. D. Li, *Mater. Sci. Eng. C*, 2016, **69**, 577–583.

37. C.-F. Dai, W.-Y. Wang, L. -Wang, L. -Zhou, S.-P. Li and X.-D. Li, *RSC Adv.*, 2016, **6**, 68335–68340.

38. A. Neira-Carrillo, E. Yslas, Y. A. Marini, P. Vásquez-Quitral, M. Sánchez, A. Riveros, D. Yáñez, P. Cavallo, M. J. Kogan and D. Acevedo, *Colloids Surfaces B Biointerfaces*, 2016, **145**, 634–642.

39. N. Qiu, H. Yin, B. Ji, N. Klauke, A. Glidle, Y. Zhang, H. Song, L. Cai, L. Ma, G. Wang, L. Chen and W. Wang, *Mater. Sci. Eng. C*, 2012, **32**, 2634–2640.

40. A. Lucas-Girot, M. C. Verdier, O. Tribut, J. C. Sangleboeuf, H. Allain and H. Oudadesse, *J. Biomed. Mater. Res. - Part B Appl. Biomater.*, 2005, **73**, 164–170.

41. S. Maleki Dizaj, F. Lotfipour, M. Barzegar-Jalali, M. H. Zarrintan and K. Adibkia, *J. Drug Deliv. Sci. Technol.*, 2016, **35**, 16–23.

42. L. Yildirimer, N. T. K. Thanh, M. Loizidou and A. M. Seifalian, *Nano Today*, 2011, **6**, 585–607.

43. S. Mitragotri, P. A. Burke and R. Langer, *Nat. Rev. Drug Discov.*, 2014, **13**, 655–72.

44. Q. Mu, G. Jiang, L. Chen, H. Zhou, D. Fourches, A. Tropsha and B. Yan, *Chem. Rev.*, 2014, **114**, 7740–7781.

45. M. Horie, H. Kato, K. Fujita, S. Endoh and H. Iwahashi, *Chem. Res. Toxicol.*, 2012, **25**, 605–619.

46. H. Bahadar, F. Maqbool, K. Niaz and M. Abdollahi, *Iran. Biomed. J.*, 2016, **20**, 1–11.

47. S. Moeno, *Chem. Rev.*, 2011, **111**, 3407–3432.

48. A. C. Lima, C. Alvarez-Lorenzo and J. F. Mano, *Adv. Healthc. Mater.*, 2016, **5**, 1687–1723.

49. G. M. Whitesides, *Nat. Biotechnol.*, 2003, **21**, 1161–1165.

50. A. Albanese, P. S. Tang and W. C. W. Chan, *Annu. Rev. Biomed. Eng.*, 2012, **14**, 1–16.

51. W. J. Stark, *Angew. Chemie - Int. Ed.*, 2011, **50**, 1242–1258.

52. M.-C. Senut, Y. Zhang, F. Liu, A. Sen, D. M. Ruden and G. Mao, *Small*, 2016, **12**, 631–646.

53. A. Nel, *Science (80-. ).*, 2007, **311**, 622–627.

54. J. Rejman, V. Oberle, I. S. Zuhorn and D. Hoekstra, *Biochem. J.*, 2004, **377**, 159–69.

55. J. A. Varela, M. G. Bexiga, C. Åberg, J. C. Simpson, K. A. Dawson, M. G. Bexiga and J. C. Simpson, *J. Nanobiotechnology*, 2012, **10**, 39.

56. K. Huang, H. Ma, J. Liu, S. Huo, A. Kumar, T. Wei, X. Zhang, S. Jin, Y. Gan, P. C. Wang, S. He, X. Zhang and X. J. Liang, *ACS Nano*, 2012, **6**, 4483–4493.

57. D. M. Brown, M. R. Wilson, W. MacNee, V. Stone and K. Donaldson, *Toxicol. Appl. Pharmacol.*, 2001, **175**, 191–199.

58. N. P. Truong, M. R. Whittaker, C. W. Mak and T. P. Davis, *Expert Opin. Drug Deliv.*, 2015, **12**, 129–142.

59. K. Nambara, K. Niikura, H. Mitomo, T. Ninomiya, C. Takeuchi, J. Wei, Y. Matsuo and K. Ijiro, *Langmuir*, 2016, **32**, 12559–12567.

60. B. V. Parakhonskiy, M. Zyuzin, A. M. Yashchenok, S. Carregal-romero, J. Rejman, H. Möhwald, W. J. Parak and A. Skirtach, *J Nanobiotechnol*, 2015, **13**, 13–53.

61. X. Huang, X. Teng, D. Chen, F. Tang and J. He, *Biomaterials*, 2010, **31**, 438–448.

62. J. Champion, Y. K. Katare and S. Mitragotri, *J. Control. Release*, 2007, **121**, 3–9.

63. R. Weissleder, M. Nahrendorf and M. J. Pittet, *Nat. Mater.*, 2014, **13**, 125–38.

64. K. Murugan, Y. E. Choonara, P. Kumar, D. Bijukumar, L. C. du Toit and V. Pillay, *Int. J. Nanomedicine*, 2015, **10**, 2191–2206.

65. E. Fröhlich, *Int. J. Nanomedicine*, 2012, **7**, 5577–91.

66. J. Park and W. Lu, *Phys. Rev. E*, 2009, **80**, 2379–2400.

67. C. Graf, Q. Gao, I. Schütz, C. N. Noufele, W. Ruan, U. Posselt, E. Korotianskiy, D. Nordmeyer, F. Rancan, S. Hadam, A. Vogt, J. Lademann, V. Haucke and E. Rühl, *Langmuir*, 2012, **28**, 7598–7613.

68. C. Foged, B. Brodin, S. Frokjaer and A. Sundblad, *Int. J. Pharm.*, 2005, **298**, 315–322.

69. J. Gebauer, M. Malissek, S. Simon, S. Knauer, M. Maskos, R. Stauber, W. Peukert and L. Treuel, *Langmuir*, 2012, **28**, 9673−9679.

70. C. Gunawan, M. Lim, C. P. Marquis and R. Amal, *J. Mater. Chem. B*, 2014, **2**, 2060–2083.

71. D. Walczyk, F. B. Bombelli, M. P. Monopoli, I. Lynch and K. a Dawson, *J. Am. Chem. Soc.*, 2010, **132**, 5761–8.

72. C. D. Walkey and W. C. W. Chan, *Chem. Soc. Rev.*, 2012, **41**, 2780–99.

73. D. Maiolo, P. Bergese, E. Mahon, K. a Dawson and M. P. Monopoli, *Anal. Chem.*, 2014, **86**, 12055–63.

74. F. Darabi Sahneh, C. Scoglio and J. Riviere, *PLoS One*, 2013, **8**.

75. L. L.K., L. Y., G. R.N., B. T.J., H. M.A., M. M., G. D. and S. W.J., *Environ. Sci. Technol.*, 2005, **39**, 9370–9376.

76. S. Shahabi, S. Döscher, T. Bollhorst, L. Treccani, M. Maas, R. Dringen and K. Rezwan, *ACS Appl. Mater. Interfaces*, 2015, **7**, 26880–26891.

77. Y. I. Svenskaya, A. M. Pavlov, D. A. Gorin, D. J. Gould, B. V. Parakhonskiy and G. B. Sukhorukov, *Colloids Surfaces B Biointerfaces*, 2016, **146**, 171–179.

78. V. Vergaro, P. Papadia, S. Leporatti, S. A. De Pascali, F. P. Fanizzi and G. Ciccarella, *J. Inorg. Biochem.*, 2015, **153**, 284–292.

79. J. A. Lee, M. K. Kim, H. M. Kim, J. K. Lee, J. Jeong, Y. R. Kim, J. M. Oh and S. J. Choi, *Int. J. Nanomedicine*, 2015, **10**, 2273–2293.

80. G. L. Szeto and E. B. Lavik, *J. Mater. Chem. B*, 2016, **4**, 1610–1618.

81. S. Kango, S. Kalia, A. Celli, J. Njuguna, Y. Habibi and R. Kumar, *Prog. Polym. Sci.*, 2013, **38**, 1232–1261.

82. Z. Tang, G. Cheng, Y. Chen, X. Yu and H. Wang, *Adv. Powder Technol.*, 2014, **25**, 1618–1623.

83. S. Demir, S. B. Gök and M. V. Kahraman, *Starch/Staerke*, 2012, **64**, 3–9.

84. J. Lee, H.-S. Min, D. G. You, K. Kim, I. C. Kwon, T. Rhim and K. Y. Lee, *J. Control. Release*, 2016, **223**, 197–206.

85. Y. Han and H. Kim, *Mater. Trans.*, 2012, **53**.

86. B. V Parakhonskiy, A. M. Yashchenok, M. Konrad and A. G. Skirtach, *Adv. Colloid Interface Sci.*, 2014, **207**, 253–64.

87. T. N. Borodina, D. B. Trushina, I. V. Marchenko and T. V. Bukreeva, *Bionanoscience*, 2016, **6**, 261–268.

88. D. J. Park, K. H. Min, H. J. Lee, K. Kim, I. C. Kwon, S. Y. Jeong and S. C. Lee, *J. Mater. Chem. B*, 2016, **4**, 1219–1227.

89. B. J. Kim, K. H. Min, G. H. Hwang, H. J. Lee, S. Y. Jeong, E.-C. Kim and S. C. Lee, *Macromol. Res.*, 2015, **23**, 111–117.

90. D. Volodkin, *Adv. Colloid Interface Sci.*, 2014, **207**, 306–24.

91. A. Som, R. Raliya, L. Tian, W. Akers, J. Ippolito, S. Singamaneni, P. Biswas and S. Achilefu, *Nanoscale*, 2016, **8**, 12639–12647.

92. R. Raliya, A. Som, N. Shetty, N. Reed, S. Achilefu and P. Biswas, *RSC Adv.*, 2016, **6**, 54331–54335.

93. E. Tolba, W. E. G. Müller, B. M. Abd El-Hady, M. Neufurth, F. Wurm, S. Wang, H. C. Schröder and X. Wang, *J. Mater. Chem. B*, 2016, **4**, 376–386.

94. C. Affolter-Zbaraszczuk, H. Ozcelik, F. Meyer, O. Gallet, P. Lavalle, V. Ball, C. M. Ghimbeu, P. Schaaf and H. Knopf-Marques, *RSC Adv.*, 2017, **7**, 5528–5532.

95. D. B. Trushina, T. V. Bukreeva, M. V. Kovalchuk and M. N. Antipina, *Mater. Sci. Eng. C*, 2015, **45**, 644–658.

96. K. H. Min, H. S. Min, H. J. Lee, D. J. Park, J. Y. Yhee, K. Kim, I. C. Kwon, S. Y. Jeong, O. F. Silvestre, X. Chen, Y. Hwang, E. Kim, S. C. Lee and M. I. N. E. T. Al, *ACS Nano*, 2015, **9**, 134–145.

97. M. Kim, J. H. Lee, S. E. Kim, S. S. Kang and G. Tae, *ACS Appl. Mater. Interfaces*, 2016, **8**, 8409–8418.

98. M. Epple, K. Ganesan, R. Heumann, J. Klesing, A. Kovtun, S. Neumann and V. Sokolova, *J. Mater. Chem.*, 2010, **20**, 18–23.

99. Z. Dong, L. Feng, W. Zhu, X. Sun, M. Gao, H. Zhao, Y. Chao and Z. Liu, *Biomaterials*, 2016, **110**, 60–70.

100. A. Sergeeva, R. Sergeev, E. Lengert, A. Zakharevich, B. Parakhonskiy, D. Gorin, S. Sergeev and D. Volodkin, *ACS Appl. Mater. Interfaces*, 2015, **7**, 21315–21325.

101. J. Kang, J. Yang, J. Lee, S. J. Oh, S. Moon, H. J. Lee, S. C. Lee, J.-H. Son, D. Kim, K. Lee, J.-S. Suh, Y.-M. Huh and S. Haam, *J. Mater. Chem.*, 2009, **19**, 2902.

# 5. Experimental methods and principles

*Overview: The following chapter describes the characterization techniques utilized in this dissertation as well as highlights the key fundamentals aspects of each method.*

## 5.1. UV-Vis spectroscopy

Ultraviolet-visible spectroscopy is a technique that uses the absorption or the reflectance in the visible range as an analytical method for the quantitative determination of the concentrations of dissolved molecules in a specific medium. In this thesis, this is used for the quantification of calcium ions and proteins in buffers.

### 5.1.1. Quantification of calcium ions in solution

The free calcium ion concentration is quantified using a colorimetric method based on o-cresolphthalein complexone.[1] The kit Fluitest CA-CPC was purchased from Analyticon Biotechnologies AG and assayed using the Multiskan GO device (Thermo Scientific). For that, the suspension to be analyzed was centrifuged at 5000 rpm for 5 minutes to remove dispersed particles. From the centrifuged solution, 10 µL of the supernatant was transferred to a 96-well plate containing

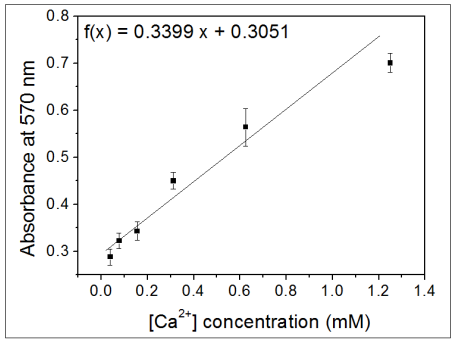


**Figure 5.1:** Concentration curve obtained for free calcium ion detected using Fluitest CA-CPC kit. The curve is prepared by a serial dilution of the standard 2.5 mM acquired with the kit.

50 µL of Reaction Mixture 1 Buffer pH 10.7 (2-Amino-2-Methyl-1-Propanol buffer). Another 50 µL of Reaction Mixture 2 (o-cresolphthalein complexone) was then added to the well plate and shaken for 30 s to allow homogeneous mixing. Under alkaline condition provided by the buffer, the calcium-o-cresolphthalein complex is formed. This compound has a bright purple color and adsorbs at 570 nm.

The absorbance of the resulting complex can be correlated to the calcium concentration with a standard concentration curve, as shown in figure 5.1. According to the company, the absorbance values are stable from 5 minutes to 1 hour after preparation. In chapter 6 and 8, the calcium concentration in the sample is calculated using standard curve by a serial dilution of the standard 2.5 mM acquired with the kit.

### 5.1.2. Quantification of proteins in buffer

Proteins can be quantified in the near UV at 280 nm due to the presence amino acids with aromatic rings and at 200 nm due to peptides bonds.[2] The protein absorbance ($A_p$) can be correlated with the protein concentration described by Lambert-Beer law, $A_p = \varepsilon c d$, where $\varepsilon$ is the extinction coefficient (which varies from protein to protein), $c$ is the protein concentration and $d$ is the length of the cuvette. However, this technique is deemed unreliable as impurities could affect the extinction coefficient and the absorbance intensities.[3] Accordingly, the quantification of protein used in this thesis is based on standard concentration

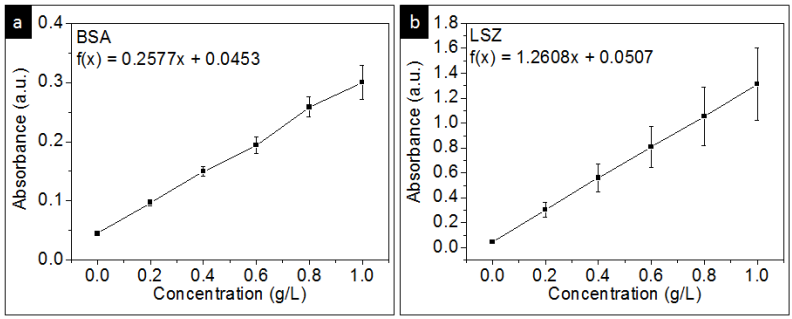


**Figure 5.2:** BSA and LSZ standard curves measured at 280 nm. The equations represent the linear regression used for the calculation of the protein concentration. For all experiments, protein quantification was performed in the linear range of the standard curve.

curves prepared prior to each experiment, as can be seen in Figure 5.2 for bovine serum albumin (BSA) and lysozyme (LSZ). The use of standard concentration curves allows for direct comparison between absorbance and protein concentration. More detail on this technique is described in chapter 6.

## 5.2. Fluorescence spectroscopy

Fluorescence (FL) spectroscopy is an analytical technique that uses the fluorescence properties of molecules in the UV range for the quantitative determination of concentrations[4] or for imaging purposes.[5] All molecules are known to interact with the electromagnetic radiation by the first law of photochemistry.[6] The absorption of photons in a molecule by the irradiating light excites the electrons from the ground electronic state to a higher energy level, the excited electronic state.[4] Collisions with other molecules and internal conversion can cause these electrons return to a ground electronic state of energy, which occurs with the emission of a photon with a lower frequency than the photon absorbed, referred as Stokes shift.[5] This technique is used to assess the release of Rhodamine B from $CaCO_3$ particles, for the quantification of the quantum yield of carbon nanodots (Chapter 7) and for fluorescence imaging (Chapter 8).

### 5.2.1. Quantification of Rhodamine B in PBS

FL spectroscopy is used for quantification of released Rhodamine B (RhB), a positively-charged, hydrophilic dye. Firstly, standard curves are generated by dissolving different amounts of RhB in phosphate-buffered saline (PBS) buffer at pH 7.4. The fluorescence emission intensities of the RhB solutions prepared at different concentrations (4, 8, 16 μM) are recorded at 485/590 nm Excitation/Emission using a microplate reader (Plate Chameleon II model 425-155). The concentration curve is plotted in the Figure 5.3a, as well as the variation in the fluorescence intensities over time is plotted in the Figure 5.3b.

### 5.2.2. Determining the fluorescence quantum yield of carbon nanodots

The fluorescence quantum yield (Q.Y.) is defined as the ratio of photons absorbed and the photons emitted through fluorescence.[7] Accordingly, it describes the probability of the excited state being deactivated by fluorescence rather than by non-radiative mechanisms.[7] For the measurement of the quantum yield of carbon dots (CDs), a comparative method was used.[7] In this method, a standard reference dye[8] with known quantum yield was used to determine the yield of the sample. Here, 4′,6-Diamidin-2-phenylindol (DAPI) was used as reference, which has a

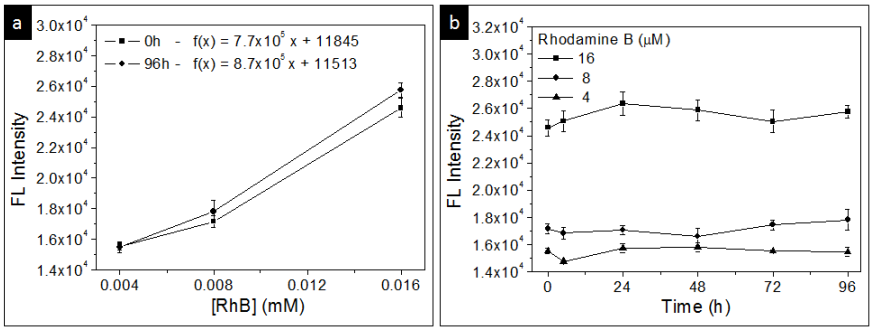


**Figure 5.3:** Concentration curve of Rhodamine B plotted from 0 to 96 hours of incubation in PBS buffer at pH 7.4 (a). The variation in the fluorescence intensity over 96 hours dissolved in the same medium (b).

quantum yield of 4% in water.[9] The DAPI dye has a maximum excitation at 358 nm and emission at 461 nm.

Due to the similar excitation and emission wavelengths to the carbon nanodots, which absorbs at 360 nm and emits at 470 nm, this dye was deemed suitable for the determination of the quantum yield of CDs. The quantum yield measurements were performed in an Infinite 200 PRO device (Tecan). Both the reference material and the sample were prepared at different concentrations in the selected medium, and the absorbance and fluorescence spectrum were recorded (Figure 5.4 a, b). It is important to mention that the absorbance intensity should not exceed 0.1. Moreover, the fluorescence spectrum needs to be integrated over the entire spectrum in order to obtain the overall emission of photons by fluorescence. By plotting the integrated photo emission and the intensity of absorbed photons, a straight line is observed with intercept at (0,0) and slope *m* (Figure 5.4 c). By comparing the slopes, it is possible obtained the Q.Y. of the sample (Figure 5.4 d). In this example, the slope *m* obtained for DAPI is $1x10^8$, while $m = 6x10^6$ for CDs. By comparing the slopes, the calculated value for the quantum yield of CDs is 0.24%.

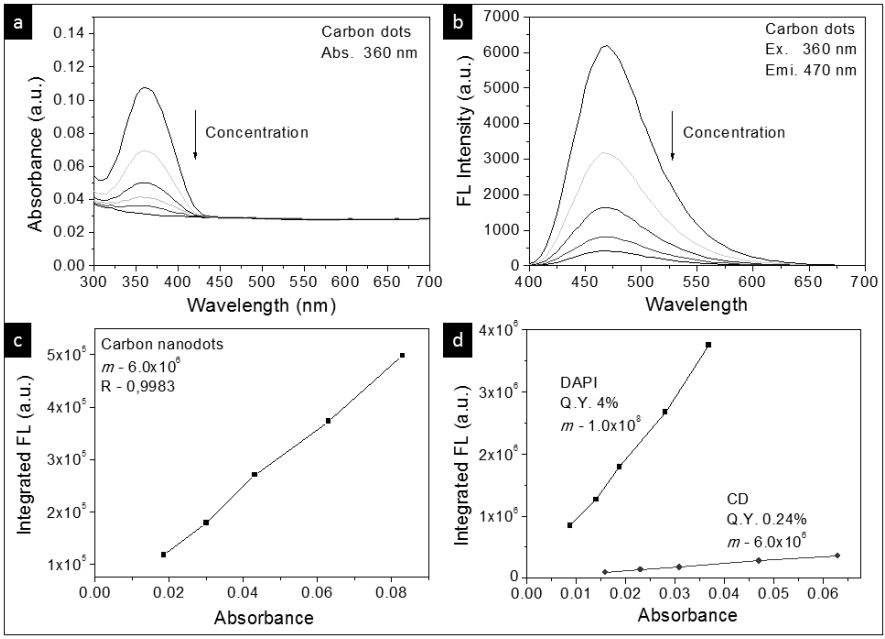


**Figure 5.4:** Quantum yield of carbon dots using DAPI as standard. a) Absorbance measurements at different CDs concentrations. b) FL measurements at different CDs concentrations. c) Slope determination of CDs by plotting the Integrated FL versus the Absorbance. d) Integrated FL versus the Absorbance plots for both DAPI and CDs. dissolved in the same medium (b).

## 5.3. Dynamic light scattering

Dynamic light scattering (DLS) is a method used primarily to determine the particle size distribution and zeta-potential of colloidal dispersions or molecules in medium. For that, a dispersion in water is illuminated with a monochromatic, polarized laser light with a wavelength in the range of 350 to 680 nm. The scattered light intensity is measured by a photon detector either at 173° or 13°.[10] Due to the change in the wavelength that occurs when light is scattered by a particle subjected to Brownian motion, a phenomenon known as Doppler shift, it is possible to measure the diffusion coefficients of the particles. These are then converted to particle size distribution and polydispersity using a correlogram. Moreover, by applying an external magnetic field with a defined strength, it is also possible to measure the electrophoretic mobility of the particles using the Henry

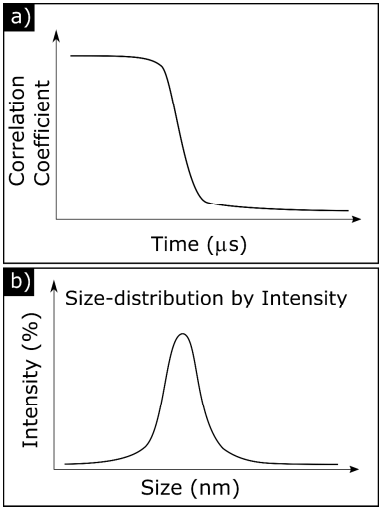


**Figure 5.5:** a) Representative correlogram. b) Illustration of the intensity-averaged size distribution. Adapted from [11].

Equation, and with that, the calculation of zeta potential is possible. These two techniques are used in chapters 6, 7 and 8.

### 5.3.1. Size measurement using DLS

According to [11], by illuminating the suspension with a monochromatic laser light, the scattered intensity is time-dependent when observed on a microsecond time scale. The intensity fluctuations reflect the rate of diffusion of the particles. In this technique, autocorrelation functions are used to extract the time dependence of a signal from the noise. From the decay of the correlation function (Figure 5.5 a), the diffusion coefficient ($D$) is calculated by $\Gamma = q^2 D$, where $\Gamma$ is the exponential decay rate and $q$ is the modulus of the scattering vector. Using the Stokes-Einstein equation $d_H = \frac{kT}{3\,\eta\pi D}$, it is possible to convert the diffusion coefficient into the hydrodynamic radius ($d_H$) taking into account the Boltzmann's constant ($k$), the temperature ($T$) and the medium viscosity ($\eta$). Accordingly, the $d_H$ represents the radius of an equivalent rigid sphere that diffuses at the same rate of the measured sample.

The size distribution curve (Figure 5.5 b) derived from the correlogram can display a large range of particle sizes, from 0.1 nm to 5 µm. The variation in the size distribution can be related to the natural variations in the synthesis processes

or even to particles aggregation. The term that coins the degree of particle-to-particle size variability is known as polydispersity index (PdI), which is dimensionless and ranges from 0 to 1.

### 5.3.2. Zeta-potential measurement using DLS

The concept of zeta-potential was previously described in chapter 3. This section will focus on the measurement of zeta-potential via the dynamic light scattering technique. As described above, DLS measures the particle mobility based on the Doppler shift ($\Delta_f$). By applying an external field, the movement of the particles (electrophoretic mobility, $U_E$) can be calculated by laser Doppler velocimetry (LDV).[11] For that, a pair of mutually coherent laser beams derived from a single source is used. One of the laser beams is set as the reference, while other is passes through the sample. The electrophoretic mobility can be calculated using the Doppler shift equation, $\Delta_f = \frac{2v}{\lambda}\sin\frac{\theta}{2}$, where $v$ is the particle velocity (electrophoretic mobility), $\lambda$ is the laser wavelength and $\theta$ the scattering angle. The $U_E$ can be transformed into zeta-potential ($\zeta$) using the Henry equation, $U_E = \frac{2\,\varepsilon\zeta F(ka)}{3\,\eta}$. The term $F(ka)$ stands for the Henry's function, $\varepsilon$ for the dielectric constant and $\eta$ for viscosity. $ka$ is a measure of the ratio of the particle radius to the Debye length.

## 5.4. Electron microscopy

Due to the limited resolution of conventional optical microscopes, which is determined by the wavelength of visible light, the use of electrons for imaging is a powerful tool. This technique allows for higher resolving power, surpassing the diffraction limit in light microscopy.[12] The basic idea of electron microscopy involves a primary electron beam that is generated by thermionic emission in a cathode filament. The beam is focused by electromagnetic lenses and accelerated towards the specimen. Depending upon the technique, either the backscattered electrons or the transmitted electrons are detected and used for the image rendition. Two types of electron microscopes were used in this thesis: the Scanning Electron Microscope (SEM) and the Transmission Electron Microscope (TEM). This technique is used for the characterization of particle size and morphology in chapters 6, 7 and 8.

### 5.4.1. Scanning electron microscopy

SEM micrographs are created, as the name suggests, by scanning the surface of the sample in a raster scan pattern. According to [12], the primary electrons interact

with the sample within a volume, known as interaction volume. Inside the interaction volume, the incoming electrons can reflect back by elastic scattering. These are known as back-scattered electrons (BSE). Another possible event is the knock-out of electrons from the sample itself. These are known as secondary electrons (SE). Both the BSE and SE are captured by specific detectors rendering two types of images that differ as a result of the nature of each electron type. The SE detector allows for better spatial resolution while BSE for better compositional information, as the electrons are created deeper in the sample.

In order to avoid accumulation of electrons at the sample surface and losses in image quality, conductive samples and sample holders are typically required. As most organic materials and ceramic samples are not conductive, the sputtering of gold or carbon creates a thin layer over the sample surface, which avoids electron accumulation. Another alternative to sputtering is the use of silicon wafers, which allow good electron conductivity.[12]

In all SEM images used in this thesis, SEM samples are prepared as follows. Firstly, a suspension containing $CaCO_3$ particles was centrifuged at 5000 rpm for 10 minutes to concentrate the particles in a pellet. The supernatant was then discarded and the particles were pipetted directly to the sample holder. This holder is comprised of a piece of silicon wafer (4 x 4 mm) glued to the metal holder using a carbon tape. Samples were dried for 1 to 12 h in an oven at 70 °C prior to the analysis to remove any water from the samples. SEM micrographs were taken with a Supra 40 device (Carl Zeiss, Oberkochen, Germany) operated at 1 kV, using the in lens detector.

### 5.4.2. Transmission electron microscopy

In transmission electron microscopy, the electrons transmitted through the specimen are used for the image rendition. As the composition of the sample varies from point to point, so does the electron transmission. Brighter parts of the image indicate higher intensity of transmitted electrons. Given that, regions with higher atomic number scatter more electrons (i.e. by elastic scattering) and therefore appear darker than their surroundings. This is one the phenomena that gives contrast to the TEM micrographs and is known as mass-thickness contrast.[12]

In this thesis, the preparation of samples for TEM is as follows. The particles in suspension were diluted to a concentration of 0.1 g/L in Millipore water. 5 µL of the solutions was pipetted onto a carbon-coated copper grid (PLANO GmbH, Wetzlar, Germany, Mesh 200). The grids were dried for 1 h at room temperature.

TEM micrographs were recorded using a Zeiss EM 900 SN 8246 operating at 80 kV.

## 5.5. X-ray diffraction

X-ray diffraction (XRD) is a nondestructive technique for characterizing crystalline structures. This technique is used in chapters 6, 7 and 8. The principle is based around the constructive interference of a monochromatic beam of X-rays scattered from crystalline materials at specific angles, a phenomenon known as diffraction.[13]

In this technique, X-rays are generated in a cathode tube in which a filament is heated by applying high voltages up to temperatures that cause thermionic emission of electrons. These electrons are accelerated towards a metal target, usually Cu, Fe and Mo. As the electrons hit the target at high energies, they are capable of dislodging inner electrons from the target material. Inside the target, outer electrons migrate to fill in the electron-deficient energy level. This occurs with the emission of characteristic X-rays. Typically, Kα X-ray is emitted and is used for the sample characterization. In this context, K refers to the vacancy in the K-energy level and α means that an electron drops from the nearest energy level, L energy level, to fill the vacancy. Following the The Kα X-ray emission, the beam is filtered to produce monochromatic radiation, collimated and directed to the sample

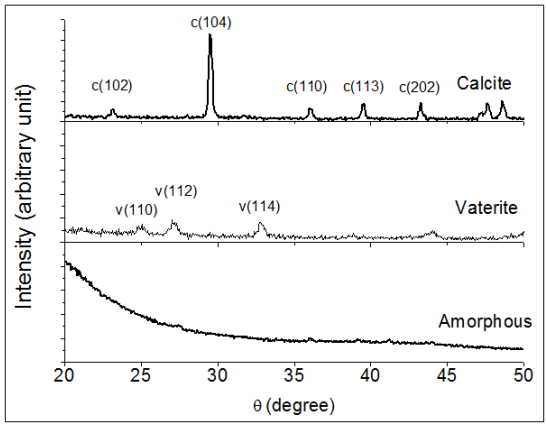


**Figure 5.6:** X-ray diffraction overview of calcite, vaterite and amorphous phases. Amorphous structure shows no reflexes. Crystal phases: c – calcite, v – vaterite.

at varying angles. The angle of incidence will produce constructive interference if the Bragg's law is satisfied, $n\lambda = 2\,d\sin(\theta)$. In this equation, $n$ is an integer, $\lambda$ is the X-ray wavelength, $d$ is the interplanar spacing and $\theta$ is the diffraction angle. As the interplanar distances are specific for each crystalline structure, it is possible to differentiate different materials, crystalline phases, grain size, crystal defects, and even strain.[13]

Figure 5.6 shows typical X-ray pattern of different crystalline phases of $CaCO_3$ (vaterite and calcite) and the amorphous phase. The experiments performed were performed in a Seiffert C300 device (GE Inspection technologies, Germany) operating at 40 mA and 40 kV. The beam was filtered with Ni filter to produce almost monochromatic Cu $K\alpha_1$ and $K\alpha_2$ radiation ($\lambda$=0.1542 nm). Diffraction patterns in the range of 5 to 70° were detected with a holding time of 1 second and a step scan of 0.025°. Powder diffraction files (PDF) of the International Centre for Diffraction Data (ICDD) were used to identify the crystal phases.

## 5.6. Thermogravimetric measurements

The thermogravimetric analysis describes the weight-loss of a sample as a function of increasing temperature, with pre-determined heating rate, final temperature, holding time and cooling rate. This technique provides insight in the chemical reactions and physical transitions that occur in the sample upon heating. Typical reactions, like thermal decomposition and water evaporation, occur with the formation of gaseous products, and therefore, there is an overall weight-loss. Other reactions can promote a gain in weight, e.g. corrosion of metals.[14]

For the measurement, the samples were inserted within a crucible and placed inside a reaction chamber. This chamber can be flushed with different gases. Atmospheric air provides an oxidative atmosphere, while argon and nitrogen, an inert atmosphere is created. The weight of the sample was recorded as temperature increases and significant loss or gain in weight due to decomposition, oxidation, or loss of moisture can be detected. In chapters 7 and 8, the samples were tested using a STA 503 device (Bähr Thermoanalyse GmbH) heated up to 750 °C with a heating rate of 4 °C/min and flushed with 2 L/min of atmospheric air.

## 5.7. Gas adsorption for determination of Specific Surface Area

Gas adsorption measurement is a common technique for the characterization of surface area and pore size distribution of samples. Brunauer, Emmett, and Teller first described the fundamentals for the determination of the specific surface area (SSA) based on gas adsorption.[15] This technique relies on the existence of a

dynamic equilibrium between free and adsorbed gas and that the covered surface is proportional to the partial pressure of the free gas.[16] Commonly, the surface area is determined by volumetric measurement of nitrogen adsorption isotherms. For that, nitrogen is added to a chamber containing the sample to be analyzed, and the adsorbed amount of nitrogen is determined at various relative pressures ($p/p_0$) at -196 °C. Based on the physisorption isotherm to form a monolayer of Nitrogen atoms and on the area occupied by a single atom, the SSA can be determined as: $SSA = \frac{V_m N a \rho}{M}$, where $V_m$ is the volume of nitrogen molecule, $N$ is the Avogadro's number, $a$ is the cross-sectional area of the nitrogen molecule, $\rho$ is the density and $M_w$ is the molecular weight.[17] In chapters 7 and 8, the measurements of adsorption isotherms and the SSA calculation were obtained using a BELSORP 18-3 (Bel Inc., Japan). Prior to the adsorption measurements, all samples were out-gassed for 24 hours at 100 °C under argon.

## 5.8. In vitro cell culture experiments

Normal cells have a finite life span of 20 to 100 generations due to the action of senescence genes, whose products hinder cell cycle progression. This factor made the in vitro experiments a very laborious technique for decades. However, by inactivating a number of cell cycle regulatory genes, it is possible to cultivate specific cell lines continuously, without the need of collecting tissue from patients. These genetically modified cells are known as immortalized cell lines and completely changed the way cell culture experiments are performed.[18] Recently, the in vitro experiments using immortalized cells lines became the standard technique to analyze the biomaterial-cellular interactions.

In vitro studies have a much lower complexity as they are performed in the absence of the physiological responses. In addition, the regulatory rules around in vitro experiments are less strict, which makes this technique an essential tool in the assessment of cytotoxicity and cellular internalization.[19,20] In chapter 7, the adenocarcinomic human alveolar basal epithelial cell line (A549) was used as model to evaluate the in vitro toxicity of $CaCO_3$ particles. In chapter 8, the cell line of choice is the human osteoblast cell line (HOB). Different cell lines were used because the experiments were performed in different institutes, which established different research interests. At the *Helmholtz-Institut für Pharmazeutische Forschung Saarland* (HIPS), research focuses on the understanding and overcoming of the pulmonary barrier and therefore the use of the human alveolar cell line is more representative. On the other hand, the *Advanced Ceramics Group* focuses on the synthesis and application of ceramic materials for both mechanical and biological applications, especially towards bone and tooth research.

### 5.8.1. Cell culture of immortalized, mammalian cell lines

For the HOB cells, the cells were cultured in DMEM supplemented with 10% heat-inactivated FCS and 1% antibiotics/antimycotics (AB/AM) in a cell incubator (C200, Labotect Labor-Technik-Göttingen, Germany) at 37 °C, 10% $CO_2$ and 95% RH. The cells were cultured in 75 $cm^2$ cell culture flasks until they were 80% confluent. For sub-culturing, cells were trypsinized with 5 mL of Trypsin-EDTA. After 30 seconds, 5 mL DMEM + FCS (10%) + AB/AM (1%) was added to stop the trypsinization. The total volume was transferred to a 50 mL Falcon tube, centrifuged at 4000 rpm for 6 minutes to concentrate the cells in a pellet form. The cells were then redispersed in fresh 5 mL DMEM + FCS (10%) + AB/AM (1%) and seeded into 75 $cm^2$ cell culture flasks. For the experiments with nanoparticles, the cells were then trypsinized for 30 seconds with Trypsin-EDTA, dispersed in DMEM + FCS (10%) + AB/AM (1%) and seeded in wells of 24-well polystyrene plate (NUNC, Fischer Scientific, Germany) at a cell density of $2x10^4$ cells per well. On the following day, the $CaCO_3$ suspension in DMEM was added to the well-plate and incubated for 24 h. In addition, for WST-1 assay, cells grown in culture medium were set as high control (100% cell viability), and others incubated with Triton X- 100 (2%, w/v) were used as low control (0% cell viability). For the LDH assay, the cytotoxicity was calculated relative to Triton X-100 as high control and cells in culture medium as low control. Samples were measured in triplicates and evaluated as mean and standard deviations (SD).

For the experiments with the A549 cell line, the cells were cultured in RPMI supplemented with 10% FCS. One day prior to experiments, the cells were detached and seeded in a 24-well plate at a density of $1x10^4$ cells per well. On the following day, the suspensions of $CaCO_3$ in HBSS were added and incubated for 4 h. In addition, for the MTT assay, cells grown in culture medium were set as high control (100% cell viability) and others incubated with Triton X-100 (2%, w/v) were used as low control (0% cell viability). For the LDH assay, the cytotoxicity was calculated relative to Triton X-100 as high control and cells in culture medium as low control. Samples were measured in triplicates and evaluated as mean and standard deviations (SD).

### 5.8.2. Bioanalytical tools to assess in vitro colloidal toxicity

In vitro studies allow researchers to assess the impact of colloidal systems in a cellular model, in which the interactions are limited and simplified to one immortalized cell line, but still can give a representative assessment on whether the particles-cellular interactions occurs in a positive way or shows possible signs of toxicity, prior to the exposure in vivo.[21] The cellular response in the in vitro studies

can be assessed by several analytical tools. Most common ones are the cellular damage indicated by reduction in metabolic activity and the leakage of plasma membrane due to membrane rupture. As the toxicity can be a function of cell type, particle concentration and exposure time, these variables are fixed throughout the experiments, allowing high reproducibility of the results.[21]

The leakage of plasma membrane can be used to assess the membrane integrity via the LDH assay (Figure 5.7a). Upon rupture or damage of the membrane, the cytosolic enzyme Lactate dehydrogenase (LDH) is released into the cell culture medium. The released LDH can be quantified by a coupled enzymatic reaction, in which the LDH catalyzes the conversion of lactate to pyruvate via $NAD^+$ reduction to NADH. Diaphorase (an electron mediator provided in the kit) uses NADH to reduce a tetrazolium salt (INT) to a red-colored formazan product. Formazan can be quantified with a colorimetric assay at 490nm. The concentration of formazan is directly proportional to the amount of LDH released to the medium and therefore, cytotoxicity.[21]

The tetrazolium salt (WST-1 or MTT) technique is another colorimetric assay used for the quantification of cell proliferation, viability and cytotoxicity (Figure 5.7 b). This assay is also based on the cleavage of WST-1 salt to soluble formazan by a complex cellular mechanism that occurs primarily at the cell surface by the succinate-tetrazolium reductase system, which belongs to the respiratory chain of the mitochondria, and is only active in metabolically intact cells. Therefore, the amount of formazan dye formed directly correlates to the number of metabolically

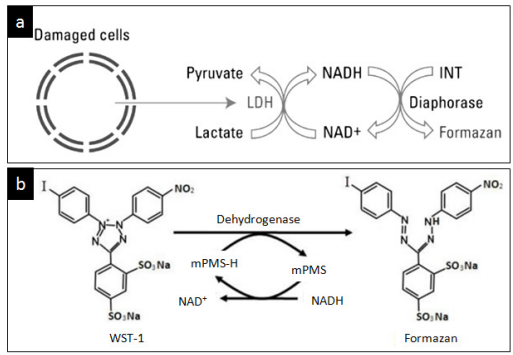


**Figure 5.7:** a) Membrane integrity measured by LDH assay. b) Cell viability measured by WST-1 or MTT assays. Adapted from datasheet provided by the manufacturers: a) Thermo Fisher, b) Roche Deutschland Holding GmbH.

active cells in the culture.[21] A more detailed description of the colorimetric assays results can be found in chapters 7 and 8.

### 5.8.3. Cellular uptake by TEM

The estimation of cellular uptake of particles within cells can be performed by fluorescence techniques, in which both the particles and the cells are fluorescently labeled. This allows for the precise location particles agglomerates within endosomes, which are also labeled with fluorescent LyzoTrackers. However, as the particles used in this these studies are not fluorescently labeled, cellular uptake studies were analyzed by means of TEM.[19] For that, osteoblasts cells treated with $CaCO_3$ particles for 24 hours were washed once with PBS, detached with Trypsin/EDTA and transferred to 2 mL Eppendorf cups. The cups were centrifuged at 6000 rpm for 6 min, fixed with standard 2.5% glutaraldehyde, 2.5% formaldehyde in 0.1 M Na-cacodylate for 1 hour at RT. After removal of the fixative, the cells were washed several times with phosphate buffer and post-fixed with osmium tetroxide solution for 1 hour at RT. The black pellet was washed twice and dispersed in 2% agar (Sigma-Aldrich) in Millipore water, and allowed to solidify at 4°C. The pellet in agar was cut into squares of about 1 mm wide. The blocks were dehydrated in a graded series of ethanol (twice for 5 minutes in 30% and 50% ethanol, 3 times for 10 minutes in 70%, 90% and twice for 15 minutes in 100% ethanol). Blocks were embedded in Epon 812. Ultrathin sections were taken with an ultramicrotome (Ultracut R, Leica, Wetzlar, Germany). In this study, surface markers, like uranyl acetate or ruthenium red, were not used, as the purpose of this experiment aimed at the visualization of internalized particles and not the visualization of intracellular membranes. A more detailed description of the particle internalization result can be found in chapter 8.

### 5.8.4. Statistical analysis

Quantitative data of cell viability and LDH activity are given as mean ± standard deviation of values obtained in three independently performed experiments. The statistical analysis is performed by two-tail-test analysis with unequal variances. P-values below 0.05 are considered to be statistically significant.

## 5.9. References

1. P. Gosling, *Ann. Clin. Biochem.*, 1986, **23**, 146–156.

2. E. Layne, *Methods Enzymol.*, 1957, **3**, 447–454.

3. G. C. Webster, *Biochim. Biophys. Acta*, 1970, **207**, 371–373.

4. J. R. Lakowicz, *Principles of Fluorescence Spectroscopy Principles of Fluorescence Spectroscopy*, 2006.

5. J. W. Lichtman and J. A. Conchello, *Nat. Methods*, 2005, **2**, 910–919.

6. P. Suppan, *Principles of photochemistry*, Chemical Society, 1972.

7. A. T. R. Williams, S. A. Winfield and J. N. Miller, *Analyst*, 1983, **108**, 1067–1071.

8. A. M. Brouwer, *Pure Appl. Chem.*, 2011, **83**, 2213–2228.

9. M. Li, R. S. Wu and J. S. C. Tsai, *Bioorganic Med. Chem. Lett.*, 2003, **13**, 4351–4354.

10. R. Borsali and R. Pecora, *Soft-Matter Characterization*, Springer Sciente+Buisiness Media, 2008.

11. S. McNeil and E. Scott, *Characterization of nanoparticles intended for drug delivery*, Humana press, 2011.

12. R. F. Egerton, *Physical Principles of Electron Microscopy*, 2005, vol. 24.

13. A. A. Bunaciu, E. G. Udristioiu and H. Y. Aboul-Enein, *Crit. Rev. Anal. Chem.*, 2015, **45**, 289–299.

14. T. Technique, *Analyst*, 1963, **88**, 906–924.

15. S. Brunauer, P. H. Emmett and E. Teller, *J. Am. Chem. Soc.*, 1938, **60**, 309–319.

16. K. S. W. Sing, D. H. Everett, R. a. W. Haul, L. Moscou, R. a. Pierotti, J. Rouquérol and T. Siemieniewska, *Pure Appl. Chem.*, 1982, **54**, 2201–2218.

17. K. Meyer, P. Lorenz, B. Bohlkuhn and P. Klobes, *Cryst. Res. Technol.*, 1994, **29**, 903–930.

18. J. R. Masters, *Nat. Rev. Mol. Cell Biol.*, 2000, **1**, 233–236.

19. H. Plattner and J. Hentschel, *Zellbilogie*, 2011.

20. R. I. Freshney, *Culture of Animal Cells: a manual of basic technique and specialized applications*, John Wiley & Sons, Inc., 2010.

21. G. Thrivikraman, G. Madras and B. Basu, *RSC Adv.*, 2014, **4**, 12763.

# 6. Coacervate-directed synthesis of $CaCO_3$ microcarriers for pH-responsive delivery of biomolecules

## 6.1. Introduction

*Abstract: We report the synthesis of pH-responsive microcarriers via the combination of complex coacervation and mineralization of calcium carbonate ($CaCO_3$). Positively and negatively charged proteins (bovine serum albumin (BSA) and lysozyme (LSZ)) form electrostatic complexes with poly(acrylic acid) sodium salt (PAANa) and calcium ions in an aqueous solution, leading to the formation of spherical coacervate droplets. By addition of sodium carbonate, the protein-loaded droplets are mineralized into stable $CaCO_3$ microcarriers. Since this inorganic material exhibits high solubility in acid, the release of protein from the carriers can be controlled via the pH of the environment. The process results in the successful generation of bulk amounts of monodispersed and colloidally stable microspheres with diameters as small as 300 nm. As the entire synthesis takes place under aqueous conditions, coacervate-directed encapsulation is suitable for sensitive active agents. Accordingly, the method presents a promising approach to synthesize pH-responsive microcarriers for drug delivery applications.*

Nanocarriers have established their place in biomedical applications as imaging and delivery vehicles.[1] Recently, several types of nano-based carriers are entering clinical trials.[2] However, due to restrictions on both ligand recognition and enhanced permeability and retention (EPR) effect, as well as the formation of complex nanoparticle coronas, nanosized drug carriers still face critical barriers for the translation into clinics.[3,4] In order to enhance bioavailability of drugs at the disease site, it is highly desirable to include stimuli responsive properties in the carriers.[1] The ability to trigger the release of active agents in response to endogenous changes can be largely exploited for the treatment for neoplastic diseases.[4] In this context, we designed a bio-inspired strategy for synthesizing pH-responsive microcarries based on the combination of two well-studied approaches: complex coacervation and the mineralization of calcium carbonate.

Besides lipids, most drug nanocarriers are based on polymeric materials,[2] due to their diversity, flexibility in synthesis methods and easy functionalization.[5] Amongst the various approaches for encapsulating active agents, coacervation has been used successfully for a long time, starting with the first description of the phenomenon by Bungenberg de Jong in 1929.[6] Two main types of coacervation

have been described and differ by the phase separation mechanism. In simple coacervation, the mechanism involves the partial desolvation or dehydration of macromolecules.[5,7] Complex coacervation, on the other hand, is induced by electrostatic interaction and comprises two or more oppositely charged colloids. Both techniques are widely used in the food industries e.g. in order to retard the oxidation of fish oil,[8] or in cosmetics to encapsulate antioxidant oils.[9] Recent research reported the use of complex coacervation to encapsulate and deliver growth factors,[10] genes[11,12] as well as proteins.[13] Furthermore, coacervates are currently being investigated for their role in protocell formation and as models of protocell assembly.[14] Several advantages arise from the coacervation method, for example the good encapsulation efficiencies,[13] the ability of co-encapsulation and the conjugation of ligands for targeting approaches.[11] The major drawback of this approach is the high instability of the complexes which might necessitate the use of potentially toxic stabilizers[15] or cross-linkers.[16] Moreover, in order to introduce pH-responsive behavior to the coacervates, additional molecules might have to be added. For instance, Pyranine-3 was used to produce pH sensitive microcapsules based on the self-assembly of nanoparticles on the surface of coacervate droplets.[17]

By mineralizing the coacervates with inorganic materials that have high solubility in acid while being stable at neutral and basic pHs, it is possible to stabilize the coacervates, as well as to introduce pH-responsive behavior. One material that suits this purpose is calcium carbonate ($CaCO_3$). It has long been suggested as a drug carrier due to its biocompatibility and biodegradability, low cell cytotoxicity and cost-effectiveness.[18] One common procedure for encapsulation and sustained release of biomolecules with $CaCO_3$ is the direct crystallization method.[19–21] The incorporation of proteins is achieved by physical adsorption onto the synthesized crystals.[19–21] The main characteristics of the produced carriers are the large particle size (1-5 μm), crystalline polymorphism and highly porous structure.[21] Some disadvantages arise from this technique, i.e. the crystalline structure is subject to recrystallization in water if not well stabilized and might lead to changes in shape or polymorphism.[20] Calcium carbonate nanoparticles produced by this technique are often used as templates to synthesize layer-by-layer polymer microcapsules.[19]

Another method for the synthesis of $CaCO_3$ particles that are loaded with active agents is co-precipitation. Here, the precipitation of calcium carbonate is initiated in a solution that already contains the molecules to be encapsulated, e.g. anti-inflammatory drugs,[22] hormones,[23] proteins,[20] genes[24–26] and antigens.[27] The morphology of products prepared via co-precipitation is rather heterogeneous, featuring macrosized plates or rods[22] as well as nanosized particles.[23] Emulsion-based co-precipitation has also been used to encapsulate pesticides,[28] genes[29] and

growth factors.[30] In this approach, emulsions containing calcium chloride, surfactant and biomolecules are prepared and the precipitation of nanocarriers is promoted by addition of sodium carbonate. High encapsulation efficiencies can be obtained with the co-precipitation method.[24]

In the aforementioned approaches, the lack of control of morphology and polymorphism of the carriers is the main drawback. Polymers,[31] polysaccharides[32,33] or even proteins[34] can be used to modify the crystallization pathway of calcium carbonate and allow the control of the morphology and the stabilization of specific polymorphisms. This method is known as polymer-controlled mineralization and results in either nanoparticles[32] or highly porous, micron-sized particles.[34] The wide variety of polymers and polyelectrolytes that can be used enables the synthesis of pH and temperature responsive carriers.[35,36] The incorporation of anti-cancer drugs[35,37] and proteins[33] can be either performed by physical adsorption after mineralization of the carriers[34] or by co-precipitation.[32]

In our work, we demonstrate a bio-inspired strategy for synthesizing pH-responsive submicron-sized carriers based on the combination of complex coacervation and mineralization. Our group first modified a polymer-controlled approach proposed by Huang et al.[38] in order to produce micropatterned parts[39] and now to encapsulate model proteins. The coacervate-directed method (Scheme 6.1) starts with complex coacervation between negatively or positively charged biomolecules and poly(acrylic acid) sodium salt (PAANa). The polymer is used as an additive to modify mineralization, to stabilize amorphous calcium carbonate

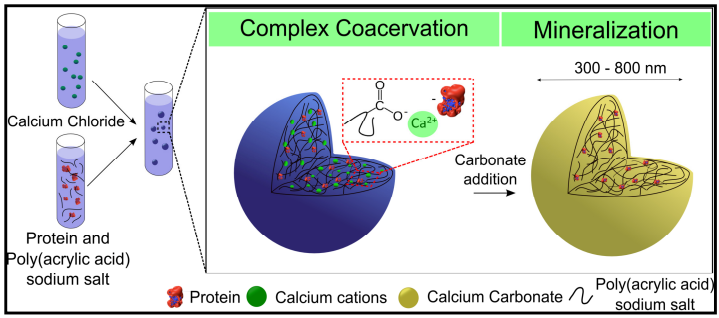


**Scheme 6.1:** Schematic synthesis approach of coacervate-directed $CaCO_3$ microcarriers: complex coacervation between PAANa and the proteins in aqueous solution generates loaded-coacervate droplets, which are subsequently mineralized by the addition of sodium carbonate.

(ACC) and to incorporate the proteins into the coacervate droplets. In order to stop complexation and to stabilize the loaded droplets, sodium carbonate is added to the solution leading to the mineralization of the complex. Since the entire encapsulation process takes place in aqueous solutions, at room temperature and mild pH, the main benefits are the preservation of the bioactivity of the encapsulated biomolecules as well as the ability to easily scale up the system. Therefore, coacervate-directed microcarriers are highly promising for potential use in gene, drug, protein and growth factor delivery.

## 6.2. Experimental section

### 6.2.1. Materials

Calcium chloride ($CaCl_2$, purity ≥ 96%), sodium carbonate ($Na_2CO_3$, purity ≥ 99.5%), poly(acrylic acid) sodium salt (PAANa, Mw = 8000 g/mol, 45 wt% in water), bovine serum albumin (BSA, lyophilized powder, purity ≥ 96%) and lysozyme (LSZ, lyophilized powder, purity ≥ 90%) were purchased from Sigma-Aldrich and used without any further purification. The experiments were performed using double deionized water with a conductivity of 0.04 µS/cm from Synergy (Millipore, Darmstadt, Germany).

### 6.2.2. Synthesis of $CaCO_3$ and incorporation of proteins

Briefly, 40 mL aqueous solution of PAANa and $CaCl_2$ was prepared resulting in a final concentration of polyelectrolyte ranging from 700 to 1900 µg/mL with fixed calcium concentration of 12 mM. The complexation between $Ca^{2+}$ and PAANa takes place immediately after mixing and leads to the phase-separation of liquid-like complex coacervates. These droplets are a highly hydrated $Ca^{2+}$/PAA complexes dispersed in the polymer-poor aqueous solution. After a specific period of time, the complexation time, 12 mM $Na_2CO_3$ was added. Since one of the main components of the coacervate droplets is calcium cations, the addition of carbonate mineralizes the complex. The samples were centrifuged (5000 rpm, 10 minutes) and the obtained precipitate was dried at room temperature for 2 days. The bulk amount of carriers produced per batch is dependent on the solution's volume, which allows easy scale-up of the process.

In order to prepare protein-loaded carriers, the respective biomolecule was dispersed in the aqueous solution prior to the addition of PAANa and $CaCl_2$. The final concentration of proteins ranged from 0.2 to 0.3 mg/mL and all other parameters were kept the same.

### 6.2.3. Release behavior of proteins

The obtained protein-loaded $CaCO_3$ microcarriers were dried in air, weighed (about 20 – 30 mg per batch), and resuspended in 0.54 mL of acetic acid (ph 4.8), PBS buffer (pH 6) or PBS buffer (pH 7.4). The samples were mildly shaken for 200 hours at room temperature. An aliquot of 350 µL was removed at each measurement time-point and replaced with an equal volume of the same buffer. The removed aliquot was centrifuged at 5000 rpm for 15 minutes and the protein concentration was determined by UV-Visible spectroscopy at 280 nm. The absorbance of polyacrylate was evaluated at this wavelength and is negligible. Biomolecule content and loading efficiencies are calculated as follows (equations 5 and 6):

$$Biomolecule\ content = \frac{quantified\ amount\ of\ biomolecules\ (nM)}{total\ weight\ of\ microcarriers\ (mg)} \quad \text{Eq. 5}$$

$$Loading\ effieciency = \frac{quantified\ amount\ of\ biomolecules\ (nM)}{initial\ amount\ of\ biomolecules\ (nM)}\ 100\% \quad \text{Eq . 6}$$

### 6.2.4. Characterization of coacervate droplets and $CaCO_3$ microcarriers

Dynamic light scattering (DLS) as well as zeta-potential measurements were performed on a zetasizer device (Malvern, Nano ZSP). The morphology of the carriers was evaluated by scanning electron microscopy (Zeiss, SUPRA 40), with an acceleration voltage of 15 kV. X-ray diffraction analysis (XRD) was carried out using a JSO-Debyeflex 2002 device, with CuKα radiation (k = 1.542 A). The samples were ground to form a fine powder and scanned from 20° to 50°, 10 seconds per degree. UV-Vis spectroscopy was performed on a Multiskan G0 device (Thermo Scientific) at 280 nm.

## 6.3. Results

### 6.3.1. Influence of complexation time and protein incorporation on the coacervate droplets size

The electrostatic interaction of $Ca^{2+}$ cations with PAANa induces the self-assembly of complex coacervate droplets. These are small complexes with an average size ranging from 200 to 400 nm formed by liquid-liquid phase separation from the initial solution. As mentioned above, this entropy-driven phenomenon is also known as complex coacervation,[40] although the term is largely missing in

more recent literature, where it is sometimes replaced by purely descriptive terms.[41] The main characteristics of the coacervates are the high instability (since it is a metastable phase) as well as the liquid-like behavior. As a result of these characteristics, after nucleation, the coarsening of the droplets happens most likely through diffusion and accumulation of polymer and $Ca^{2+}$.[42] Ostwald ripening does not seem to play a role as a growth mechanism since the polydispersity of the coacervates remains constant over time and the tail of the size distribution curve is located on the large-diameter side (Supporting Figure 6.1, Appendix 10.2).[43] Figure 6.1 depicts the tendency of growth as a function of complexation time as well as the influence of the polyelectrolyte and proteins on the droplets size.

For native coacervates ($Ca^{2+}$/PAANa in the absence of proteins), the initial size is highly dependent on the PAANa concentration. By increasing the polymer concentration, the number of nucleation sites is increased along with a reduction in the particle size. Moreover, the droplets grow at different rates depending on the polymer concentration. For 700 µg/mL of PAANa, coacervates grow steadily within the 14-minute-experiment, while for 1900 µg/mL this growth behavior is no longer noticeable. The growth process is related to the stability of the coacervates in solution. Since the coacervate droplets are electrostatically stabilized, droplets with higher net charges are less susceptible to aggregation and growth. (Supporting Figure 6.2).[44,45] Moreover, it is possible to tailor the size by controlling the polymer concentration; if the concentration is increased from 700 to 1900 µg/mL, the particle size decreases from 800 nm to 300 nm.

BSA-loaded coacervates were prepared with final BSA concentration of 0.2 g/L. The incorporation of BSA slightly decreases the coacervates size compared to unloaded droplets. The rate at which the coacervates grow is not affected by the incorporation of BSA (Figure 6.1).

When lysozyme is incorporated into the droplets, the coacervate size drastically changes (Figure 6.1). The effect of LSZ on the coacervates is thought to be related to the formation of another complex coacervate, comprised of LSZ and PAANa. The electrostatic interaction of LSZ and PAANa is described in previous studies.[46,47] These complexes are larger than $Ca^{2+}$/PAANa, ranging from 800 nm to 1.2 µm depending on the polymer concentration. This can be explained by the increased incorporation of LSZ due to stronger complexation compared to BSA. Furthermore, diffusion-controlled transport is still the predominant growth mechanism and reveals the metastability of the complex.

### 6.3.2. Characterization of mineralized microcarriers

As seen from the DLS results (Figure 6.1), the size of coacervate droplets is highly dependent on the complexation time (tendency to grow over time as a result from the liquid-like behavior) and the polymer concentration. Based on this, it is possible to tailor the size of the final microcarriers by tweaking these two parameters. Since small carriers are desired for drug delivery applications, the complexation time was set to 1 minute and sodium carbonate was added to the solution in order to mineralize the microcarriers. Figure 6.2 summarizes the final size of native, BSA and LSZ-loaded microcarriers measured by DLS. For native and BSA-loaded, increasing the polymer concentration yields smaller carriers. However, for LSZ-loaded carriers this tendency is no longer observed due to the formation of larger LSZ/PAANa coacervates.

The morphology of carriers has shown to affect the cellular uptake of nanoparticles[48] and therefore this facet was assessed by SEM (Figure 6.3). The incorporation of both negatively and positively charged molecules does not seem to influence the spherical geometry of the mineralized microcarriers. In the case of LSZ loading, smaller particles of about 20 nm can be observed adsorbed to the bigger particles. Since mineralization takes place at high supersaturation conditions, these small, unstable particles are formed and adsorb at the surface of the mineralized coacervate droplets.[39] For all samples, the size of the mineralized microcarriers is consistent with the DLS data. In some of the samples, formation of

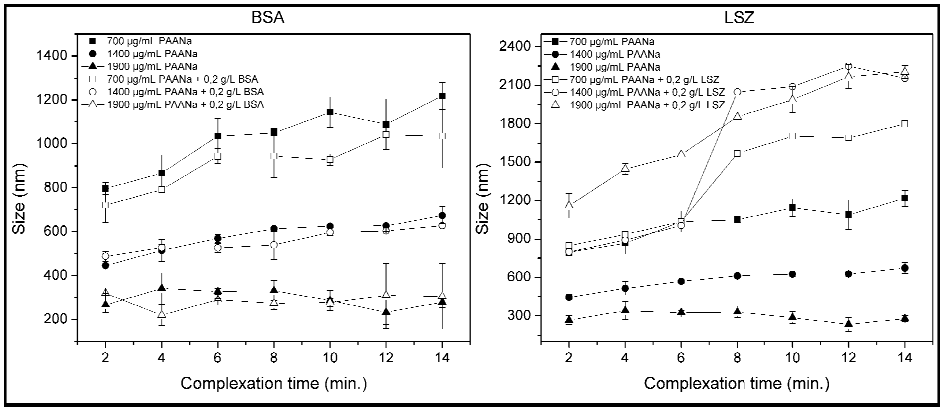


**Figure 6.1:** Dynamic Light Scattering (DLS) overview of the mineralized microcarriers size as a function of PAANa concentration: Native, BSA and LSZ-loaded microcarriers. $[Ca^{2+}]=[CO_3^{2-}]$ was kept constant at 12 mM. Each value is represented as means ± standard deviation of 3 samples.

open capsules could be observed. Note, however, that the intact carriers are not hollow, as was confirmed by STEM analysis (Supporting Figure 6.3).

Zeta potential measurements can be used to assess the adsorption behavior of the molecules onto the surface of the particles. For carriers loaded with LSZ, by increasing the LSZ concentration from 0 to 0.5 g/L, the zeta potential changes from - 35 to -26 mV (Table 6.1). Most likely, positively-charged LSZ is adsorbed on the surface of negatively charged carriers. The zeta potential measured for BSA remains constant at about -35 mV, which means that absorption does not seem to take place, mainly due to electrostatic repulsion between negatively charged BSA and $CaCO_3$.

The amorphous polymorphism of the samples was verified by XRD analysis (Supporting Figure 6.4). Hydrophilic polymers are well known to stabilize the amorphous phase as well as to alter the morphology of the final product.[31] The various effects of LSZ[49] and BSA[34] on the stabilization of polymorphism and morphology of $CaCO_3$ are also reported in the literature.

### 6.3.3. Incorporation of proteins

Yield of carriers, loading efficiency and biomolecule content is detailed in Figure 6.4. For all experiments, the yield of carriers is around 20 mg, even with the incorporation of BSA or LSZ. Moreover, according to the UV measurements, 0.23

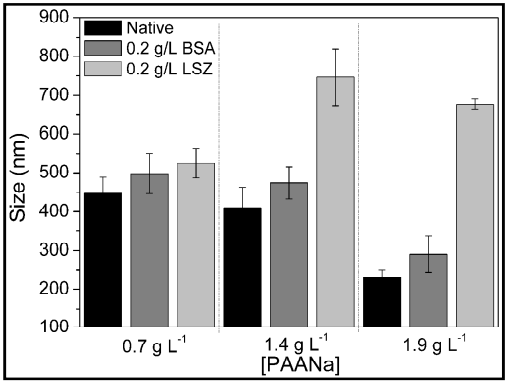


**Figure 6.2:** Dynamic Light Scattering (DLS) overview of the mineralized microcarriers size as a function of PAANa concentration: Native, BSA and LSZ-loaded microcarriers. $[Ca^{2+}]=[CO_3^{2-}]$ was kept constant at 12 mM. Complexation time was set to 1 minute. Each value is represented as means ± standard deviation of 3 samples.

nM of BSA were encapsulated per milligram of $CaCO_3$ carriers, resulting in an efficiency of about 0.2%. The scarce encapsulation of BSA was probably caused by the electrostatic repulsion of PAANa and BSA, since both of them are negatively charged at synthesis pH of 7. However, the LSZ experiment showed that 7 - 8 nM of LSZ were encapsulated per milligram of $CaCO_3$ carriers, which equals an efficiency of 17 – 33 %. Most likely, the electrostatic attraction between PAANa and LSZ is responsible for the better efficiency.

### 6.3.4. Release of proteins from microcarriers

The amount of proteins released from the carriers was cumulatively plotted in figure 6.5. The release profile is highly pH dependent, which suggests that the main mechanism of release is the dissolution of the carriers.

At neutral pH, the complete BSA content is released within 50 hours (Figure 6.5). If the experiments are performed at pH 4.8, the same amount of protein is released within a tenth of that time, 5 hours. Experiments that took place at pH 6 showed a similar release behavior as for pH 7. In general, BSA-loaded carriers show a rapid release curve at all evaluated pHs when compared to LSZ. Moreover,

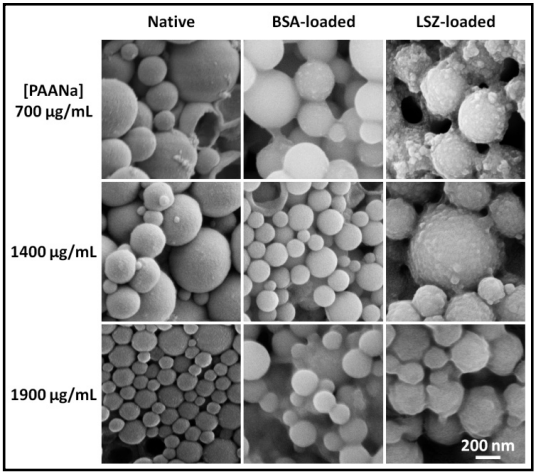


**Figure 6.3:** SEM micrographs of native, BSA and LSZ-loaded microcarriers as a function of PAANa concentration (700, 1400 and 1900 µg/mL). $[Ca^{2+}]=[CO_3^{2-}]$ was kept constant at 12 mM. Complexation time was set to 1 minute.

**Table 6.1.** Zeta potential (mV) of microcarriers as a function of protein concentration. Measurements were performed at pH 9 and 1400 g/L of PAANa. Each value is represented as means ± standard deviation of 3 samples.

| Protein concentration | 0 g/L | 0.2 g/L | 0.5 g/L |
|---|---|---|---|
| BSA | -35.68 ± 2.41 | -31.14 ± 4.50 | -37.09 ± 6.92 |
| LSZ | -35.68 ± 2.41 | -28.24 ± 3.21 | -26.14 ± 4.01 |

the release of BSA was completed before full dissociation of the carriers, which leads to two conclusions, (a) BSA is physically adsorbed to the surface of the carriers and therefore the release is desorption-dependent or (b) the molecules are encapsulated close to the surface of the carrier, which leads to complete release without full dissociation of the particles. By analyzing the zeta potential measurements, the first hypothesis is unlikely, since the zeta potential remains constant with varying BSA concentrations (Table 6.1).

Regarding LSZ, the release profile shows sustained release over time with a notable absence of a burst release. At pH 4.8, LSZ was fully released within 140 hours while at neutral pH the release reaches a plateau after 80 hours of about 30% of release. At pH 6, the release behavior was slightly faster than at pH 7. Both at pH 6 and 7.4, the release was slow and incomplete. The cationic nature of this protein (pKa = 11.35) gives rise to electrostatic interaction with the negatively charged carriers preventing complete release. Another possible explanation lies in the electrostatic nature of the complex LSZ/PAANa. If the pH is decreased, the net charge of PAANa reduced which weakens the complex and allows a complete release.

Burst release of biomolecules from inorganic porous carriers have been reported elsewhere.[50] In the case of calcium carbonate, it is mostly associated with the polymorph stability.[22] Since the carriers are amorphous, the most unstable polymorph of $CaCO_3$, burst release could be expected. However, due to the introduction of PAANa, which stabilizes the carrier, the initial burst release can be avoided.

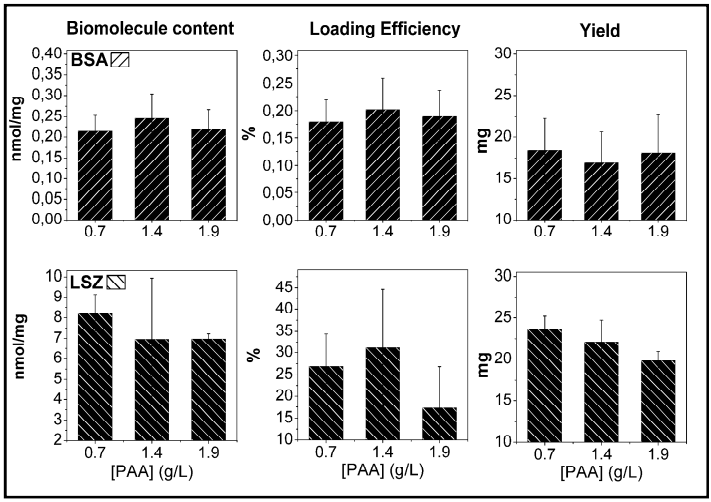


**Figure 6.4:** Yield of carriers, loading efficiency and biomolecule content for BSA and LSZ loaded carriers. Each value is represented as means ± standard deviation of 3 samples.

### 6.3.5. Proposed mechanism for protein encapsulation and release behavior

The incorporation of proteins is based on the electrostatic interaction between PAANa and the respective molecule. In the case of BSA (Scheme 6.2a), calcium plays two roles: (1) it favors the formation of complex coacervate droplets comprised of highly hydrated $Ca^{2+}$/PAANa and (2) it binds to both the carboxylate groups and the negative sites of BSA, forming the complex PAANa/$Ca^{2+}$/BSA,[51] which is responsible for encapsulation. The $Ca^{2+}$-mediated complex is only moderately effective in incorporating BSA (0.21 nM per mg of sample) and therefore results in low encapsulation capacities (0.02%).

By contrast, in the case of LSZ, two complex coacervation phenomena take place simultaneously: (1) complex coacervation of $Ca^{2+}$/PAANa and (2) complex coacervation of LSZ/PAANa, which is responsible for encapsulation (scheme 6.2b). The competitive effect between the complexes leads to the formation of larger carriers with larger size and broader size distribution. Due to high electrostatic interaction between the polyelectrolyte/protein, higher encapsulation efficiencies (around 25%) are obtained.

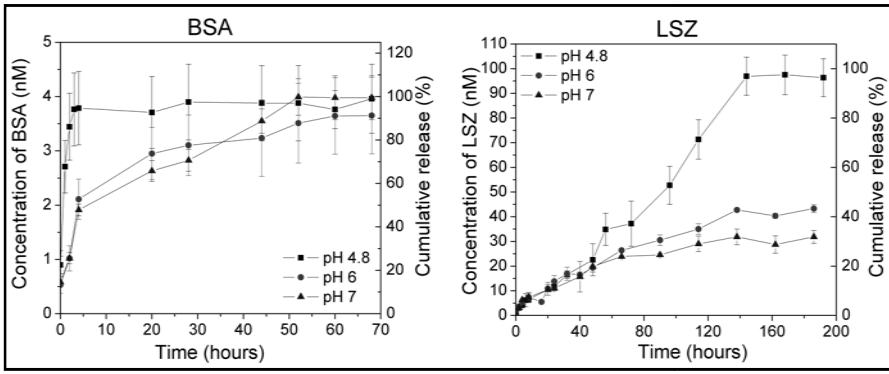


**Figure 6.5:** Release profile of BSA and LSZ from microcarriers in acetic acid pH 4.8, PBS buffer pH 6 and 7.4. Each value is represented as means ± standard deviation of 3 samples.

After formation of the coacervates, $Na_2CO_3$ is added in order to stabilize the droplets by forming fully mineralized amorphous $CaCO_3$ particles. This material exhibits a good solubility in acid environments allowing the triggered release of proteins by adjusting the pH of the solution (Figure 6.5). BSA molecules are encapsulated close to the surface of the carrier and are rapidly and completely released after 50 hours. The release of LSZ is slow and incomplete due to electrostatic interaction between the protein and the negatively charged carriers.

## 6.4. Conclusions

In summary, the coacervate-directed mineralization approach allows the synthesis of pH-responsive carriers loaded with both negatively charged BSA and

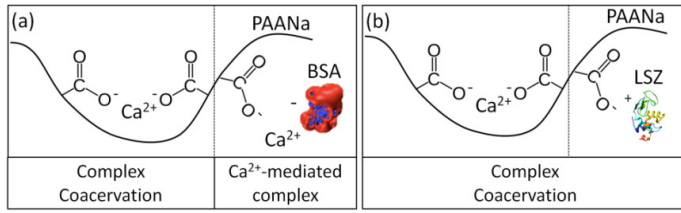


**Scheme 6.2:** Proposed mechanism for encapsulation of (a) BSA and (b) LSZ into the coacervate droplets.

positively charged LSZ. The synthesis starts by complexating PAANa and the respective protein within coacervate droplets, whose size can be tailored by the polymer concentration and the complexation time. In order to stabilize the protein-loaded coacervate droplets and functionalize them with pH-responsive behavior, the complexes were mineralized via the addition of carbonate. The fully mineralized $CaCO_3$ microspheres had a diameter between 300 and 800 nm, exhibited spherical morphology and were loaded with BSA and LSZ at 0.2 nM and 8 nM per milligram of $CaCO_3$, respectively. As expected, the release behavior of the proteins was triggered by changes in pH. BSA molecules were rapidly and completely released after 50 hours while the release of LSZ is slow and incomplete due to electrostatic interaction between the protein and the negatively charged carriers. Based on these features, we think that the coacervate-directed method presents a cost-effective, easy to scale-up way to synthesize tailorable submicron-sized, pH-responsive $CaCO_3$ carriers, which can be potentially used in gene, drug and growth factor delivery.

## 6.5. References

This chapter was adapted from with permission from Lauth, V.; Maas, M.; Rezwan, K. Coacervate-Directed Synthesis of $CaCO_3$ Microcarriers for pH-Responsive Delivery of Biomolecules. J. Mater. Chem. B 2014, 2, 7725–7731. Copyright 2014 Royal Society of Chemistry.

The article is mainly based on the work of the first author and the author of this thesis, Victor Rafael Lauth. The precise contributions of each author are listed below.

| Author | Contribution |
|---|---|
| Lauth, V. | Conceptualization of the work, design and implementation of experiments, data collection, analysis and interpretation, principle writing of the manuscript and revision of the article |
| Maas, M. | Conceptualization of the work, data analysis, writing and revision of the manuscript. |
| Rezwan, K. | Gave conceptual advices and input, critical assessment of all experiments and revision of the manuscript. |

1. S. Ganta, H. Devalapally, A. Shahiwala and M. Amiji, *J. Control. Release*, 2008, **126**, 187–204.

2. D. Peer, J. M. Karp, S. Hong, O. C. Farokhzad, R. Margalit and R. Langer, *Nat. Nanotechnol.*, 2007, **2**, 751–760.

3. M. P. Monopoli, C. Åberg, A. Salvati and K. A. Dawson, *Nat. Nanotechnol.*, 2012, **7**, 779–786.

4. S. Mura, J. Nicolas and P. Couvreur, *Nat. Mater.*, 2013, **12**, 991–1003.

5. J. Nicolas, S. Mura, D. Brambilla, N. Mackiewicz and P. Couvreur, *Chem. Soc. Rev.*, 2013, **42**, 1147–1235.

6. B. de Jong and H. R. Kruypz, *Proc. K. Ned. Akad. Wet.*, 1929, **32**, 849–856.

7. R. Arshady, *Polym. Eng. Sci.*, 1990, **30**, 905–914.

8. B. Wang, B. Adhikari and C. J. Barrow, *Food Chem.*, 2014, **158**, 358–365.

9. I. M. Martins, S. N. Rodrigues and F. Barreiro, *J. Microencapsul.*, 2009, **26**, 667–675.

10. H. K. Awada, N. R. Johnson and Y. Wang, *Macromol. Biosci.*, 2014, **14**, 679–686.

11. K. . Leong, H.-Q. Mao, V. . Truong-Le, K. Roy, S. . Walsh and J. . August, *J. Control. Release*, 1998, **53**, 183–193.

12. Y. Yuan, J. Tan, Y. Wang, C. Qian and M. Zhang, *Acta Biochim Biophys Sin*, 2009, **41**, 515–526.

13. N. Ray, T. Ambe and Y. Wang, *Acta Biomater.*, 2014, **10**, 40–46.

14. S. Mann, *Acc. Chem. Res.*, 2012, **45**, 2131–2141.

15. C. Sanchez and D. Renard, *Int. J. Pharm.*, 2002, **242**, 319–324.

16. C. L. Cooper, P. L. Dubin, A. B. Kayitmazer and S. Turksen, *Curr. Opin. Colloid Interface Sci.*, 2005, **10**, 52–78.

17. A. J. Amali, S. Singh, N. Rangaraj, D. Patra and R. K. Rana, *Chem. Commun.*, 2012, **48**, 856–858.

18. R. Kurapati and A. M. Raichur, *J. Mater. Chem. B*, 2013, **1**, 3175.

19. D. V Volodkin, N. I. Larionova and G. B. Sukhorukov, *Biomacromolecules*, 2004, **5**, 1962–1972.

20. A. I. Petrov, D. V Volodkin and G. B. Sukhorukov, *Biotechnol. Prog.*, 2005, **21**, 918–25.

21. G. B. Sukhorukov, D. V. Volodkin, A. M. Gunther, A. I. Petrov, D. B. Shenoy and H. Mohwald, *J. Mater. Chem.*, 2004, **14**, 2073.

22. U. Maver, M. Bele and J. Jamnik, *Mater. Res. Bull.*, 2013, **48**, 137–145.

23. Y. Ueno, H. Futagawa, Y. Takagi, a Ueno and Y. Mizushima, *J. Control. Release*, 2005, **103**, 93–8.

24. C.-Q. Wang, J.-L. Wu, R.-X. Zhuo and S.-X. Cheng, *Mol. Biosyst.*, 2014, **10**, 672–8.

25. S. Chen, D. Zhao, F. Li, R.-X. Zhuo and S.-X. Cheng, *RSC Adv.*, 2012, **2**, 1820–1826.

26. T. Borodina, E. Markvicheva, S. Kunizhev, H. Möhwald, G. B. Sukhorukov and O. Kreft, *Macromol. Rapid Commun.*, 2007, **28**, 1894–1899.

27. S. De Koker, B. G. De Geest, S. K. Singh, R. De Rycke, T. Naessens, Y. Van Kooyk, J. Demeester, S. C. De Smedt and J. Grooten, *Angew. Chemie - Int. Ed.*, 2009, **48**, 8485–8489.

28. K. Qian, T. Shi, T. Tang, S. Zhang, X. Liu and Y. Cao, *Microchim. Acta*, 2010, **173**, 51–57.

29. M. Fujiwara, K. Shiokawa, K. Morigaki, Y. Zhu and Y. Nakahara, *Chem. Eng. J.*, 2008, **137**, 14–22.

30. X. He, T. Liu, Y. Chen, D. Cheng, X. Li, Y. Xiao and Y. Feng, *Cancer Gene Ther.*, 2008, **15**, 193–202.

31. V. B. A. De Meijere, K. N. H. H. Kessler, S. V. L. S. L. Schreiber, J. T. B. M. Trost and H. Yamamoto, *Biomineralization II*, Springer Berlin Heidelberg, 2007, vol. 271.

32. D. Zhao, R.-X. Zhuo and S.-X. Cheng, *Mol. Biosyst.*, 2012, **8**, 753–9.

33. Z. Lu, J. Zhang, Y. Ma, S. Song and W. Gu, *Mater. Sci. Eng. C*, 2012, **32**, 1982–1987.

34. N. Qiu, H. Yin, B. Ji, N. Klauke, A. Glidle, Y. Zhang, H. Song, L. Cai, L. Ma, G. Wang, L. Chen and W. Wang, *Mater. Sci. Eng. C*, 2012, **32**, 2634–2640.

35. C. Du, J. Shi, J. Shi, L. Zhang and S. Cao, *Mater. Sci. Eng. C*, 2013, **33**, 3745–3752.

36. J. Shi, W. Qi, C. Du and S. Cao, *J. Appl. Polym. ...*, 2013, 577–584.

37. J. Shi, J. Shi, D. Feng, P. Yue and S. Cao, *Polym. Bull.*, 2014, **71**, 1857–1873.

38. S.-C. C. Huang, K. Naka and Y. Chujo, *Langmuir*, 2007, **23**, 12086–12095.

39. P. Kaempfe, V. R. Lauth, T. Halfer, L. Treccani, M. Maas and K. Rezwan, *J. Am. Ceram. Soc.*, 2013, **96**, 736–742.

40. C. G. De Kruif, F. Weinbreck and R. De Vries, *Curr. Opin. Colloid Interface Sci.*, 2004, **9**, 340–349.

41. B. Cantaert, Y. Kim, H. Ludwig, F. Nudelman, N. A. J. M. Sommerdijk and F. C. Meldrum, *Adv. Funct. Mater.*, 2012, **22**, 907–915.

42. C. Sanchez, G. Mekhloufi and D. Renard, *J. Colloid Interface Sci.*, 2006, **299**, 867–873.

43. C. Sanchez, G. Mekhloufi, C. Schmitt, D. Renard, P. Robert, C. Lehr, A. Lamprecht and J. Hardy, *Langmuir*, 2002, **18**, 10323–10333.

44. D. Romanini, M. Braia, R. Giatte, W. Loh and G. Pic, *J. Chromatogr. b*, 2007, **857**, 25–31.

45. A. Ghimire, R. M. Kasi and C. V Kumar, *J. Phys. Chem. B*, 2014, **118**, 5026–5033.

46. H. Herd, N. Daum, A. T. Jones, H. Huwer, H. Ghandehari and C. Lehr, *ACS Nano*, 2013, **7**, 1961–1973.

47. X. Wang, H. Sun, Y. Xia, C. Chen, H. Xu, H. Shan and J. R. Lu, *J. Colloid Interface Sci.*, 2009, **332**, 96–103.

48. C. Wang, C. He, Z. Tong, X. Liu, B. Ren and F. Zeng, *Int. J. Pharm.*, 2006, **308**, 160–167.

49. M. Karahan, Z. Mustafaeva and C. Ozeroğlu, *Protein J.*, 2010, **29**, 336–42.

# 7. Self-assembly and shape control of hybrid nanocarriers based on calcium carbonate and carbon nanodots

## 7.1. Introduction

*Abstract: We describe a platform for the synthesis of functional hybrid nanoparticles in the submicrometer range with tailorable anisotropic morphology. Fluorescent carbon dots (CDs) and poly(acrylic acid) (PAA) are used to modify the crystallization and assembly of calcium carbonate ($CaCO_3$). Carboxylic groups on CDs sequester calcium ions and serve as templates for $CaCO_3$ precipitation when carbonate is added. This creates primary $CaCO_3$ nanoparticles, 7 nm in diameter, which self-assemble into spheres or rods depending on the PAA concentration. At increasing polymer concentration, oriented assembly becomes more prevalent yielding rod-like particles. The hybrid particles show colloidal stability in cell medium, absence of cytotoxicity as well as a loading efficiency of around 30% for Rhodamine B with pH-controlled release. Given the morphological control, simplicity of synthesis and efficient loading capabilities the CD-$CaCO_3$ system could serve as a novel platform for advanced drug carrier systems.*

In the last years, nanotechnology has quickly established its role as a catalyst for rapid advances in medicine.[1] Both diagnostics and treatment of several diseases, including but not limited to cancer, have been facilitated by the incorporation of imaging agents and active pharmaceutical ingredients in one multifunctional carrier.[2,3] A large number of drug delivery systems (DDS) developed over the past 5 decades addressed the limited cellular uptake by improving carrier-cellular interactions.[4] Recent DDS approaches for improving biological interactions focus either on grafting an active-targeting moiety onto the carrier surface to maximize specific uptake[5] or on tailoring carrier properties, such as geometry, to hinder macrophage engulfment[6] and improving long-term circulation.[7]

Besides the vast and rapidly advancing field of nanomedicine targeted to treat cancer, significant effort has also been put forth in the field of pulmonary delivery. In fact, pulmonary diseases are among global health hazards in terms of mortality[8] and therefore, the application of nanomedicine technology in diagnosis, treatment and prevention is of high importance. Due to the complex anatomy and physiology of the lungs, the design of novel pulmonary delivery systems takes into account

aerodynamic properties of the carriers as well as the innate immune defense mechanisms. Since the engulfment of anisotropic particles by macrophages is orientation-dependent, anisotropic particles can avoid rapid macrophage clearance.[9] Moreover, the anisotropic geometry has shown to allow better lung penetration and accumulation, since anisotropic particles can align with the air flow.[7] Given this, aspherical carriers find high potential in the treatment of pulmonary diseases, such as related to microbial infections.

Nanoparticle size has long been studied as a key parameter for achieving efficient drug delivery by exploiting the enhanced permeability and retention effect (EPR).[10,11] Recently, carrier morphology has emerged as an equally important parameter.[12,13] Early reports described the enhancement of tissue-specific targeting by using non-spherical particles.[14] However, due to difficulties in synthesis, a platform that allows geometrical control of biocompatible carriers in bulk quantities is of high interest. For such purposes, calcium carbonate can be a great option, since it is biocompatible and most importantly, some mechanisms involved in geometrical control have been studied in great detail over the past 25 years.[15]

The crystallization of calcium carbonate can be controlled by the addition of soluble macromolecules, acidic proteins and cations like $Mg^{2+}$.[16,17] In biomineralization, the presence of these additives allows living organisms to synthesize hierarchical minerals and composite materials with intricate morphologies and outstanding mechanical properties. The understanding of principals involved during biomineral synthesis has served as a great source of inspiration for producing advanced synthetic materials.[18]

Additives have been shown to play different roles in mineralization:[19] (i) antiscalants hinder mineralization by disturbing nucleation, (ii) growth initiators induce local supersaturation via ion complexation, (iii) habit modifiers inhibit crystal growth by selective adsorption and (iv) poly-anions are able to stabilize amorphous, highly hydrated phases. Acidic polymers, such as poly(acrylic acid),[20] poly(aspartate),[19,21,22] or dendrimers[23,24] have been shown to play multiple roles at once. Under kinetic controlled mineralization, the crystallization pathway of $CaCO_3$ usually follows multiple steps, starting with formation of primary nanoparticles which then can self-assemble to form the final crystal. This controlled self-assembly of primary particles is known as mesoscale assembly.[25,26] Polymers can adsorb onto specific crystallographic growth planes of primary nanoparticles, affecting both crystal growth and the assembly process.[26] As a result of nanoparticle-polymer interactions, the assembly can take place in a mutually oriented fashion forming higher-order superstructures.[26] The primary nanoparticles that form the superstructure can either grow to form one single crystal or remain at

the nanoscale, depending on the binding affinity between nanoparticles and macromolecules. If oriented assembly takes place with stable crystallites, i.e. particles that do not fuse together, the resulting superstructures are often referred to as mesocrystals.[27]

Carbon nanomaterials can also be used to modify the crystallization of calcium carbonate due to their surface chemistry. For example, carboxyl-functionalized carbon nanotubes (CNTs) can serve as nucleation sites for calcium carbonate, which grows around the CNTs forming spherical vaterite crystals.[28] Graphene and graphene oxide have also been used as templates for controlling the nucleation and growth of $CaCO_3$ crystals for structural materials[29] as well as for the synthesis of bioactive hydroxyapatite bone replacement materials.[30,31] Carbon dots have been reported to influence $CaCO_3$ precipitation as well. They serve as templates for the nucleation of primary hybrid nanoparticles which then self-assemble into spherical sub-micrometer structures.[32]

Carbon dots are especially interesting for biological applications due to their fluorescent properties and very small sizes, under 10 nm. This material usually has a relatively low quantum yield, less than 50% in comparison to the conventional quantum dots.[33] However, surface passivation additives can be incorporated to improve the quantum yield of carbon dots,[34] e.g. poly(ethylenimine) (PEI) or its monomer. The increase in photoluminescence is attributed to passivated defects on the carbon particle surface which act as excitation energy traps.[35] Due to the various surface functional groups, including hydroxyl, carbonyl, carboxyl and amine groups, CDs can form complexes with cations such as $Fe^{3+}$ and $Zn^{2+}$ allowing application as ionic-sensors.[36] Moreover, CDs offer good biocompatibility and low cytotoxicity[37] and therefore have a great potential for biomedical applications, such as bioimaging and biosensors.[34,38]

Here, the fundamentals on the $CaCO_3$ crystal growth were applied for designing drug carriers with two different morphologies: spheres and rods. The developed platform allows control of nanocomposite morphology while maintaining sizes under 500 nm, colloidal stability in cell medium, encapsulation of positively-charged Rhodamine B by electrostatic interaction and pH-triggered release in acid due to carrier dissolution. Such a system can be potentially of interest for the treatment of pulmonary diseases.

## 7.2. Experimental section

### 7.2.1. Materials

Calcium chloride ($CaCl_2$, purity ≥ 96%), sodium carbonate ($Na_2CO_3$, purity ≥ 99.5%), poly(acrylic acid) sodium salt (PAANa, Mw 8000 g/mol , 45 wt% in water), poly(ethylenimine) branched (PEI, Mw 25000 g/mol) and Rhodamine B (479.02 g/mol, purity ≥ 95%) were purchased from Sigma-Aldrich and citric acid ($C_6H_8O_7$, purity ≥ 99.5%) was purchased from Carl Roth GmbH. All chemical were used without further purification. The experiments were performed using double deionized water with a conductivity of 0.04 μS $cm^{-1}$ from Synergy (Millipore, Darmstadt, Germany). Phosphate buffered saline (PBS) was prepared as follows: 129 mM NaCl, 2.5 mM KCl, 7 mM $Na_2HPO_4 \cdot 7\ H_2O$ and 1.3 mM $KH_2PO_4$. The pH was adjusted to 7.4. Hanks' Balanced Salt Solution (HBSS) was prepared in accordance to supporting information 7.1 (Appendix 10.3). RPMI-1640 cell culture medium (Gibco, Life Technologies) was used without further supplements.

### 7.2.2. Synthesis of Carbon dots with different degree of carboxylation (CDs)

Carbon dots are synthesized by an in-complete carbonization reaction of citric acid in water, as previously described.[39] Briefly, 1 g of citric acid is dissolved in 10 mL of Millipore water and heated to 130 °C. The samples were treated for 2 or 2.5 hours. After the defined time, most of the water evaporated and the sample resembles an orange-yellow gel. After cooling to room temperature, the gel is dissolved in 50 mL of 10 g/L NaOH and centrifuged (6000 rpm for 30min) to remove any aggregates. The supernatant is kept and the pH is set to 10. Samples treated for 2h had a yield of 0.022 ± 0.003 g/L and the carboxylation degree $[CD]_{COOH}$ was 2.3 mol/g, while sample treated for 2.5h had a yield of 0.005 ± 0.001 g/L and 0.5 mol/g of $[CD]_{COOH}$. For calculation see Supporting Information 7.2.

### 7.2.3. Carbon-dots-mediated precipitation of $CaCO_3$ by Poly(acrylic acid) (PAA-CD-$CaCO_3$) and Poly(ethylenimine) (PEI-CD-$CaCO_3$)

The synthesis of $CaCO_3$ nanocomposites is performed by a one-pot approach. The synthesis starts with 6 mL aqueous solution of PAANa (final concentration of 0, 0.15, 0.3, 0.5 and 0.7 g/L) mixed with CDs (final concentration of 0.013 g/L). After stirring the suspension for 10 minutes, an aqueous solution of $CaCl_2$ is added to reach a final concentration of 32 mM. Subsequently, an aqueous solution of $Na_2CO_3$ is rapidly added keeping the ratio $[Ca^{2+}]=[CO_3^{2-}]$ constant. Finally, the suspension is stirred for 48 hours to allow complete the mineralization. The

precipitated hybrid nanoparticles were centrifuged (5000 rpm, 30 min) and the supernatant is removed to extract free carbon dots. The pellet is redispersed in 10 mL of Millipore water.

To evaluate the influence of a cationic polymer on the assembly process, a second experiment was performed in which along with PAANa, PEI was added to the CDs solution and precipitation procedure followed as previously described. The polymers final concentrations are 0, 0.3 and 0.7 g/L, keeping the weight ratio PAA:PEI 1:1.

### 7.2.4. Rhodamine B encapsulation and release from CD-$CaCO_3$

Rhodamine B, a low molecular weight fluorescent dye, was used as a hydrophilic model drug due to its hydrophilicity and positive charge. For RhB encapsulation, the dye is dissolved in the solution containing PAANa and CDs with final concentration of 12 μM and precipitation procedure followed as previously described.

The release profile was determined by dispersing 10 mg of rod-shaped (0.7 g/L PAA-CD-$CaCO_3$) in 1 mL of 0.3 M Citric acid – Sodium citrate buffer at pH 4.8 or PBS buffer at pH 7.4. The dispersion was kept under gentle stirring in the dark. At specific time points, 300 μL were drawn from the solution, centrifuged to remove any particle in solution and the fluorescence was measured at 575 nm (excited at 500 nm) in a 96-well plate. No appreciable reduction on the fluorescence intensity was observed over the course of the experiment (Supporting Information 7.3).

### 7.2.5. Stability of CD-$CaCO_3$ in various physiological media

PAA-CD-$CaCO_3$ nanocomposites were centrifuged at 6000 rpm for 10 minutes, the supernatant was removed and the pellet redispersed in different media: Millipore water, Hanks Balanced Salt Solution (HBSS) and RPMI and RPMI supplemented with 10% (v/v) fetal bovine serum (FBS). The size and zeta potential were determined by a Zetasizer after 4 hours of incubation (Nano ZS, Malvern Instruments). The data is given as mean ± standard deviation (SD) based on three independent measurements.

### 7.2.6. Toxicity Profile

To assess relative toxicity of the nanoparticles, cell viability at different concentrations was evaluated by means of membrane integrity via LDH release and metabolic activity via mitochondrial enzymes (MTT). PAA-CD-$CaCO_3$ nanocomposites were centrifuged and redispersed in HBSS pH 7.4 at different concentrations. Cells A549 were cultured in RPMI supplemented with 10% FCS.

One day prior to experiments, the cells were detached and seeded in a 24-well plate at a density of 1 x $10^4$ cells per well. In the following day, the suspensions were added and incubated for 4 h. In addition, for MTT assay, cells grown in culture medium were set as high control (100% cell viability) and others incubated with Triton X-100 (2%, w/v) were used as low control (0% cell viability). For the LDH assay, the cytotoxicity was calculated relative to Triton X-100 as high control and cells in culture medium as low control. Samples were measured in triplicates and evaluated as mean and standard deviations (SD).

### 7.2.7. Characterization

Potentiometric titration was performed with a pH electrode PHC3081 connected to Titralab Tim 840 automated titrator (Radiometer Analytical SAS, France) operating at an addition speed of 0.2 L/min. All triplicate measurements were carried out under 2 L/min $N_2$ at room temperature. Each sample is comprised of 5 mL CD dispersion and 15 mL water. The pH was adjusted to 4.2 by the addition of 800 µL 1M HCl. Particle morphologies were visualized by transmission electron microscopy (TEM, Oxford Instruments - JEOL JEM 2011 and Zeiss - EM 900) and scanning electron microscopy (SEM, Zeiss - Supra 40). Before SEM, the dispersion was centrifuged and the supernatant was removed. Afterwards, a droplet of dispersion was placed on a silicon wafer and dried at 70°C for 2 h. Before TEM, the dispersion was diluted 1:5 and a droplet of dispersion was placed on a copper grid with Formvar film and dried in air. The samples did not require staining. X-ray diffraction (XRD) was carried out using a Seifert XRD 3003 device (General Electric, Germany), with CuKa radiation (k = 1.542 Å). The samples were ground to form a fine powder and scanned for 2 s per degree from 20° to 70°. The specific surface area (SBET) of the samples was determined by nitrogen adsorption (Belsorp-Mini, Bel Japan), using the BET-method. Quantum yield was measured in an Infinite 200 PRO device (Tecan, Switzerland).

## 7.3. Results

The synthesis of $CaCO_3$ nanocomposites is performed by a one-pot approach. It begins by preparing carbon nanodots via an incomplete carbonization reaction of citric acid in water.[39] The reaction takes place in absence of passivation additives and results in low quantum yield CDs. Using DAPI as reference, the quantum yield measured was 0.3% (Supporting Information 7.4). The surface chemistry of CDs can be controlled by varying the duration of the carbonization reaction. Samples heat-treated for 2.5 hours showed a darker color and a lower carboxylation degree of 0.5 mol/g, while samples treated for 2 hours were lighter in color with higher carboxylation degree of 2.3 mol/g (Figure 7.1a, insets. For calculations see

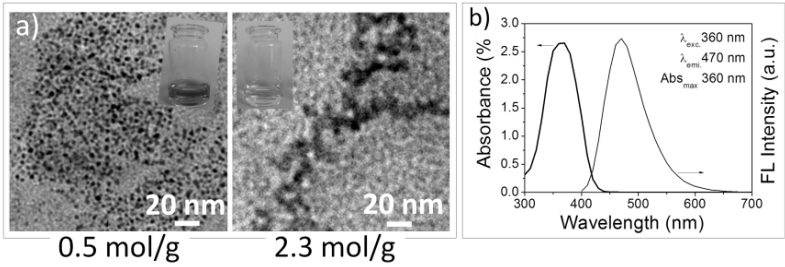


**Figure 7.1:** a) TEM micrographs of carbon dots with varying degrees of carboxylation ($[CD]_{COOH}$ 0.5 and 2.3 mol/g). Inset shows the color of each dispersion at pH 10. b) Maximum absorption at 360 nm and emission at 470 nm of sample $[CD]_{COOH}$ 2.3. Sample $[CD]_{COOH}$ 0.5 had similar fluorescence and absorbance spectra.

Supporting Information 7.2). Moreover, TEM micrographs revealed a difference in size when comparing both samples. For CD with 2.3 mol/g, the size is around 2.10 ± 0.15 nm while it is 15.72 ± 2.95 nm for a carboxylation degree of 0.5 mol/g. Despite the difference in particle size, maximum absorption at 360 nm was observed for both samples. If excited at 360 nm, the fluorescent maximum is observed at 470 nm situated in the blue color space (Figure 7.1b).

The reaction proceeds with the addition of PAA at low concentrations to the carbon nanodot dispersion, followed by sequential addition of calcium chloride and sodium carbonate. This results in the immediate formation of primary nanoparticles as shown in Figure 7.2a. According to SEM and TEM micrographs, these nanoparticles are anisotropic with an average size of 7.4 ± 2.1 nm. The TEM micrographs suggest that the crystallites show a plate-like geometry, similar to the anisotropic carbon dots. Moreover, XRD reveals the crystalline nature of the primary nanoparticles, showing calcite polymorphism (figure 7.2b). After stirring for 4 hours, it is observed that the primary nanoparticles self-assemble into micrometer structures, as shown on Figure 7.2c. The assembly of submicrometer particle is complete after 48 hours of stirring (figure 7.2d).

As carboxylated additives are known to influence $CaCO_3$ crystallization, the effect of PAA concentration (0, 0.15, 0.3, 0.5 and 0.7 g/L) as well as the carboxylation degree of CD (0.5 and 2.3 mol/g) was assessed with regards to final particle geometry and an overview is shown in Figure 7.3. At a low carboxylation degree, large calcite crystals immediately precipitated from the solution, independent of the PAA concentration (figure 7.3, bottom). Here, the carboxyl concentration of carbon dots and PAA is not sufficient to avoid precipitation and

the crystallization follows the classical pathway. Below 0.3 g/L of PAA, aspherical crystals with large particle size (5 - 7 µm) precipitated. At 0.7 g/L, the formed structures show rod-like morphology and particle size of around 1 µm.

At high carboxylation degree, the final morphology can be controlled by varying the concentration of the polymer. In the absence of the polymeric additive, calcite crystals immediately precipitated. The crystals look similar to the ones formed at low carboxylation degree and can be explained by the low concentration of crystallization inhibiting PAA. In this case, the carboxyl groups on the surface of the CDs alone are not sufficient for avoiding direct precipitation. However, by adding even small concentrations (0.15 g/L) of PAA, the formation of large crystals is prevented and sub-micrometer spheres are formed. At 0.3 g/L a combination of spheres and rods are formed (31/69% respectively). At 0.7 g/L PAA, all particles show a rod-like shape. Above this concentration, only very small nanoparticles (under 90 nm) are formed. This can be assigned to further polymer stabilization, which completely prevents aggregation (Supporting information 7.5). The influence of PAA molecular weight was evaluated by mineralizing the samples with 15k and 100k g/mol PAA at 0.15 and 0.7 g/L. The samples were mineralized with high carboxylation degree carbon dots and the results show (Supporting information 7.6) that there are no significant changes when increasing the M.W. to 15k g/mol. At 100k g/mol, both spheres and rods are formed at 0.1 g/L PAA. This highlights the ability to control the geometry of the carriers in a wide

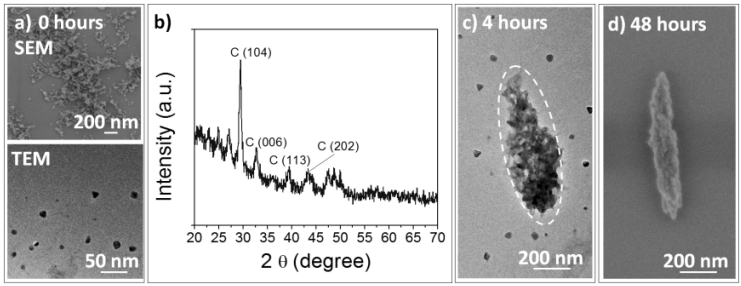


**Figure 7.2:** Precipitation of PAA-CD-$CaCO_3$ at different stages: (a) SEM and TEM micrographs immediately after carbonate addition. Particle size measured by TEM 7.4 ± 2.1 nm (n =30 ± deviation). (b) XRD pattern immediately after carbonate addition. (c) After 4 h, the nanoparticles self-assemble to form the rod microstructure (dashed curve delineates the final structure). (d) Assembled rod-like composite nanoparticles after 48 h. Polymer concentration is 0.7 g/L, and CD carboxylic degree is 2.3 mol/g. Sample $[CD]_{COOH}$ 0.5 had similar fluorescence and absorbance spectra.

range of molecular weights. However, at extreme long chain lengths, the morphology is no longer controlled by PAA.

The spheres and rod like carriers were characterized by means of zeta-potential and BET. Dispersed in water, the zeta-potential at pH 7.4 is around -38.9 ± 5.2 for 0.7 g/L and -36.7 ± 7.0 mV for 0.3 g/L PAA. The difference in zeta potential is due to the difference in polymer concentration. For samples prepared with 0.7 g/L PAA, the median pore diameter calculated by Nitrogen adsorption-desorption was 37 nm; the surface area 27 $m^2/g$ and total pore volume 0.24 $cm^3/g$ (Supporting information 7.7). While for 0.3 g/L PAA, median pore diameter was 23 nm, the surface area of 36 $m^2/g$ and total pore volume of 0.21 $cm^3/g$. Pore size distribution calculated by BJH shows monomodal (about 6 nm) distribution of pores for both geometries. This pore size can be attributed to the space in between assembled nanoparticles, as revealed by TEM (figure 7.2c). Analysis of the XRD pattern of the final particles (Supporting information 7.8) showed that the most stable polymorph, calcite, is still present after 48 h of precipitation.

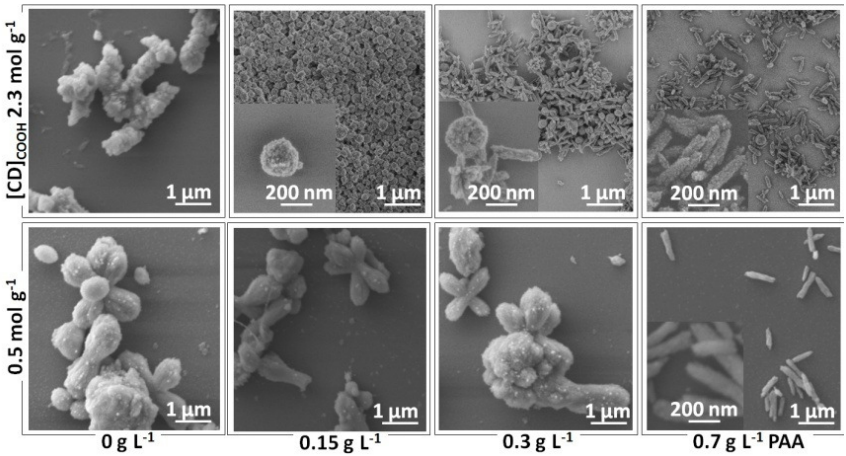


**Figure 7.3:** SEM overview evaluating the influence of carboxylation degree (0.5 and 2.3 mol/g) and poly(acrylic acid) concentration (0, 0.15, 0.3, and 0.7 g/L) on the morphology of the $CaCO_3$ nanocomposites. h. Polymer concentration is 0.7 g/L, and CD carboxylic degree is 2.3 mol/g. Sample $[CD]_{COOH}$ 0.5 had similar fluorescence and absorbance spectra.

**Table 7.1** Particle Sizes and ζ-Potentials of PAA-CD-$CaCO_3$ carriers in different media at pH 7.4.

| Shape | Medium | Size (nm)[a,b] | PDI | ζ-potential (mV)[b] |
|---|---|---|---|---|
| Rods | Millipore | 458 ± 20 | 0.18 | -38.9 ± 5.2 |
| Spheres | Millipore | 313 ± 15 | 0.14 | -36.7 ± 7.0 |
| Rods | HBSS | 2270 ± 95 | 0.28 | -24.5 ± 2.0 |
| Spheres | HBSS | 873 ± 112 | 0.29 | -24.9 ± 3.7 |
| Rods | RPMI | 700 ± 50 | 0.19 | -26.2 ± 10.8 |
| Spheres | RPMI | 439 ± 43 | 0.17 | -27.3 ± 11.8 |
| Rods | RPMI+FCS | 656 ± 42 | 0.24 | -11.8 ± 12.1 |
| Spheres | RPMI+FCS | 472 ± 36 | 0.24 | -13.3 ± 8.6 |

[a] Intensity-weighted size distribution. [b] Value ± Standard Deviation (n = 3). CD with 2.3 mol/g is used on the experiment. PDI: polydispersity index.

Aiming at the assessment of polymer charge on the final structure, similar experiments were performed using a combination of positively charged PEI and negatively charged PAA. Figure 7.4 shows the SEM overview of final structures precipitated for 48 hours at different PEI and PAA concentrations. Alone, PEI cannot prevent direct precipitation of large calcite crystals. By inclusion of PAA, final particles are under 1 μm in size. However, it is no longer possible to fully control the morphology as the nanoparticles highly aggregate, possibly as a result of electrostatic heteroaggregation. Moreover, the ζ-potential of the particles is around -31 ± 4.3 mV, which shows that PEI can absorb onto charged nanoparticles and interfere with the precipitation and self-assembly.

Considering the biocompatibility of calcium carbonate and its pH-sensitivity, this system can be potentially used as drug carrier featuring controlled release properties. In order to evaluate the stability of the carriers in a biological environment, the carriers were dispersed in different media, incubated for 4 hours and then characterized by size and zeta-potential. The results are summarized in table 7.1. In Millipore water, both rods and spheres have high colloidal stability, with zeta-potential ranging around -36 mV. The rods have a hydrodynamic diameter of 458 nm (PdI 0.15) while the spheres are 313 nm (PdI 0.16). In Hank's Balanced Salt Solution (HBSS) the dispersion stability decreases. Zeta-potential in both samples dropped to -25 mV while the size increased to over 1 μm (PdI 0.29).

The instability can be assigned to the high ionic strength of HBSS. When dispersed in RPMI-1640 medium without serum, the carriers are fairly stable, maintaining a zeta-potential of around -26 mV and hydrodynamic diameters of 700 nm (PdI 0.19) for rods and 440 nm (PdI 0.17) nm for spheres. In RPMI with 10% fetal calf serum (FCS), the zeta-potential dropped to –12 mV and the polydispersity index was over 0.3. This behavior is to be expected since the presence of serum proteins in the media is known to increase aggregation of negatively charged particles due to protein adsorption and corona formation.[40–42] To improve stability in protein-containing media, coating with biocompatible polymers, e.g. PEG, will be further investigated.

The safety of this delivery system is assessed on A549 cell line by means of cell membrane integrity (LDH) and metabolic activity via mitochondrial enzymes (MTT). As depicted in figure 7.5, the effect of particle concentration was evaluated for both geometries. According to LDH release, around 5% of A549 cells died after 4 h incubation, regardless of the nanohybrids geometry and concentration. MTT assay corroborates with the idea of no toxic behavior. For both types of particles and concentration, there is no statistical significant deviation from the high control. Early reports reveal toxicity associated with an increase in the cytosolic $Ca^{2+}$ concentration. This is associated with an increase in the overall

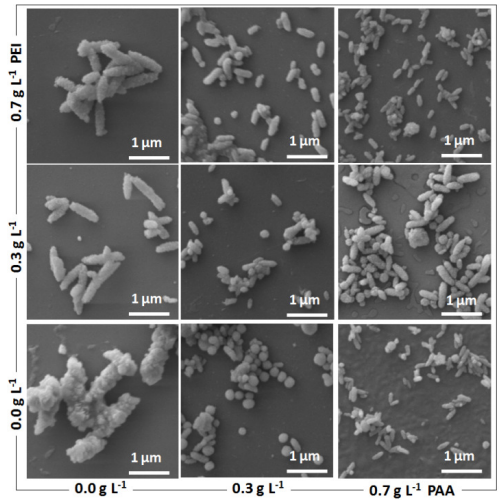


**Figure 7.4:** SEM micrographs of CD-$CaCO_3$ precipitated for 48 h by combining PAA and PEI at 0, 0.3, and 0.7 g/L. CD with 2.3 mol/g is used on the experiment.

calcium ion concentration when the particles dissolve. A closer inspection is shown on supporting information 7.9 and it can be concluded that at 6 and 12 mM of $Ca^{2+}$, no toxicity response was found.

In order to model the delivery of small molecules, the dye Rhodamine B was used. This dye was encapsulated via the co-precipitation method, in which the dye is dissolved in water prior to particle synthesis. Table 7.2 shows that the loading was around $8.6\times10^{-5}$ % for spheres and $7.4\times10^{-5}$ % for rods, with an encapsulation efficiency (EE) of 32 % and 27 %, respectively. This difference can be attributed to the higher surface area of spheres when compared to the rods.

Figure 7.6a shows the release of encapsulated dye from rod-like nanocomposites. At pH 4.8, the carriers rapidly dissolve and completely release the dye within 6 hours. At pH 7.4, the release starts with a burst within the first 3 h, in which almost 30% is released. This can be attributed to loosely bound dye molecules on the surface of carriers. From 6 to 84h, 10 % is released due to dye diffusion through the pores within the matrix. As a proof of concept, Figure 7.6b shows the pH-triggered release. The sample was kept at pH 7.4 for 54 hours. Within this period, 31 % of RhB was released. After that, the pH of the buffer was

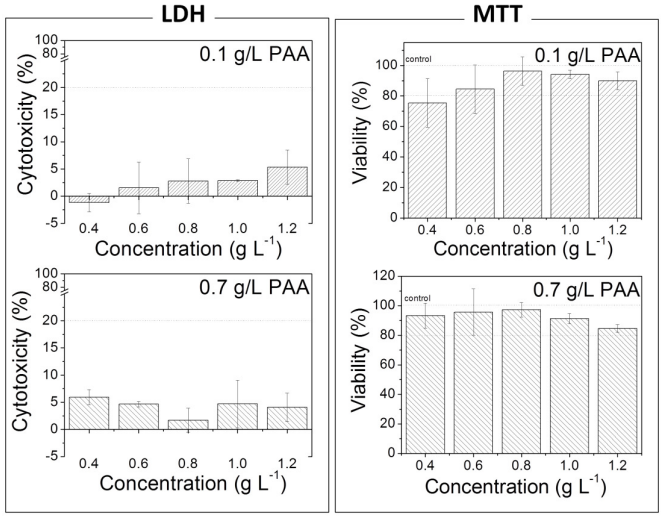


**Figure 7.5:** Cytotoxicity of both spheres (0.1 g/L PAA) and rod-like (0.7 g/L PAA) nanohybrids at different particle concentration assessed by LDH and MTT assay.

changed to 4.8 by addition of 1M HCl, which triggered the complete release by dissolution of the carriers within 5h.

## 7.4. Discussion

Materials with high carboxylic content, such as carbon nanodots,[32] graphene oxide[43] and acidic polyelectrolytes,[20,44] have been shown to affect the precipitation kinetics of calcium carbonate yielding crystals with intricate morphology and metastable polymorphs. Carboxyl groups that are pre-sent on the surface of CDs coordinate with $Ca^{2+}$ leading to an accumulation of ions at the nanodots, while at the same time depleting $Ca^{2+}$-ions in the volume phase. The addition of carbonate ions then leads to the nucleation of small primary crystallites, with the carbon dots as primary initiators for heterogeneous nucleation. The role of the carboxylic polymer PAA in the biomimetic mineralization of $CaCO_3$ is well documented[19,20,44,45] and is expected to enhance the effect described above for CD while at the same time further restricting crystal growth by adsorbing to positively-charged planes of the crystallites.[46,47] This retards both particle growth and uncontrolled aggregation and leads to controlled mesoscale self-assembly. Moreover, the crystallinity of both primary and final nanoparticles emphasizes the role of PAA as an additive and carbon nanodots as the main mediator for crystallization. Previous studies[20,44,45] revealed amorphous character of $CaCO_3$ if precipitation is mediated only by PAA at similar concentrations, while in this study, the carbon dot template causes the direct formation of crystalline $CaCO_3$.

As can be derived from the concentration-dependent behavior, the hierarchical structure of the hybrid nanoparticles is most likely to occur if the overall content of

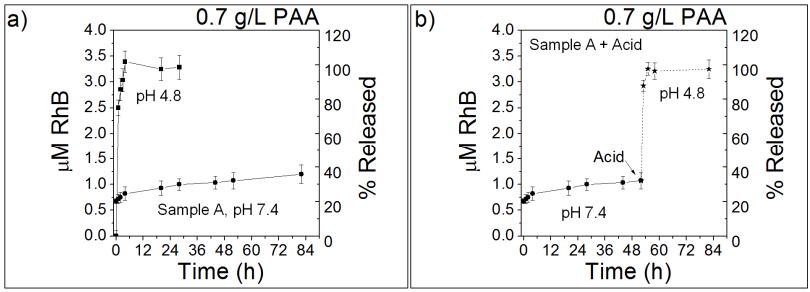


**Figure 7.6:** a) Release profile of Rhodamine B from 0.7 g/L PAA-CD-$CaCO_3$ at pH 4.8 and 7.4. b) pH-triggered release: after 56 h, sample A was divided into two and pH was changed from 7.4 to 4.8 using 1 M HCl. CD with 2.3 mol/g is used on the experiment.

PAA is high enough to avoid direct precipitation of large crystals and sufficiently cover the surfaces of the primary particles. The formation of the two distinct geometries may be explained by certain alignment of the disc-like primary particles during the mesoscale-assembly process (Figure 7.7). At low PAA concentration, due to high yield (0.15 g/L), the number of poorly coated crystallites in solution is high and the aggregation process tends to occur rapidly and without preferential organization.[48] This unordered assembly results in the formation of spheres with diameters of a few hundred nanometers and with 6 nm pore sizes. Increasing the PAA concentration to 0.7 g/L, the yield is lowered to 1.0 g/L due to growth inhibition, which leads to sufficient coverage of the anisotropic primary particles with PAA at specific growth planes resulting in controlled alignment during assembly. The final mesocrystal geometry is most likely a result of the anisotropic shape of the primary nanoparticles, which assemble into rod-like composite nanoparticles. The structuring of primary particles inside the rods (Figure 7.7, parallel white lines) suggests that rods are formed by planes of nanoparticles at a distance of around 10.1 ± 1.8 nm, which is very similar to the primary nanoparticle size (7.4 ± 2.1 nm). Once assembled, the nanoparticles are most likely held together by PAA/$CaCO_3$ coordination.

The influence of polymer charge on the final structure revealed the absence of carboxyl groups, when using PEI as the additive, direct precipitation of large calcite crystals can not be prevented. By combining both PEI and PAA, it is no longer possible to fully control the morphology as the nanoparticles highly aggregate, possibly as a result of electrostatic heteroaggregation which disturbs the controlled mesoscale assembly.

The particles showed reasonable stability in protein free RPMI medium. However, when introduced to media supplemented with proteins, the suspension tended to aggregate, as could be expected since the particles do not feature a protective layer of poly(ethylene glycol) or similar. The safety of this delivery system to the pulmonary epithelial cells was also assessed. Cytotoxicity experiments revealed that for both morphologies, there was no toxicity in both LDH and MTT assays. Special consideration is given to the toxicity associated with varying $Ca^{2+}$ concentration, as was previously reported for calcium phosphate particles.[49] The dissolution of such carriers increases the overall calcium ion concentration. This can lead to an elevation in the cytosolic $Ca^{2+}$ concentration and therefore induce apoptosis. A closer inspection with a control system using $CaCl_2$ shown on supporting information 7.9 reveals that at 6 and 12 mM of $Ca^{2+}$, no toxicity response was found. One of the main advantages of using $CaCO_3$ is that this mineral is already produced by the body and is generally recognized as safe.

**Table 7.2** Encapsulation efficiency and loading of Rhodamine-B.

| Shape | PAA (g/L) | Loading (%) | Loading rate (μM/mg) | Encapsulation Efficiency (%) |
|---|---|---|---|---|
| Spheres | 0.15 | $8.6\times10^{-5} \pm 4\times10^{-6}$ | $3.8\times10^{-1} \pm 1.8\times10^{-2}$ | 32.0 ± 8.4 |
| Rod | 0.7 | $7.4\times10^{-5} \pm 6\times10^{-6}$ | $3.2\times10^{-1} \pm 2.2\times10^{-2}$ | 27.4 ± 7.6 |

Value ± Standard Deviation (n = 3). Initial [RhB] 12 μM. CD with 2.3 mol/g is used on the experiment. Loading: % of mass encapsulated dye per total mass of particles. Loading rate: mM of encapsulated dye per total mass of particles. Encapsulation Efficiency: % encapsulated dye compared to initial amount.

Rhodamine B can be encapsulated with an encapsulation efficiency (EE) of 32% for spheres, slightly higher than for rods (27%). This can be attributed to the higher surface area of spheres when compared to rods. The release of encapsulated dye from rod-like nanocomposites occurs either by desorption-diffusion or carrier dissolution, depending upon the environmental pH. At pH 4.8, the release is complete within 6 hours due to rapid carrier dissolution. However at pH 7.4, loosely bound dye molecules desorb from the $CaCO_3$ surface within 6h, as can be seen by the initial burst release. From 6 to 84h, the slow rate of release is most likely the result of a desorption-diffusion mechanism. Considering that both polymer and the nanocomposite are negatively charged at neutral pH, electrostatic interaction can play a role in the release profile, especially at neutral-basic conditions, slowing down the release rate. Triggered pH release was achieved by shifting the pH from neutral to acid, as shown in Figure 7.6b. Here, the change of pH promotes fast release of dye molecules due to carrier dissolution.

## 7.5. Conclusion

In summary, carbon nanodots and poly(acrylic acid) sodium salt were used to modify the precipitation of calcium carbonate for the synthesis of porous $CaCO_3$ composite nanoparticles. The mesoscale assembly during the precipitation of CD-$CaCO_3$ allows the formation of porous organic-inorganic composite particles with controlled geometry. At low polymer concentration, spherical morphology is achieved while at higher concentration, rod-like structures are formed. Since the primary nanoparticles do not fuse together after assembly as a result of polymer stabilization, the carriers are porous and have rough surfaces. These pores, allow the occlusion of molecules within the $CaCO_3$ matrix, which was studied by loading a model low-molar dye, Rhodamine B. The release of the dye is governed by desorption-diffusion at pH 7.4 and by carrier dissolution at pH 4.8. Given the morphological control, simplicity of synthesis and pH-triggered release, the CD-$CaCO_3$ system can be a potential drug carrier. The ability to adjust the geometry while still maintaining appropriate size, medium stability and absence of toxicity highlights the potential use for biological applications. Rod-shaped $CaCO_3$ carriers can potentially benefit from better targeted-uptake when compared to spherical particles[50] as well as higher receptor-mediated accumulation.[14] With respect to

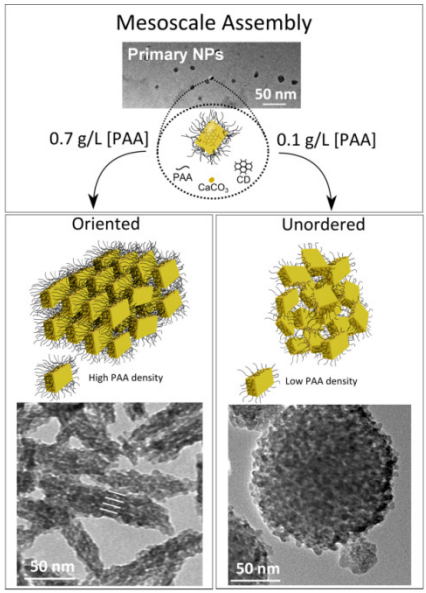


**Figure 7.7:** Schematic drawing and TEM micrographs of oriented and unordered mesoscale assembly mechanism proposed in this paper.

pulmonary delivery, these anisotropic particles can potentially benefit from lower phagocytosis clearance, due to the orientation-dependent uptake by macrophages.[51] Moreover, in the field of materials science, the knowledge on mesoscale assembly is valuable for a comprehensive control and design of inorganic crystals mediated by organic additives.

## 7.6. Acknowledgement

We thank Tochukwu Ogoke for assistance in the preparatory work and the Research Training Group GRK 1860, 'Micro-, meso- and macroporous nonmetallic materials: fundamentals and applications' (MIMENIMA) for funding.

## 7.7. References

This chapter was reprinted with permission from V. Lauth, B. Loretz, C. M. Lehr, M. Maas, and K. Rezwan, Chemistry of Materials, 2016, 28, 3796–3803. Copyright 2016 American Chemical Society. The correction issued in 2017 is already included in this dissertation: V. Lauth, B. Loretz, C. M. Lehr, M. Maas, and K. Rezwan, Chemistry of Materials, Chem. Mater., 2017, 29 (7), pp 3346–3346

The article is mainly based on the work of the first author and the author of this thesis Victor Rafael Lauth. The precise contributions of each author are listed below.

| Author | Contribution |
|---|---|
| Lauth, V. | Conceptualization of the work, design and implementation of experiments, data collection, analysis and interpretation, principle writing of the manuscript and revision of the article |
| Loretz, B. | Assisted in the design of the experiments and conceptualization of the work, data analysis, discussion and revision of the manuscript. |
| Lehr, C. M. | Gave conceptual advices and input, critical assessment of all experiments and revision of the manuscript. |
| Maas, M.* | Conceptualization of the work, data analysis, writing and revision of the manuscript. |

| Author | Contribution |
|---|---|
| Rezwan, K. | Gave conceptual advices and input, critical assessment of all experiments and revision of the manuscript. |

1. W. H. De Jong and P. J. a Borm, *Int. J. Nanomedicine*, 2008, **3**, 133–149.

2. H. Ai, *Adv. Drug Deliv. Rev.*, 2011, **63**, 772–88.

3. W. X. Mai and H. Meng, *Integr. Biol.*, 2013, **5**, 19–28.

4. K. Park, *ACS Nano*, 2013, **7**, 7442–7447.

5. S. K. Kim, M. B. Foote and L. Huang, *Cancer Lett.*, 2013, **334**, 311–8.

6. C. Tscheka, M. Hittinger, C.-M. Lehr, N. Schneider-Daum and M. Schneider, *Eur. J. Pharm. Biopharm.*, 2015, **95**, 151–155.

7. Y. Geng, P. Dalhaimer, S. Cai, R. Tsai, M. Tewari, T. Minko and D. E. Discher, *Nat. Nanotechnol.*, 2007, **2**, 249–255.

8. M. Bahadori and F. Mohammadi, *Tanaffos*, 2012, **11**, 18–22.

9. J. a. Champion, Y. K. Katare and S. Mitragotri, *J. Control. Release*, 2007, **121**, 3–9.

10. J. W. Nichols and Y. H. Bae, *J. Control. release*, 2014, **190**, 451–64.

11. P. Decuzzi, B. Godin, T. Tanaka, S.-Y. Lee, C. Chiappini, X. Liu and M. Ferrari, *J. Control. Release*, 2010, **141**, 320–327.

12. N. P. Truong, M. R. Whittaker, C. W. Mak and T. P. Davis, *Expert Opin. Drug Deliv.*, 2015, **12**, 129–142.

13. M. B. Fish, A. J. Thompson, C. a. Fromen and O. Eniola-Adefeso, *Ind. Eng. Chem. Res.*, 2015, **54**, 4043–4059.

14. P. Kolhar, A. C. Anselmo, V. Gupta, K. Pant, B. Prabhakarpandian, E. Ruoslahti and S. Mitragotri, *Proc. Natl. Acad. Sci.*, 2013, **110**, 10753–10758.

15. F. C. Meldrum and H. Cölfen, *Chem. Rev.*, 2008, **108**, 4332–4432.

16. H.-B. Yao, J. Ge, L.-B. Mao, Y.-X. Yan and S.-H. Yu, *Adv. Mater.*, 2014, **26**, 163–188.

17. H. Cölfen, *Curr. Opin. Colloid Interface Sci.*, 2003, **8**, 23–31.

18. S. Mann, in *Inorganic Elements in Biochemistry*, Springer Berlin Heidelberg, 1983, vol. 54, pp. 125–174.

19. B. J. McKenna, J. H. Waite and G. D. Stucky, *Cryst. Growth Des.*, 2009, **9**, 4335–4343.

20. V. Lauth, M. Maas and K. Rezwan, *J. Mater. Chem. B*, 2014, **2**, 7725–7731.

21. H. Cölfen and M. Antonietti, *Langmuir*, 1998, **14**, 582–589.

22. L. . Gower and D. . Tirrell, *J. Cryst. Growth*, 1998, **191**, 153–160.

23. J. Donners, B. R. Heywood, E. W. Meijer, R. J. M. Nolte and N. A. J. . Sommerdijk, *Chem. - A Eur. J.*, 2002, **8**, 2561–2567.

24. J. M. Donners, E. W. Meijer, R. J. M. Nolte, C. Roman, A. P. H. J. Schenning, N. A. J. M. Sommerdijk and B. R. Heywood, *Chem. Commun.*, 2000, 1937–1938.

25. A.-W. W. Xu, Y. R. Ma, H. Colfen and H. Coelfen, *J. Mater. Chem.*, 2007, **17**, 415–449.

26. H. Cölfen and S. Mann, *Angew. Chemie - Int. Ed.*, 2003, **42**, 2350–2365.

27. R.-Q. Song and H. Cölfen, *Adv. Mater.*, 2010, **22**, 1301–1330.

28. W. Li and C. Gao, *Langmuir*, 2007, **23**, 4575–4582.

29. X. Wang, H. Bai, Y. Jia, L. Zhi, L. Qu, Y. Xu, C. Li and G. Shi, *RSC Adv.*, 2012, **2**, 2154–2160.

30. S. Kim, S. H. Ku, S. Y. Lim, J. H. Kim and C. B. Park, *Adv. Mater.*, 2011, **23**, 2009–2014.

31. G. M. Neelgund, A. Oki and Z. Luo, *Mater. Res. Bull.*, 2013, **48**, 175–179.

32. S. Guo, M. Yang, M. Chen, J. Zhang, K. Liu, L. Ye and W. Gu, *Dalt. Trans.*, 2015, **44**, 8232–8237.

33. Y. Dong, H. Pang, H. Bin Yang, C. Guo, J. Shao, Y. Chi, C. M. Li and T. Yu, *Angew. Chemie - Int. Ed.*, 2013, **52**, 7800–7804.

34. Y. Wang and A. Hu, *J. Mater. Chem. C*, 2014, **2**, 6921–6939.

35. L. Cao, X. Wang, M. J. Meziani, F. Lu, H. Wang, P. G. Luo, Y. Lin, B. a. Harruff, L. M. Veca, D. Murray, S. Y. Xie and Y. P. Sun, *J. Am. Chem. Soc.*, 2007, **129**, 11318–11319.

36. N. Dhenadhayalan and K.-C. Lin, *Sci. Rep.*, 2015, **5**, 10012.

37. Y. Wang, P. Anilkumar, L. Cao, J.-H. Liu, P. G. Luo, K. N. Tackett, S. Sahu, P. Wang, X. Wang and Y.-P. Sun, *Exp. Biol. Med.*, 2011, **236**, 1231–1238.

38. S. Zhu, J. Zhang, S. Tang, C. Qiao, L. Wang, H. Wang, X. Liu, B. Li, Y. Li, W. Yu, X. Wang, H. Sun and B. Yang, *Adv. Funct. Mater.*, 2012, **22**, 4732–4740.

39. Y. Dong, J. Shao, C. Chen, H. Li, R. Wang, Y. Chi, X. Lin and G. Chen, *Carbon N. Y.*, 2012, **50**, 4738–4743.

40. T. L. Moore, L. Rodriguez-Lorenzo, V. Hirsch, S. Balog, D. Urban, C. Jud, B. Rothen-Rutishauser, M. Lattuada and A. Petri-Fink, *Chem. Soc. Rev.*, 2015, **44**, 6287–6305.

41. M.-Q. Gong, J.-L. Wu, B. Chen, R.-X. Zhuo and S.-X. Cheng, *Langmuir*, 2015, **31**, 5115–5122.

42. S. S. Raesch, S. Tenzer, W. Storck, A. Rurainski, D. Selzer, C. A. Ruge, J. Perez-Gil, U. F. Schaefer and C. M. Lehr, *ACS Nano*, 2015, **9**, 11872–11885.

43. C. Yao, A. Xie, Y. Shen, J. Zhu and H. Li, *Mater. Sci. Eng. C*, 2015, **51**, 274–278.

44. P. Kaempfe, V. R. Lauth, T. Halfer, L. Treccani, M. Maas and K. Rezwan, *J. Am. Ceram. Soc.*, 2013, **96**, 736–742.

45. S.-C. C. Huang, K. Naka and Y. Chujo, *Langmuir*, 2007, **23**, 12086–12095.

46. S. H. Yu, H. Cölfen, J. Hartmann and M. Antonietti, *Adv. Funct. Mater.*, 2002, **12**, 541–545.

47. S. G. Deng, J. M. Cao, J. Feng, J. Guo, B. Q. Fang, M. B. Zheng and J. Tao, *J. Phys. Chem. B*, 2005, **109**, 11473–11477.

48. A. N. Kulak, P. Iddon, Y. Li, S. P. Armes, H. Cölfen, O. Paris, R. M. Wilson and F. C. Meldrum, *J. Am. Chem. Soc.*, 2007, **129**, 3729–3736.

49. Y. C. Tseng, A. Yang and L. Huang, *Mol. Pharm.*, 2013, **10**, 4391–4395.

50. S. Barua and S. Mitragotri, *Nano Today*, 2012, **29**, 223–243.

51. J. a Champion and S. Mitragotri, *Proc. Natl. Acad. Sci.*, 2006, **103**, 4930–4934.

# 8. An evaluation of colloidal and crystalline properties of $CaCO_3$ nanoparticles for biological applications

## 8.1. Introduction

*Abstract: Biodegradable calcium carbonate carriers are a promising and safe nanoparticle platform, which might enable various applications as an engineered nanomaterial in health care, food and cosmetics. However, engineered nanoparticles can exhibit new forms of toxicity that must be carefully evaluated before being widely adopted in consumer products or novel drug delivery systems. To this end, we studied four common calcium carbonate particle systems (calcite nanoparticles, amorphous sub-micrometer and vaterite sub-micrometer and micrometer particles) and compared their behavior in biological medium and in cell culture experiments. The thermodynamically stable calcite phase is shown to maintain its morphological features as no phase transformation occurs. Size- and time-dependent phase transformation of the less stable vaterite particles are observed within 96 hours in cell medium. The protein serum albumin can be an effective inhibitor of phase-transition and it is shown to improve colloidal stability. The impact of the biological environment goes beyond protein-corona formation, as we observed rapid dissolution of amorphous particles in high ionic strength cell medium, but not in Millipore water. Cellular responses of human osteoblasts against $CaCO_3$ particles indicate that increased extracellular calcium ions improve viability and that particle internalization is not size-dependent. Useful insights for designing $CaCO_3$-based delivery systems are provided and also corroborate to the idea that intrinsic material properties as well as environmental conditions are of relevance for the successful implementation of dispersed $CaCO_3$ particles in drug delivery systems and in other applications.*

The use of engineered nanoparticles (ENPs) in consumer products is becoming increasingly prevalent.[1] Clothing,[2] cosmetic[1] and food industries[3] are just a few examples of today's use of ENPs. The particles are mainly applied as pigments and fillers, for the occlusion and delivery of active ingredients and as antimicrobial agents. Another field in which the use of nanoparticles holds great potential is nanomedicine,[4,5] especially considering tumor targeting, diagnostics, imaging and treatment.[6] With the increasing use of ENPs, the necessity for nanosafety assessments is well recognized,[2] as evidenced by the strong increase in the publications numbers within the past two decades.[7]

As a consequence of various strategies to trick the immune system, like change of particle aspect ratio or functionalization with stealth polymers and self-peptides, these colloidal systems are able to avoid clearance.[6,8,9] Accordingly, these materials can exhibit new forms of toxicity, especially as a result of long-term accumulation in the body.[10] To avoid such undesirable effects, biodegradable and biocompatible materials are a promising option. Food and Drug Administration (FDA)-approved polymers like chitosan and poly(lactate) (PLGA) received special attention as they are well tolerated by the body.[8] Another alternative is the use of endogenous materials, like calcium phosphate, calcium carbonate and phosphosilicates.[11] Calcium carbonate ($CaCO_3$) holds great potential, as it is highly pH-sensitive and dissociates into calcium and carbonate ions, which already are ubiquitous in the body.

$CaCO_3$ exists in six different crystal morphologies: the naturally occurring calcite, aragonite, vaterite and amorphous calcium carbonate (ACC) phase and the highly unstable ikaite and monohydrocalcite. Only calcite is thermodynamically stable, while aragonite and vaterite are slightly unstable and tend to transform into calcite in the presence of water/humidity.[12–14] The same is true of amorphous calcium carbonate which in nature often occurs as a precursor to the more stable polymorphs.[15] All $CaCO_3$ polymorphs have a certain solubility in water which is determined by the solubility product and scales with the thermodynamic stability of each crystal phase.[16] This instability is more pronounced at the nanoscale, at which solubility and reactivity increases due to an enhanced surface to volume ratio.[17] Additionally, the dissolution rate is known to be highly dependent on the intrinsic nature of the particles (composition and crystal phase)[15] as well as on the environmental conditions (pH, presence of proteins and calcium-chelating moieties, ionic strength).[18–20] Moreover, the dissolution of nanoparticles in biological medium can impact the biological systems interacting with the material, potentially changing the toxicity behavior from nano to ion-related.[7] Given that, to properly design $CaCO_3$-based drug delivery systems (DDS) or similar nanostructures with dispersed $CaCO_3$ particles considering particle solubility in the respective media is critical. Furthermore, colloidal stability and consequently biological availability of $CaCO_3$ particles could be influenced by their crystal phase and morphology as a consequence of different surface properties of the nanomaterials including their interactions with media biomolecules.

As a result of the detailed and inspired studies of $CaCO_3$ biomineralization, a vast number of publications report the design of $CaCO_3$ particles for drug delivery. However, just for a fraction of these publications in vitro or in vivo studies were performed.[21–65] The latter studies evaluated different aspects of the $CaCO_3$-cellular interactions: intracellular behavior,[36,65] pH modulation,[37] bubble generation,[34,35,53]

bone remodeling,[24] photothermal therapy,[22,28,43,49] drug / protein delivery,[21,23,25–27,29–33,38,41,42,46–48,50–52,60–62] gene transfection,[44,45,54–59] cellular uptake,[63] toxicity [40,65] and bioavailability studies.[39,64,65] Among these publications, crystalline particles like calcite, vaterite and aragonite[38] phases have been utilized. These particle-systems varied in size from bulk material, to micrometer (1 – 1.5 µm), sub-micrometer (150 – 800 nm) and nanometer (30 – 100 nm) particles. In the case of amorphous carriers, the range of particle size was narrower, from 100 to 230 nm.[44–49] In some cases, the interplay of both amorphous and crystalline $CaCO_3$ phases was also reported.[24,41–43] In others, the crystallinity of the particles was not described.[50–65] Moreover, the aforementioned systems were tested with different cell culture media, incubation periods and cell lines. While most studies report viable nanoparticle systems in their own context, comparing the results is a challenging task. The lack of standardization when assessing biological responses[66] along with the incomplete information on the colloidal characterization makes it difficult to generalize the results, especially considering the real-live performance of particle-based drug delivery systems.

With the above discussion in mind, we designed a study that would allow us to compare the biological behavior of different $CaCO_3$ systems with varied crystallinity, solubility and colloidal properties. To this end, we analyzed the material properties of four different types of $CaCO_3$ particles commonly described in the literature as potential drug delivery systems and investigated their biological behavior against human osteoblasts in the Dulbecco's Modified Eagle's Medium (DMEM). Here, we focused on the changes in material properties in the cell medium and on the impact of the particles on the cells. For our study, we chose calcite, ACC particles, and vaterite particles in the range of 90 nm to 1 µm which we consider representative in regard to polymorphism and size of those described in the literature as potential drug delivery systems.

## 8.2. Experimental section

### 8.2.1. Materials

Calcium chloride ($CaCl_2$ dihydrate, purity > 96 %), sodium carbonate ($Na_2CO_3$, purity > 99.5 %), poly(acrylic acid) sodium salt (PAA, Mw 8000 g/mol, 45 wt % in water), bovine serum albumin (BSA, lyophilized powder), glycerol (Gly, purity > 99.5 %), sodium hydrogen carbonate ($NaHCO_3$, purity > 99.5 %), ethylene glycol (EG, purity ≥ 99 %) were purchased from Sigma-Aldrich and used without further purification. The experiments were performed using double deionized water

with a conductivity of 0.04 mS/cm from Synergy (Millipore, Darmstadt, Germany).

Cell culture tests were carried out on human osteoblast cells (HOB, lot no. 232R020412 obtained from Provitro - Germany). Dulbecco's Vogt modified Eagle's minimal essential medium (DMEM, high glucose), antibiotic-antimycotic (AB/AM), Alexa Fluor 488 phalloidin (AF488) were obtained from Invitrogen (Germany). Fetal calf serum (FCS), phosphate buffered saline (PBS), trypsin/ethylenediamine tetraacetic acid (0.25% Trypsin, 0.02% EDTA), Triton X-100, 4′,6-diamidino-2-phenylindole (DAPI, 0.5 µg/mL), paraformaldehyde (PFA, 95.0-100.5%), osmium tetroxide solution ($OsO_4$, 4% in water), glutaraldehyde solution (Grade 1, 25% in water) and an epoxy embedding medium kit (Epon 812 substitute) were purchased from Sigma-Aldrich (Germany). The water-soluble tetrazolium salt (WST-1) cell toxicity assay (Roche Diagnostics GmbH, Germany) and the lactate dehydrogenase (LDH) Pierce assay (Thermo Scientific, Germany) were directly purchased from the suppliers.

### 8.2.2. Synthesis of crystalline and amorphous nanoparticles

Calcite nanoparticles, purchased from PlasmaChem GmbH (Berlin, Germany) are produced by a sol-gel process and used as purchased. Amorphous particles were prepared as previously described.[67] In short, 10 mL aqueous solution with a final concentration of 1.9 g/L of PAA and 12 mM of $CaCl_2$ was prepared. To mineralize the particles, an aqueous solution of $Na_2CO_3$ was added to the reach the final concentration of 12 mM. The suspension was centrifuged at 5000 rpm for 10 minutes, the supernatant discarded and particles dried in an oven at 70 °C for 1 hour.

Vaterite particles were prepared in a similar way as previously reported.[37,68–70] Micrometer particles were synthesized in a water:EG solution (1:6, v/v). First, 207 µL of 2 M $CaCl_2$ aqueous solution was first added to 4.15 mL of EG solution, stirred for 5 min and followed by 415 µL of 1 M $NaHCO_3$ aqueous solution and 227 µL of water. The final concentration of carbonate was kept equimolar at 83 mM. The solution turned turbid after 5 minutes, indicating the formation of particles. After 1 hour stirring at 500 rpm, 30 mL of 100% ethanol was added to the suspension. Particles were collected by centrifugation at 5000 rpm for 10 min. This washing step was repeated twice and the collected particles were dried at 70°C for 2 hours. Sub-micrometer particles were prepared in a similar fashion but with a few modifications. The 1:6 water:EG solution was substituted by water:EG:Gly 1:1.25:3.7 in volume. Both $CaCl_2$ and $NaHCO_3$ aqueous solutions were added to a 4.15 mL solution containing 1.04 mL of EG and 3.11 mL of Gly.

The final concentration of calcium and carbonate was kept equimolar at 83 mM. The solution remained transparent for about 1 hour. The dispersion turned turbid after this period. Particles were collected by centrifugation after 2h 30min, followed by washing the particles twice in 100% ethanol and drying at 70°C for 2 hours. For experiments without BSA-stabilization, the particles were dispersed in the respective medium in an ultrasound bath for 10 minutes.

### 8.2.3. Particle-stabilization by BSA

Dried particles were dispersed in 0.2% BSA in Millipore water to prepare 1.2 g/L particle concentration. The suspension was ultrasonicated for 15 minutes to ensure that no aggregates remained in solution and to fully coat the particles. Afterwards, it was centrifuged for 10 minutes at 5000 rpm and dried at 70°C for 1 hour.

### 8.2.4. Calcium-ion release from nanoparticles

The calcium content in the supernatant was quantified using the o-cresolphthalein complexone colorimetric kit (Fluitest CA-CPC). Briefly, an amount of dried particles were added to the respective medium to prepare a particle concentration of 1.2 g/L. The suspension was serially diluted in the same medium to prepare 0.6, 0.3, 0.15 and 0.075 g/L. The suspensions were centrifuged for 10 minutes at 5000 rpm. 10 µL of the supernatant was added to a 96-well plate containing 50 µL of reaction mixture 1 (reagent obtained in the kit). 50 µL of reaction mixture 2 was added and the well plate was shaken for 30 s to allow homogeneous mixing. The plate was incubated for 10 minutes at room temperature (RT) and the absorbance was measured at 570 nm with plate reader. The calcium concentration was calculated using a standard curve by a serial dilution of the 2.5 mM standard acquired with the kit.

### 8.2.5. Toxicity profile assessment

To assess toxicity of the $CaCO_3$ particles, cell viability at different concentrations was tested in a similar way to [71], by means of membrane integrity via LDH release (Pierce assay) and metabolic activity via mitochondrial activity (WST-1 assay, Roche). Particles stabilized by BSA were centrifuged and sterilized overnight under a UV lamp and redispersed in DMEM at different concentrations. Human osteoblast cells (4th to 11th passage) were cultured in DMEM supplemented with 10% heat-inactivated FCS and 1% antibiotics/antimycotics in an incubator (C200, Labotect Labor Technik, Germany) at 37 °C with 10% $CO_2$ and 95% relative humidity (RH). One day prior to the experiments, the cells were

detached and seeded in a 24-well plate at a density of $2 \times 10^4$ cells per well. On the following day, the dispersions were added and incubated for 24 h. In addition, for the WST-1 assay, cells grown in culture medium were set as high control (100% cell viability), and others incubated with Triton X- 100 (2%, w/v) were used as low control (0% cell viability). For the LDH assay, the cytotoxicity was calculated relative to Triton X-100 as high control and cells in culture medium as low control. Samples were measured in triplicates and evaluated as mean and standard deviations (SD).

Particle uptake studied via electron microscopy. For Transmission electron microscopy (TEM) analysis, a similar procedure to [72] was used. Shortly, osteoblasts were washed once with PBS, detached with Trypsin/EDTA and transferred to 2 mL Eppendorf cups. The cups were centrifuged at 6000 rpm for 6 min, fixed with standard 2.5% glutaraldehyde, 2.5% formaldehyde in 0.1 M Na-cacodylate for 1 h at RT. After removal of the fixative, the cells were washed several times with phosphate buffer and post-fixed with Osmium tetroxide solution for 1 hour at RT. The black pellet was washed twice and dispersed in 2% agar (Sigma-Aldrich) in Millipore water, and allowed to solidify at 4°C. The pellet in agar was cut into squares of about 1 mm wide. The blocks were dehydrated in a graded series with ethanol (twice for 5 minutes in 30% and 50% ethanol, 3 times for 10 minutes in 70%, 90% and twice for 15 minutes in 100% ethanol). Blocks were embedded in Epon 812. Ultrathin sections were taken with an ultramicrotome (Ultracut R, Leica, Wetzlar, Germany). No surface markers were used (uranyl acetate or ruthenium red), in order to enhance the contrast of intracellular components, as these are not the focus of the analysis.

### 8.2.6. Characterization techniques

For the measurement of particle size and zeta-potential, dried particles were ultrasonicated for 10 minutes in the respective medium. Particle size and zeta potential were determined by a Zetasizer after 4 h of incubation (Malvern Instruments, Nano ZSP). The data is given as mean ± standard deviation (SD) based on three independent measurements. The aggregation behavior was evaluated in terms of the particle size distribution and polydispersity index (PDI). The morphology of the carriers was evaluated by scanning electron microscopy (Zeiss, SUPRA 40), with an acceleration voltage of 15 kV as well as transmission electron microscopy with a Zeiss EM 900 (Zeiss, Oberkochen, Germany) at 80 kV. Images were acquired using a CCD-camera (TRS, Dünzelbach, Germany) with the software ImageSP (TRS). X-ray diffraction (XRD) analysis was carried out using a JSO-Debyeflex 2002 device, with Cu Kα radiation ($\lambda$ = 1.542 Å). The samples

were ground to a powder, placed on the holder with silicone grease and scanned from 20° to 50°, 1 second per step. UV- Vis spectroscopy was performed on a Multiskan Go device (Thermo Scientific). Thermogravimetric measurements (TGA) were performed in STA 503 (Bähr Thermoanalyse) with a heating rate of 4 °C/min under 2 L/min of atmospheric air. The specific surface area (SBET) of the samples was determined by nitrogen adsorption (Belsorp-Mini, Bel Japan, Osaka, Japan), using the BET-method. The pore size distribution was determined by the BJH method from the adsorption/desorption hysteresis of the BET-isotherms.

## 8.3. Results

### 8.3.1. Material characterization of the $CaCO_3$ particles

The $CaCO_3$ particles were fully characterized prior to the cell experiments. Figure 8.1 shows a TEM overview of the particles immediately after synthesis (vaterite and ACC) or as purchased (calcite). The calcite particles are monodispersed and exhibit a rhombohedral shape with a particle size of 90 ± 10 nm. The amorphous particles are synthesized in Millipore water by the complex coacervation of [$Ca^{2+}$] ions and PAA, followed by mineralization with $Na_2CO_3$, as previously reported by us.[67] As the size can be controlled by complexation time and PAA concentration, the smallest particle size that can be obtained with this method is 250 ± 20 nm in diameter. Due to the nature of the synthesis, smaller nanoparticles (8 nm particles in diameter) are also formed.[73] Vaterite particles are prepared in a water-solvent mixture.[37,68–70] Sub-micrometer particles are prepared in 1:1.25:3.7 water:EG:Gly in volume ratio and yield particles size of 600 nm ± 20 nm while micrometer particles are prepared in 1:6 water:EG, which yields 1 µm ± 0.1 µm particles. Supporting Figure 8.1 shows an XRD analysis of the crystal phases of calcite and vaterite particles, as well as the absence of reflexes in the amorphous phase. BJH characterization of the samples showed that both vaterite particles are porous, with a mean pore diameter of 7 nm for sub-micrometer and 9 nm for micrometer, respectively (Supporting Figure 8.2). The amorphous sub-micrometer particles as well as calcite nanoparticles are not porous.

### 8.3.2. Time-dependent phase-transformation in DMEM

It is well known that thermodynamically metastable phases tend to transform into more stable phases, like calcite.[15] This transformation is triggered in the presence of water/moisture[12] and can be a concern when designing $CaCO_3$-based DDSs. To analyze the phase-transformation in cell culture medium and to assess the influence of protein-coating in this transformation, $CaCO_3$ particles were dispersed in DMEM and SEM images were taken at 24 and 96 hours after initial dispersing.

The SEM analysis of the samples dispersed in DMEM for 24 and 96 h and with or without BSA-coating is summarized in Figure 8.2. In the absence of BSA-stabilization, it was observed that calcite nanoparticles neither dissolve in DMEM nor grow within the time frame of the experiment. Moreover, the X-ray diffraction patterns (Supporting Figure 8.3) confirm that calcite does not phase-transform within 96 h. For vaterite sub-micrometer particles, morphological changes at 96 hours from rods to micrometer-sized, rhombohedral-shaped crystals indicate a phase transformation. This is also observed in the XRD data, where a peak at 29 ° indicates the complete transformation into the calcite phase. On the other hand, micrometer-sized vaterite particles do not phase-transform into calcite and maintain their morphology and size. Amorphous sub-micrometer particles are not

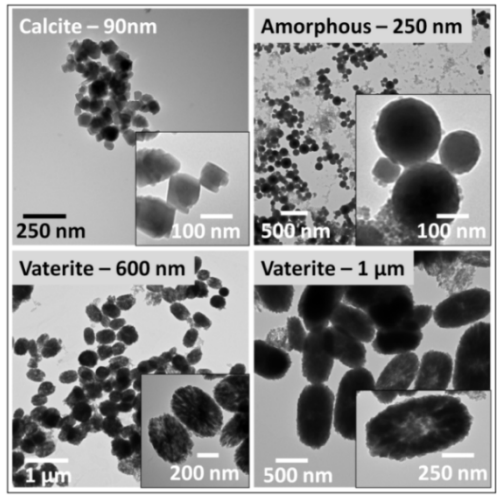


**Figure 8.1:** TEM overview of calcite, amorphous, micrometer and sub-micrometer vaterite particles. Crystalline and amorphous particles are dispersed in Millipore water while vaterite particles in ethanol.

shown in the picture because of their complete dissolution in DMEM.

The presence of BSA can act as a phase-stabilizer of less stable polymorphs. The shape and size of BSA-coated calcite nanoparticles and vaterite microparticles is not affected by the presence of the protein and both size and crystallinity remain constant throughout the experiment. As opposed to the BSA-free solution, BSA-stabilized sub-micrometer vaterite particles remain stable in solution for 96 h without appreciable change in shape or size. A closer inspection of the XRD data (Supporting Figure 8.3) reveals that the rate of the transformation is drastically reduced by the protein coating. It is worth mentioning that the phase-transformation appears to be both size-dependent, as it just occurs in the sub-micrometer vaterite particles as well as time-dependent, as no phase transformation is observed after 24 h. This behavior can be explained by the higher surface-to-volume ratio of the smaller particles which goes along with higher instability and enhanced solubility.[68] For instance, the surface area of micrometer vaterite particles is 44 $m^2/g$, which is low compared to sub-micrometer sized particles with

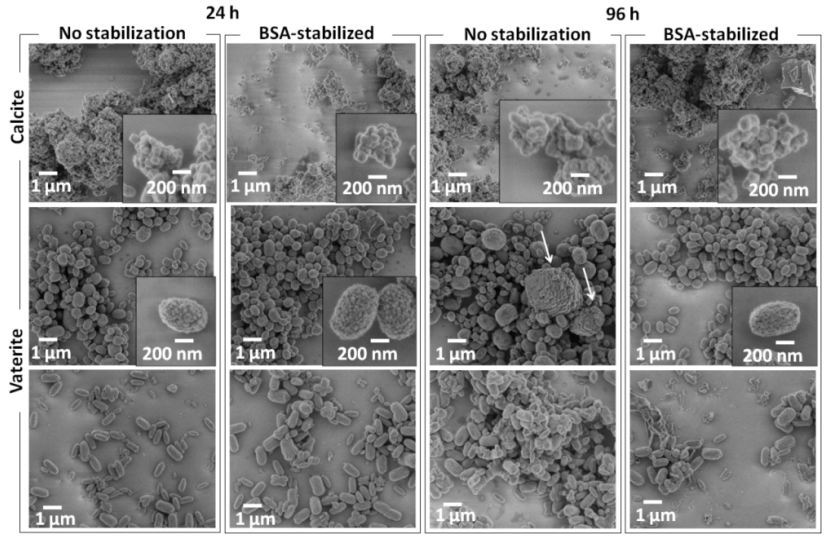


**Figure 8.2:** SEM overview of calcite, amorphous, micrometer vaterite and sub-micrometer vaterite particles after 24 and 96 hours of incubation in DMEM. Both bare and BSA-stabilized particles are reported. Amorphous particles immediately dissolved in DMEM and therefore are not shown. Arrows indicate the possible formation of calcite microcrystals.

104 $m^2/g$. Finally, the addition of BSA does not prevent the dissolution of the amorphous particles in DMEM.

### 8.3.3. Colloidal stability in different media

As shown above, the presence of proteins can alter the phase transformation of $CaCO_3$ particles in cell culture medium. The presence of BSA in medium and its adsorption at the surface of the nanoparticles directly affect the colloidal stability, as shown in Figure 8.3. The physisorption of the protein can be quantified via thermogravimetric. In the absence of protein (Figure 8.3a), calcite particles do not show a mass loss up to 600 °C. As the temperature rises, calcination takes place, which accounts for around 50 % of the weight loss. Vaterite particles show a similar trend. Up to 200 °C, absorbed and intrinsic water are removed. Between 200 and 300 °C left-over solvents are removed, followed by a calcination reaction. The amorphous particles show the highest weight loss of about 70 % ± 10 %, from which around 20 % can be attributed to absorbed water, 25 % from PAA and 17 % from calcination. By comparing the TGA data in the presence of proteins (Figure 8.3d) it is possible to calculate the weight loss associated with protein absorption within the temperature range from 210 °C to 405 °C. For calcite nanoparticles, BSA accounts for 4.2 ± 3.1 % of the weight loss. This relates to around 0.45 mM of BSA per g of particle. In the case of the micrometer vaterite particles, 3.1 ± 2.9 % of the weight is related to BSA, which represents approximately 0.60 mM of BSA / g of particle. Sub-micrometer particles absorbed 5.0 ± 4.5 % of its weight, around 0.75 mM of BSA / g of particle. Amorphous particles did not absorb any appreciable amount of protein.

$CaCO_3$ has an isolectric point around pH 6 in ultrapure water,[74] and is therefore negatively charged at physiological pH. In Millipore water at pH 7 and in the absence of BSA, the dispersed calcite particles have a mean hydrodynamic diameter of 91 ± 16 nm (Figure 8.3b) and show good colloidal stability (PDI 0.29) with a zeta-potential of -29.6 ± 2.3 mV (Figure 8.3c). The amorphous particles also show good stability with the lowest zeta-potential in water, around - 46.8 ± 3.6 mV, while the hydrodynamic size is 220 ± 35 nm. The high zeta-potential value can be explained by the inclusion of PAA molecules, which are negatively charged at neutral pH. The micron-sized vaterite particles showed strong agglomeration and sedimentation in water which prevented accurate DLS measurements. The sub-micrometer vaterite particles have a hydrodynamic size of around 712 ± 40 nm and zeta-potential of - 16.7 ± 1.3 mV.

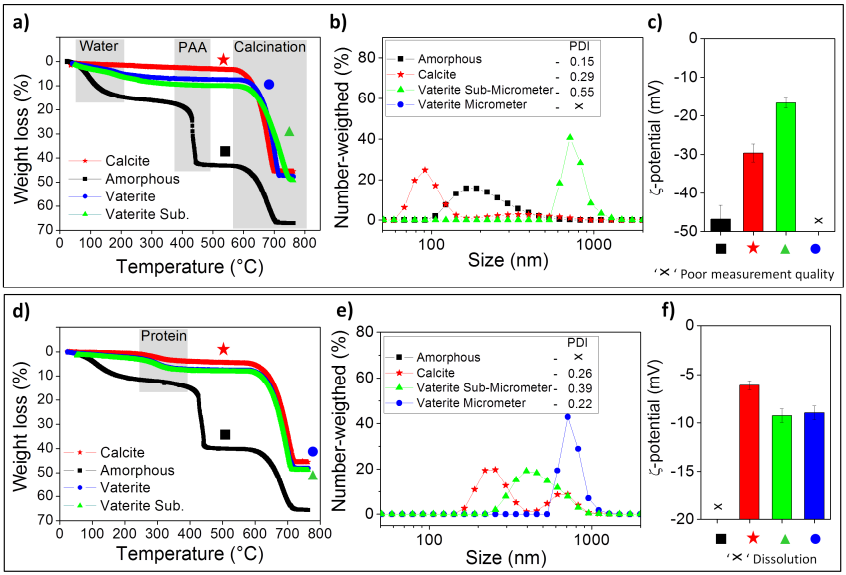


**Figure 8.3:** Thermogravimetric analysis (a,d), number-weighted particle size distribution (b,e) and zeta-potential (c,f) of calcite, amorphous, micrometer and sub-micrometer vaterite particles. (a) Dried bare particles, (b – c) Bare particles dispersed in Millipore water, (d) Dried BSA-stabilized particles, and (e – f) BSA-stabilized particles dispersed in DMEM.

When the bare particles (in absence of BSA) were dispersed in DMEM, rapid agglomeration and sedimentation took place and therefore DLS measurements were not possible. The instability can be related to the high ionic-strength of the medium, which reduces the Debye-length and the repulsion forces between nanoparticles.[75] On the other hand, BSA-stabilized suspensions are partially stable in DMEM, showing PDI values of around 0.3 and zeta-potential around -10 mV. In medium, the calcite dispersion exhibited a mean hydrodynamic diameter of 255 ± 30 nm (Figure 8.3e) and a zeta-potential of -6.1 ± 1.0 mV (Figure 8.3f). In contrast to dispersions in Millipore water, amorphous particles dissolved upon redispersion in DMEM. Note that this dissolution is not caused by a low pH, but is instead probably a result of chelating of $Ca^{2+}$ ions by the various amino acids and phosphate salts contained in DMEM. Vaterite microparticles showed a size of 712 ± 50 nm and a zeta-potential of about - 9.2 ± 1.0 mV. Sub-micrometer vaterite particles have a hydrodynamic size of around 396 ± 30 nm and a zeta-potential of -

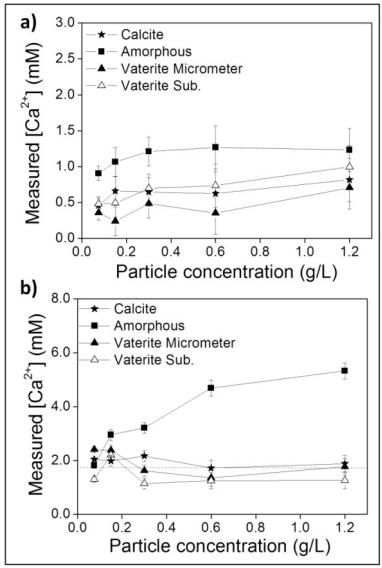


**Figure 8.4:** Dissolution of calcite, micro- and sub-micrometer vaterite and amorphous particles upon serial dilution in aqueous medium. (a) Bare particles (no BSA-stabilization) dispersed in Millipore water pH 7. (b) BSA-stabilized particles dispersed in DMEM pH 7.4.

8.9 ± 1.0 mV. In DMEM, it is observed that the stabilization of particles with 3 to 5 % of BSA can hinder aggregation and improve colloidal stability of all types of particles (Figure 8.3b, c, e, f). These findings are also supported by a previous report.[36]

### 8.3.4. Dissolution behavior in different media

As shown previously, the incorporation of BSA improves colloidal stability and slows down the rate of phase transformation of sub-micrometer vaterite particles. Serial dilution of particles along with determining the free calcium ions allowed us to examine the dissolution behavior of each particle type in both water and DMEM. In Millipore water, bare particles are tested while in DMEM, BSA-stabilized particles are used due to the improved colloidal stability. In water, all particles are stable with low calcium ion release (Figure 8.4a). At 1.2 g/L, amorphous particles show the highest calcium ion release, approximately 1.2 ± 0.3 mM, followed by vaterite sub-micrometer particles at 0.9 ± 0.2 mM, calcite nanoparticles at 0.8 ± 0.2 mM and vaterite microparticles at 0.7 ± 0.1 mM.

If the particles are dispersed in DMEM, the minimum calcium concentration detected is 1.80 ± 0.2 mM, which corresponds to the calcium concentration in the

medium (Figure 8.4b). Crystalline particles remain stable and barely dissolve. The calcium concentration remains constant with values ranging around 1.8 mM for all different particle concentrations. Amorphous particles on the other hand, readily dissolve in DMEM, increasing the $Ca^{2+}$ concentration up to 6.0 ± 0.3 mM at 1.2 g/L. The dissolution of amorphous particles is confirmed by turbidity measurements at 450 nm and by SEM. Moreover, additional experiments of BSA-coated particles in water and bare particles in DMEM (Supporting Figure 8.4) revealed similar results.

### 8.3.5. Toxicity profile of $CaCO_3$ particles against HOBs

Toxicity experiments were performed using a HOB cell line and incubated with BSA-stabilized particles for 24 h in serum-free DMEM at different particle concentrations (Figure 8.5). Two standard experiments were performed: the LDH release assay, which indicates membrane damage with increasing LDH release and hence toxicity, and the WST-1 assay which indicates viability by quantifying the mitochondrial activity of the investigated cells. Amorphous particles did not show any significant deviation from the control (pure medium) both for LDH release and for viability (Figure 8.5a and b). However, it must be noted that for mitochondrial activity, the values approached 80 % indicating a possible toxic effect of the amorphous particles or its constituents that are released upon the already described dissolution of the particles in DMEM. Calcite particles displayed conflicting results. Regarding LDH release, a concentration-dependent increase in LDH release was observed. At higher particle concentration, 1.2 g/L, the LDH release showed significant values close to toxic levels (20%). On the contrary, viability experiments displayed improved viability, up to 125% at the highest particle concentration. Both types of vaterite particles show no significant deviations from the control for LDH release. Moreover, as with calcite, improvement in viability is observed for sub-micrometer particles at 0.6 g/L and at 1.2 g/L for micrometer-sized particles.

Control experiments were performed using $CaCl_2$ and PAA and are shown in Figure 8.5c and d. Poly(acrylic acid) can be toxic depending on its molecular weight. According to the LDH release, no significant values are observed when compared to the control. However, the viability decreases considerably at 1.9 g/L of PAA, which is similar to the concentration of PAA used in the preparation of the amorphous particles. At lower concentrations, 0.15 and 0.7 g/L, no toxic effect can be observed. In the calcium chloride control experiments, optimal conditions for cell viability can be obtained by adding additional $CaCl_2$ up to 2 mM to DMEM

medium, while higher concentrations reduce cell viability and also show an increase in membrane damage.

By comparing the experiments using $Ca^{2+}$ as control and the ones with crystalline particles, better viability for crystalline particles is observed (around 150%) than for 0.5 mM [$Ca^{2+}$] as control (127 ± 15%). Since in both experiments the extracellular calcium is kept roughly the same, around 2 mM and 2.3 mM respectively, the difference in viability cannot just be explained by the elevation in the extracellular calcium concentration. Accordingly, due to the particle uptake followed by lysosomal dissolution (see below), the increase in intracellular calcium levels might cause even stronger cellular excitation, and therefore cellular viability.

Live-dead staining experiments were performed to validate the aforementioned experiments and the results are shown in Supporting Figure 8.5. In these experiments with all particle types, all cell cultures are observed to be 100% viable for a particle concentration of 0.3 g/L. By analyzing fluorescent micrographs of cells incubated with 0.3 g/L of particles (Supporting Figure 8.6), no morphological alterations were observed.

### 8.3.6. Particle-dependent uptake by human osteoblasts

Calcite nanoparticles are internalized by HOB cells, as observed on microtome sections analyzed via TEM (Figure 8.6). As a result of trypsinization, the cells appeared to be spherical with a diameter of about 15 to 20 µm. Since the cells were not stained with surface markers for practical reasons, the identification of intracellular membranes was not optimized. Control experiments with cells incubated in the absence of particles also show spherical cells in which the mitochondria could be observed as a denser region (Supporting Figure 8.7). The embedding resin that encloses the cell has a lighter colour, which allows for good distinction between cells and resin. When incubated with calcite nanoparticles, the size of the nanoparticles (90 nm) closely matches the size of the microtome slices (60 – 85 nm). Therefore, entire nanoparticles can remain in the slice and can be observed as dark dots in the TEM images. Internalized nanoparticles are located within endosomes. In the case of amorphous particles, which readily dissolved in DMEM, no particles can be observed within or outside the cells.

Due to the large size of the sub-micrometer and micrometer vaterite particles, these particles are shattered during slicing. What remains appears as an open space with a shape similar to the initial particles. As these spaces are transmitting, they appear as brighter regions dotted with remaining bits of $CaCO_3$ (dark dots). Both

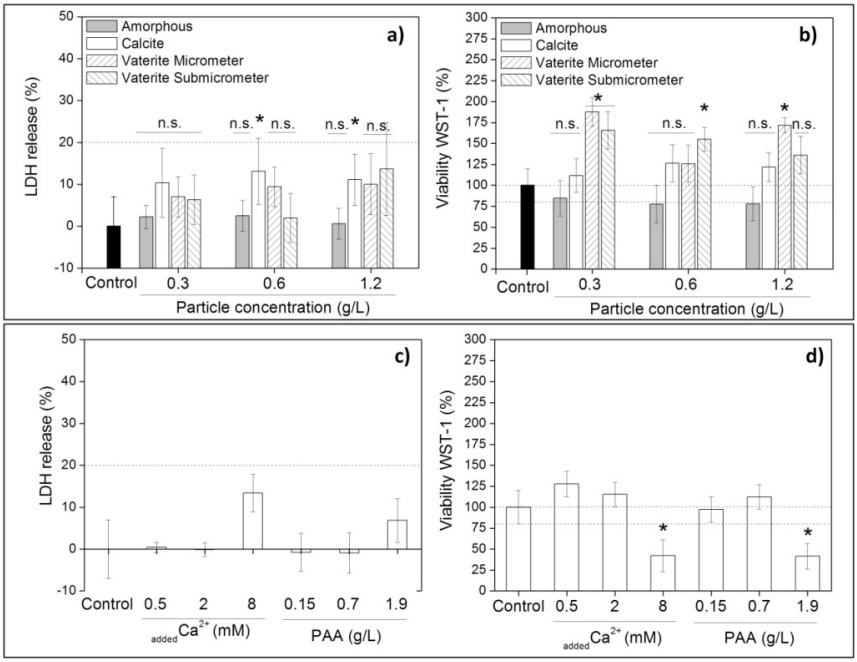


**Figure 8.5:** HOB intracellular LDH release (a, c) and mitochondrial viability (b, d) when incubated with calcite, amorphous and vaterite particles at different particle concentration as well as with $CaCl_2$ and PAA. (a,b) incubation with BSA-stabilized particles. (c, d) control experiments using $CaCl_2$ and PAA. * Significant value $p < 0.05$, n.s. Non significant value.

types of vaterite particles seem to be internalized and are located within endosomes.

Upon internalization, the particles can be dissolved in the acidic environment of the lysosomes. As discussed above, increased intracellular $Ca^{2+}$ levels could be the reason for elevated mitochondrial activity as observed via the WST-1 assay (Figure 8.5). Supporting Figure 8.8 shows fluorescent micrographs of intracellular calcium stained with Fluo-3 AM. Analysis of the images indicates a higher calcium concentration in the cytosol than in the nucleus, but no clear significant distinction between the different particle types could be observed.

## 8.4. Discussion

The phase transformation of less stable phases to calcite is a phenomenon that occurs in air [12,14] and in aqueous solutions.[13,68] The observed phase transformation of sub-micrometer particles is a function of the increasing surface-to-volume ratio and overall free energy, with decreasing particle size. Moreover, the ion-exchange mechanism that leads to phase transformation is dependent on the diffusion rate, which is also enhanced with a higher surface-to-volume ratio.[68] The phase-transformation is usually accompanied by changes in morphology and size, which can alter the colloidal stability and the biological responses of crystalline particles. Our findings suggest that the adsorption of BSA on the surface of $CaCO_3$ crystals can hinder the phase transformation of sub-micrometer vaterite particles. These results are supported by previous studies,[37] which stated that nanosized vaterite particles can be stabilized by 2% BSA in PBS. The use of proteins to modulate crystal precipitation, morphology and crystallinity is also observed in nature.[76,77] Accordingly, proteins and analogous polyionic polymers have been widely studied in the field of biomineralization for modifying crystal nucleation and growth.[78] Additionally, a series of proteins like BSA, R-chymotrypsin and lysozyme have been physically adsorbed to porous $CaCO_3$ microcrystals and studied as protein-delivery systems.[79]

Colloidal stability in biological medium is also recognized as an important parameter for drug delivery systems.[80] It is also known that a reduction of the particle concentration in the nanometer range due to colloidal instability can result in lower cytotoxicity profiles.[81] In Millipore water, nanometer and sub-micrometer $CaCO_3$ particles are well dispersed. However, micrometer vaterite particles did not yield stable suspensions as these large particles rapidly sediment. In DMEM, however, agglomeration and sedimentation is observed for all bare particle systems, due to the elevated ionic-strength of this medium and possibly due to adsorption of small molecules like sugars and amino acids present in DMEM. The increased ionic strength reduces both the Debye-Hückel length and the electro-static potential, hence the repulsive force between nanoparticles, which can lead to destabilization.[75] It must be pointed out that the presence of divalent ions in DMEM (1.8 mM of calcium ions) can also significantly contribute to the destabilization in the cell medium.[75] On the other hand, BSA-stabilized suspensions are more stable in DMEM according to PDI values. This can partially be explained by the steric stabilization provided by the bulky BSA molecules. Similar stabilization provided by proteins was previously reported.[36,82] Finally, regarding the relationship between crystalline phases and the colloidal stability, no apparent role can be observed. Since the zeta potential of all types of BSA-

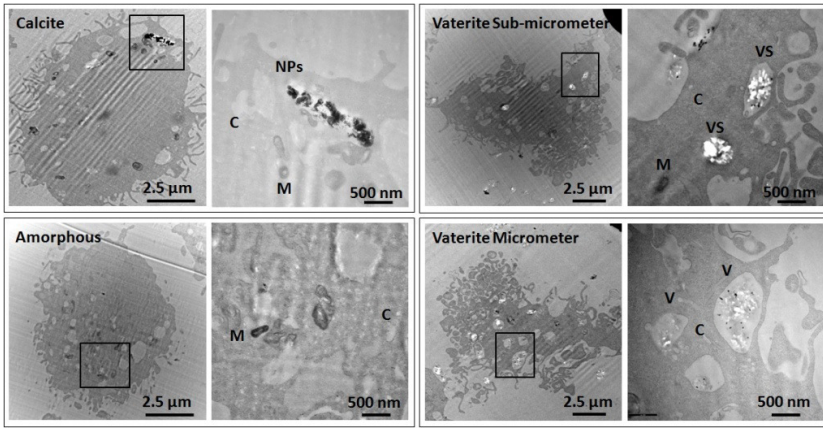


**Figure 8.6:** TEM of HOB cells incubated with calcite, amorphous, sub-micrometer and micrometer vaterite particles for 24 hours. Particle concentration: 0.3 g/L. Right panel is a high magnification image from selected area on left panel. Labels: C – cytosol, M - mitochondrion, NPs - calcite nanoparticles, VS – vaterite sub-micrometer particles, V – vaterite microparticles.

stabilized $CaCO_3$ particles was very similar, colloidal stability seems to be mostly dependent on particle size and ionic strength.

The dissolution behavior of each particle-system was determined in both Millipore water pH 7 and DMEM pH 7.4. As dissolution is dictated by the solubility product of each $CaCO_3$ phase, it can be expected that less thermodynamically stable phases are more soluble than other phases.[16,19] Accordingly, amorphous particles in water partially dissolved and a low increase in the calcium ion concentration was detected. Crystalline phases barely dissolved, and the difference in the dissolution behaviors of calcite and vaterite was not strongly pronounced at our experimental conditions. It is well-known that additional molecules in the medium, such as calcium chelators (particularly leucine, lysine and phosphate salts in DMEM, but also reported for citrates and EDTA in other buffers [19]) can significantly alter the phase equilibrium, which we experimentally observed for amorphous particles in DMEM. Amorphous particles readily dissolved in DMEM increasing the $[Ca^{2+}]$ in the medium. However, beneath the crystalline phases, the differences seem to be insignificant.

Toxicity experiments revealed that increased $[Ca^{2+}]$ concentration of around 2 to 6 mM can improve cell viability, which is a similar concentration range as was

reported elsewhere.[83] This behavior occurred for all three types of crystalline particles, but not for the amorphous particles, indicating that the observed increase in cell viability might be a result of cell internalization followed by lysosomal dissolution of the more stable $CaCO_3$ particles. For the amorphous particles, the release of the additive PAA, which was used to stabilize the amorphous phase, possibly caused membrane damage. Our findings are supported by [84], which described that PAA molecules (25 k mol/g) can actively disrupt cellular membrane of mammalian cells and cause cytotoxicity.

The TEM micrographs of HOB cells suggest that calcite and vaterite particles are internalized by the cells. In the micrometer range, the shape of $CaCO_3$ particles on the uptake by cervical carcinoma cells was studied.[63] It was suggested that the number of internalized particles is dependent on the aspect ratio of the particles. In regard to $CaCO_3$ in the nanometer scale, the uptake of nanoparticles by A549 cells was also observed.[36] However the role of crystallinity in the uptake has not yet been differentiated. Considering that all three particle-systems investigated here, apart from amorphous particles, were internalized, no clear dependency could be observed, regardless of size or crystallinity.

## 8.5. Conclusion

In summary, we examined four common types of dispersed calcium carbonate particles that are regularly studied as novel drug delivery systems and which might eventually find their way into health-related consumer products. Both crystallinity and environmental conditions (ionic strength, presence of proteins and chelators) play key roles in the colloidal behavior and phase-stability of $CaCO_3$ particles. However, since $CaCO_3$ is basically nontoxic and biocompatible, these aspects do not strongly affect their cellular response and toxicology profile. The behavior of the particles regarding their crystallinity, solubility and colloidal stability was evaluated by various standard methods for the characterization of nanomaterials and showed that the crystalline particles remained dispersed in solution, with no appreciable dissolution; however, the amorphous particles readily dissolved in the cell nutrition medium DMEM. It is worth mentioning that the sub-micrometer vaterite particles phase-transition into the more stable calcite phase accompanied by changes in particle size and shape. This change was only observed after 24 h and only for the smaller sub-micrometer vaterite particles. The addition of BSA generally improved colloidal stability in cell culture medium and diminished the rate of phase-transformation of the smaller vaterite particles. While the crystalline particles remained in solution with low release of calcium ions, the amorphous nanoparticles readily dissolved upon dispersion in DMEM, increasing the

extracellular $Ca^{2+}$ concentration. Two cellular responses were observed: increased mitochondrial activity induced by an internal increase of calcium ion concentration for crystalline particles, and cell death by membrane damage due to the presence of PAA in amorphous particles. Cellular uptake was observed for all crystalline particles, even the large micrometer-sized vaterite particles. Consequently, crystallinity, solubility and colloidal stability are key parameters for engineering $CaCO_3$ nanomaterials for biological applications and should also be factored into all assessments of the feasibility of new drug delivery systems.

## 8.6. Acknowledgement

We thank James Ziemah for assistance in the preparatory work and the Research Training Group GRK 1860, 'Micro-, meso- and macroporous nonmetallic materials: fundamentals and applications' (MIMENIMA) for funding.

## 8.7. References

This chapter was adapted from: Lauth, V., M. Maas,* and K. Rezwan. "An evaluation of colloidal and crystalline properties of $CaCO_3$ nanoparticles for biological applications, 2017, 78, 305–314" Materials Science and Engineering: C (2017). License number: **4085800483180**.

The article is mainly based on the work of the first author and the author of this thesis Victor Rafael Lauth. The precise contributions of each author are listed below.

| Author | Contribution |
|---|---|
| Lauth, V. | Conceptualization of the work, design and implementation of experiments, data collection, analysis and interpretation, principle writing of the manuscript and revision of the article |
| Maas, M.* | Conceptualization of the work, data analysis, writing, and revision of the manuscript. |
| Rezwan, K. | Gave conceptual advices and input, critical assessment of all experiments and revision of the manuscript. |

1. R. Kessler, *Environ. Health Perspect.*, 2011, **119**, 246–253.

2. R. Foldbjerg, X. Jiang, T. Miclăuş, C. Chen, H. Autrup and C. Beer, *Toxicol. Res.*, 2015, **4**, 563–575.

3. B. S. Sekhon, *Nanotechnol. Sci. Appl.*, 2010, **3**, 1–15.

4. D. Peer, J. M. Karp, S. Hong, O. C. Farokhzad, R. Margalit and R. Langer, *Nat. Nanotechnol.*, 2007, **2**, 751–760.

5. E. Blanco, H. Shen and M. Ferrari, *Nat. Biotechnol.*, 2015, **33**, 941–951.

6. E. Lepeltier, L. Nuhn, C.-M. Lehr and R. Zentel, *Nanomedicine (Lond).*, 2015, **10**, 3147–3166.

7. H. F. Krug, *Angew. Chemie - Int. Ed.*, 2014, **53**, 12304–12319.

8. F. Lebre, C. H. Hearnden and E. C. Lavelle, *Adv. Mater.*, 2016, 5525–5541.

9. K. P. García, K. Zarschler, L. Barbaro, J. A. Barreto, W. O'Malley, L. Spiccia, H. Stephan and B. Graham, *Small*, 2014, **10**, 2516–2529.

10. H. F. Krug and P. Wick, *Angew. Chemie*, 2011, **123**, 1294–1314.

11. T. Shen, Y. Zhang, A. M. Kirillov, B. Hu, C. Shan, W. Liu and Y. Tang, *J. Mater. Chem. B*, 2016, **4**, 7832–7844.

12. F. Konrad, F. Gallien, D. E. Gerard and M. Dietzel, *Cryst. Growth Des.*, 2016, **16**, 6310–6317.

13. Z. Zou, L. Bertinetti, Y. Politi, A. C. S. Jensen, S. Weiner, L. Addadi, P. Fratzl and W. J. E. M. Habraken, *Chem. Mater.*, 2015, **27**, 4237–4246.

14. R. K. Pai, S. Pillai, J. Ihli, W. C. Wong, E. H. Noel, Y.-Y. Kim, A. N. Kulak, H. K. Christenson, M. J. Duer and F. C. Meldrum, *CrystEngComm*, 2014, **5**, 3169.

15. V Radha, T. Z. Forbes, C. E. Killian, P. U. P. a Gilbert and A. Navrotsky, *Proc. Natl. Acad. Sci. U. S. A.*, 2010, **107**, 16438–16443.

16. L. N. Plummer and E. Busenberg, *Geochim. Cosmochim. Acta*, 1982, **46**, 1011–1040.

17 M. Auffan, J. Rose, J.-Y. Bottero, G. V Lowry, J.-P. Jolivet and M. R. Wiesner, *Nat. Nanotechnol.*, 2009, **4**, 634–41.

18. M. P. Monopoli, C. Åberg, A. Salvati and K. A. Dawson, *Nat. Nanotechnol.*, 2012, **7**, 779–786.

19. K. Sawada, *Pure Appl. Chem.*, 1997, **69**, 921–928.

20. F. Meder, S. S. Thomas, L. W. Fitzpatrick, A. Alahmari, S. Wang, J. G. Beirne, G. Vaz, G. Redmond and K. A. Dawson, *ACS Nano*, 2016, **10**, 4660–4671.

21. A. Wang, Y. Yang, X. Zhang, X. Liu, W. Cui and J. Li, *Chempluschem*, 2016, **81**, 194–201.

22. Q. Dong, J. Li, L. Cui, H. Jian, A. Wang and S. Bai, *Colloids Surfaces A Physicochem. Eng. Asp.*, 2017, **516**, 190–198.

23. T. N. Borodina, D. B. Trushina, I. V. Marchenko and T. V. Bukreeva, *Bionanoscience*, 2016, **6**, 261–268.

24. E. Tolba, W. E. G. Müller, B. M. Abd El-Hady, M. Neufurth, F. Wurm, S. Wang, H. C. Schröder and X. Wang, *J. Mater. Chem. B*, 2016, **4**, 376–386.

25. J. Zhang, Y. Li, H. Xie, B.-L. Su, B. Yao, Y. Yin, S. Li, F. Chen and Z. Fu, *ACS Appl. Mater. Interfaces*, 2015, **7**, 15686–15691.

26. N. Qiu, H. Yin, B. Ji, N. Klauke, A. Glidle, Y. Zhang, H. Song, L. Cai, L. Ma, G. Wang, L. Chen and W. Wang, *Mater. Sci. Eng. C*, 2012, **32**, 2634–2640.

27. Y. Guo, W. Jia, H. Li, W. Shi, J. Zhang, J. Feng and L. Yang, *J. Mater. Chem. B*, 2016, **4**, 5650–5653.

28. A. Neira-Carrillo, E. Yslas, Y. A. Marini, P. Vásquez-Quitral, M. Sánchez, A. Riveros, D. Yáñez, P. Cavallo, M. J. Kogan and D. Acevedo, *Colloids Surfaces B Biointerfaces*, 2016, **145**, 634–642.

29. Y. Zhao, Y. Lu, Y. Hu, J.-P. Li, L. Dong, L.-N. Lin and S.-H. Yu, *Small*, 2010, **6**, 2436–42.

30. Y. Guo, J. Zhang, L. Jiang, X. Shi, L. Yang, Q. Fang, H. Fang, K. Wang and K. Jiang, *Chem. Commun. (Camb).*, 2012, **48**, 10636–8.

31. V. Lauth, B. Loretz, C. M. Lehr, M. Maas and K. Rezwan, *Chem. Mater.*, 2016, **28**, 3796–3803.

32. G. Begum, T. N. Reddy, K. P. Kumar, K. Dhevendar, S. Singh, M. Amarnath, S. Misra, V. K. Rangari and R. K. Rana, *ACS Appl. Mater. Interfaces*, 2016.

33. W. Wei, G.-H. Ma, G. Hu, D. Yu, T. McLeish, Z.-G. Su and Z.-Y. Shen, *J. Am. Chem. Soc.*, 2008, **130**, 15808–10.

34. D. J. Park, K. H. Min, H. J. Lee, K. Kim, I. C. Kwon, S. Y. Jeong and S. C. Lee, *J. Mater. Chem. B*, 2016, **4**, 1219–1227.

35. K. H. Min, H. S. Min, H. J. Lee, D. J. Park, J. Y. Yhee, K. Kim, I. C. Kwon, S. Y. Jeong, O. F. Silvestre, X. Chen, Y. Hwang, E. Kim, S. C. Lee and M. I. N. E. T. Al, *ACS Nano*, 2015, **9**, 134–145.

36. M. Horie, K. Nishio, H. Kato, S. Endoh, K. Fujita, A. Nakamura, S. Kinugasa, Y. Hagihara, Y. Yoshida and H. Iwahashi, *Chem. Biol. Interact.*, 2014, **210**, 64–76.

37. A. Som, R. Raliya, L. Tian, W. Akers, J. Ippolito, S. Singamaneni, P. Biswas and S. Achilefu, *Nanoscale*, 2016, **8**, 12639–12647.

38. A. Shafiu Kamba, M. Ismail, T. A. Tengku Ibrahim and Z. A. B. Zakaria, *Biomed Res. Int.*, 2013, **2013**, 1–10.

39. J. A. Lee, M. K. Kim, H. M. Kim, J. K. Lee, J. Jeong, Y. R. Kim, J. M. Oh and S. J. Choi, *Int. J. Nanomedicine*, 2015, **10**, 2273–2293.

40. M. S. Jeong, H. S. Cho, S. J. Park, K. S. Song, K. S. Ahn, M. H. Cho and J. S. Kim, *Food Chem. Toxicol.*, 2013, **62**, 308–317.

41. F. Tewes, O. L. Gobbo, C. Ehrhardt and A. M. Healy, *ACS Appl. Mater. Interfaces*, 2016, **8**, 1164–1175.

42. J. Li, H. Jiang, X. Ouyang, S. Han, J. Wang, R. Xie, W. Zhu, N. Ma, H. Wei and Z. Jiang, *ACS Appl. Mater. Interfaces*, 2016, **8**, 30027–30036.

43. Y. I. Svenskaya, A. M. Pavlov, D. A. Gorin, D. J. Gould, B. V. Parakhonskiy and G. B. Sukhorukov, *Colloids Surfaces B Biointerfaces*, 2016, **146**, 171–179.

44. T. Cheang, S. Wang, Z. Hu, Z. Xing, G. Chang, C. Yao, Y. Liu, H. Zhang and A.-W. Xu, *J. Mater. Chem.*, 2010, **20**, 8050–8055.

45. J. Wei, T. Cheang, B. Tang, H. Xia, Z. Xing, Z. Chen, Y. Fang, W. Chen, A. Xu, S. Wang and J. Luo, *Biomaterials*, 2013, **34**, 1246–1254.

46. C. Qi, Y. J. Zhu and F. Chen, *ACS Appl. Mater. Interfaces*, 2014, **6**, 4310–4320.

47. Y. Zhao, Z. Luo, M. Li, Q. Qu, X. Ma, S. Yu and Y. Zhao, *Angew. Chemie - Int. Ed.*, 2015, **54**, 919–922.

48. Y. Zhao, L. N. Lin, Y. Lu, S. F. Chen, L. Dong and S. H. Yu, *Adv. Mater.*, 2010, **22**, 5255–5259.

49. Z. Dong, L. Feng, W. Zhu, X. Sun, M. Gao, H. Zhao, Y. Chao and Z. Liu, *Biomaterials*, 2016, **110**, 60–70.

50. X. Ying, C. Shan, K. Jiang, Z. Chen and Y. Du, *RSC Adv.*, 2014, **4**, 10841–10844.

51. J. D. Snook, C. B. Chesson, A. G. Peniche, S. M. Dann, A. Paulucci, I. V. Pinchuk and J. S. Rudra, *J. Mater. Chem. B*, 2016, **4**, 1640–1649.

52. D. Liu, G. Jiang, W. Yu, L. Li, Z. Tong, X. Kong and J. Yao, *Mater. Lett.*, 2017, **188**, 263–266.

53. J. Lee, H.-S. Min, D. G. You, K. Kim, I. C. Kwon, T. Rhim and K. Y. Lee, *J. Control. Release*, 2016, **223**, 197–206.

54. X. He, T. Liu, Y. Chen, D. Cheng, X. Li, Y. Xiao and Y. Feng, *Cancer Gene Ther.*, 2008, **15**, 193–202.

55. S. Chen, D. Zhao, F. Li, R.-X. Zhuo and S.-X. Cheng, *RSC Adv.*, 2012, **2**, 1820–1826.

56. S. K. Kim, M. B. Foote and L. Huang, *Cancer Lett.*, 2013, **334**, 311–8.

57. S. Chen, F. Li, R.-X. Zhuo and S.-X. Cheng, *Mol. Biosyst.*, 2011, **7**, 2841–7.

58. D. Zhao, R.-X. Zhuo and S.-X. Cheng, *Mol. Biosyst.*, 2012, **8**, 3288–94.

59. C.-Q. Wang, J.-L. Wu, R.-X. Zhuo and S.-X. Cheng, *Mol. Biosyst.*, 2014, **10**, 672–8.

60. J.-L. Wu, C.-Q. Wang, R.-X. Zhuo and S.-X. Cheng, *Colloids Surfaces B Biointerfaces*, 2014, **123**, 498–505.

61. J.-L. Wu, X.-Y. He, P.-Y. Jiang, M.-Q. Gong, R.-X. Zhuo and S.-X. Cheng, *RSC Adv.*, 2016, **6**, 69083–69093.

62. F. Kong, H. Zhang, X. Zhang, D. Liu, D. Chen, W. Zhang, L. Zhang, H. A. Santos and M. Hai, *Adv. Funct. Mater.*, 2016, **26**, 6158–6169.

63. B. V. Parakhonsky, M. Zyuzin, A. M. Yashchenok, S. Carregal-romero, J. Rejman, H. Möhwald, W. J. Parak and A. Skirtach, *J Nanobiotechnol*, 2015, **13**, 13–53.

64. S. Huang, J. C. Chen, C. W. Hsu and W. H. Chang, *Nanotechnology*, 2009, **20**, 375102.

65. M.-K. Kim, J.-A. Lee, M.-R. Jo, M.-K. Kim, H.-M. Kim, J.-M. Oh, N. Song and S.-J. Choi, *Nanomaterials*, 2015, **5**, 1938–1954.

66. M. Björnmalm, M. Faria and F. Caruso, *J. Am. Chem. Soc.*, 2016, **138**, 13449–13456.

67. V. Lauth, M. Maas and K. Rezwan, *J. Mater. Chem. B*, 2014, **2**, 7725–7731.

68. B. V. Parakhonskiy, A. Haase and R. Antolini, *Angew. Chemie Int. Ed.*, 2012, **51**, 1195–1197.

69. D. B. Trushina, T. V. Bukreeva and M. N. Antipina, *Cryst. Growth Des.*, 2016, **16**, 1311–1319.

70. M. Cocquyt, B. Pinchasik, D. Khalenkow, H. Mo, M. Konrad and A. Skirtach, *ACS Appl. Mater. Interfaces*, 2016, **8**, 14284–14292.

71. S. Shahabi, S. Döscher, T. Bollhorst, L. Treccani, M. Maas, R. Dringen and K. Rezwan, *ACS Appl. Mater. Interfaces*, 2015, **7**, 26880–26891.

72. K. Apte, R. Stick and M. Radmacher, *J. Mol. Recognit.*, 2017, **30**, 1–11.

73. P. Kaempfe, V. R. Lauth, T. Halfer, L. Treccani, M. Maas and K. Rezwan, *J. Am. Ceram. Soc.*, 2013, **96**, 736–742.

74. V. Vergaro, P. Papadia, S. Leporatti, S. A. De Pascali, F. P. Fanizzi and G. Ciccarella, *J. Inorg. Biochem.*, 2015, **153**, 284–292.

75. C. Graf, Q. Gao, I. Schütz, C. N. Noufele, W. Ruan, U. Posselt, E. Korotianskiy, D. Nordmeyer, F. Rancan, S. Hadam, A. Vogt, J. Lademann, V. Haucke and E. Rühl, *Langmuir*, 2012, **28**, 7598–7613.

76. L. B. Gower and D. J. Odom, *J. Cryst. Growth*, 2000, **210**, 719–734.

77. J. S. Evans, *CrystEngComm*, 2013, **15**, 8388–8394.

78. H.-B. Yao, J. Ge, L.-B. Mao, Y.-X. Yan and S.-H. Yu, *Adv. Mater.*, 2014, **26**, 163–188.

79. A. I. Petrov, D. V Volodkin and G. B. Sukhorukov, *Biotechnol. Prog.*, 2005, **21**, 918–25.

80. T. L. Moore, L. Rodriguez-Lorenzo, V. Hirsch, S. Balog, D. Urban, C. Jud, B. Rothen-Rutishauser, M. Lattuada and A. Petri-Fink, *Chem. Soc. Rev.*, 2015, **44**, 6287–6305.

81. N. Nafee, M. Schneider, U. F. Schaefer and C.-M. Lehr, *Int. J. Pharm.*, 2009, **381**, 130–9.

82. M. Horie, K. Nishio, K. Fujita, H. Kato, S. Endoh, M. Suzuki, A. Nakamura, A. Miyauchi, S. Kinugasa, K. Yamamoto, H. Iwahashi, H. Murayama, E. Niki and Y. Yoshida, *Toxicol. Vitr.*, 2010, **24**, 1629–1638.

83. S. Maeno, Y. Niki, H. Matsumoto, H. Morioka, T. Yatabe, A. Funayama, Y. Toyama, T. Taguchi and J. Tanaka, *Biomaterials*, 2005, **26**, 4847–4855.

84. C. Kusonwiriyawong, P. Van De Wetering, J. A. Hubbell, H. P. Merkle and E. Walter, *Eur. J. Pharm. Biopharm.*, 2003, **56**, 237–246.

# 9. Conclusion and perspectives

In this dissertation, significant effort has been devoted to the synthesis of $CaCO_3$ particles with controlled shape and size. To this end, the theories that govern the complex coacervation and biomineralization processes are modified to allow the production of particles with tailored physical properties. As these particles are intended for drug delivery applications, encapsulation assessments of proteins and fluorescent dyes are performed along with colloidal- and phase- stability studies in cell nutrition media. In addition, to estimate the toxic behavior and cellular internalization, the particles are assessed in vitro with two different cell lines.

The first study focused on the control of particle size and the ability to encapsulate proteins. As reported, the modified complex coacervation method is suitable for encapsulation of positively charged biomolecules, however the control of particle size is limited. As the complex coacervation phenomenon is based on the electrostatic interaction, charged proteins are shown to comprise one of the assembling components along with calcium ions and poly(acrylic acid) (PAA). Positively-charged lysozyme is shown to strongly coordinate with PAA, being highly incorporated into the coacervate phase. Considering the high protein loading, the coacervate size increases to 900 nm and can no longer be fully tailored by the complexation time. When tested with negatively-charged bovine serum albumin (BSA), due to repulsion with the negatively charged PAA, BSA is encapsulated at low concentrations and allows for good control of particle size similarly to unloaded coacervate droplets. Considering these features, the coacervate-directed method presents a cost-effective, easy to scale-up way to synthesize pH-responsive carriers that can be potentially used in gene and drug delivery.

Another synthesis method reported in the thesis is the template-assisted method, which uses poly(acrylic acid) as an additive and highly-carboxylated carbon dots (CDs) as templates for the mineralization of calcium carbonate. This technique allows the synthesis of particles with tailorable anisotropy in the sub-micrometer range. As a result of the high concentration of carboxylic groups provided by the additives, the bulk solution is depleted of free calcium ions by $Ca^{2+}$-carboxyl coordination. This coordination avoids both the direct precipitation of crystals in solution and allows the heterogeneous nucleation of $CaCO_3$ at the template surface. The particles self-assemble in either spheres or rods depending on the PAA concentration. Accordingly, the ability to adjust the particle geometry while still

maintaining appropriate size and encapsulation ability highlights the potential use as delivery vehicles to biological systems.

With biological applications in mind, the third study relates the role of size, morphology and crystallinity on the cellular response. In this context, commonly reported particle systems are characterized in terms of stability in medium. It is shown that the thermodynamically stable calcite particles maintain their morphological features as no phase transformation occurs. However, the sub-micrometer vaterite particles displayed a time- and size-dependent phase transformation to calcite. This transformation is effectively inhibited by the stabilization with albumin. In regard to the cellular response of human osteoblasts, it is reported that the particle uptake is not particle dependent, as all particles were internalized. Moreover, the viability assessment is shown to be dependent on the release of calcium ions by the particles. The partial dissolution of the carriers increased the extracellular and, probably, the intracellular calcium concentration in medium, which improved the viability. At the same time, the dissolution of amorphous particles released PAA and showed high levels of toxicity.

Accordingly, these studies present plenty of opportunities for further optimization. Given the aforementioned ability to modify the physical properties of calcium carbonate carriers, their use should not just be limited to drug delivery. This material is especially interesting in biological systems that respond to $Ca^{2+}$ ions. In bone regeneration for example, scaffolds could incorporate calcium carbonate particles. Upon dissolution, these particles provide a boost in the environment's calcium concentration. As calcium ions are known to regulate the cell cycle, this may offer an opportunity for osteoblast and osteoclast cell lines stimulation and improved bone regeneration. In addition, therapeutic ingredients can be encapsulated within the $CaCO_3$ particles and sustained release.

The complex coacervation method also offers opportunities for improvement. In our complex coacervation system, the choice of the acidic polyelectrolyte is based on a previous report that utilizes poly(acrylic acid). However, the cellular experiments showed that this polymer promoted cellular toxicity at 1.9 g/L when tested with osteoblast cell line. Possibly, the utilization of a more biocompatible polymer, like polyphosphate, may still allow phase-separation with the added benefit of improved morphogenetic activity on bone cells.

In the case of template-assisted assembly, there is the possibility of utilizing different templates. In this system, fluorescent carbon dots could be substituted by superparamagnetic iron oxide, anti-microbial nanodiamonds, or even a combination of more than one template type to create a multifunctional carrier.

Regarding the cellular studies, some critical aspects still have to be addressed. In vitro studies are very limited in their own context, as just a fraction of all possible nanoparticle-cellular interactions can occur in such model studies. Therefore, there is still doubt as to whether the reported in vitro behavior will hold true when performed in a living organism. In a more general sense, this is the central debate on nanoscience, in which, there still marginal improvement to the therapeutic outcome of clinical diseases despite 3 decades of research. To address this issue, studies should be devoted to the transition to in vivo experiments, up-scaling studies, to the improvement of active targeting moieties and in the design of more accurate computer simulations.

# 10. Appendix

## 10.1. Supporting information Chapter 2

The solubility of weak acids is very dependent on the pH. If the hydrolyses of carbonate is considered, the following equilibrium equations allow the calculation of the solubility of calcium carbonate as a function of pH:

$$CaCO_3 \overset{\text{Ksp}}{\longleftrightarrow} [\text{Ca}^{2+}] + [CO_3^{2-}] \quad \text{Eq. 7}$$

$$[H_2CO_3] \overset{\text{Ka1}}{\longleftrightarrow} [\text{H}^+] + [HCO_3^-] \quad \text{Eq. 8}$$

$$[HCO_3^-] \overset{\text{Ka2}}{\longleftrightarrow} [\text{H}^+] + [CO_3^{2-}] \quad \text{Eq. 9}$$

$$[H_2\text{O}] \overset{\text{Kw}}{\longleftrightarrow} [\text{H}^+] + [\text{OH}^-] \quad \text{Eq. 10}$$

$$[\text{Ca}^{2+}] = [CO_3^{2-}] + [HCO_3^-] + [H_2CO_3] \quad \text{Eq. 11}$$

$$[\text{Ca}^{2+}] = [CO_3^{2-}] + [CO_3^{2-}]\frac{[\text{H}^+]}{K_{a2}} + [CO_3^{2-}]\frac{[\text{H}^+]^2}{K_{a1}\,K_{a2}} \quad \text{Eq. 12}$$

$$[\text{Ca}^{2+}] = [CO_3^{2-}]\left(1 + \frac{[\text{H}^+]}{K_{a2}} + \frac{[\text{H}^+]^2}{K_{a1}\,K_{a2}}\right) \quad \text{Eq. 13}$$

$$[\text{Ca}^{2+}]^2 = [\text{Ca}^{2+}][CO_3^{2-}]\left(1 + \frac{[\text{H}^+]}{K_{a2}} + \frac{[\text{H}^+]^2}{K_{a1}\,K_{a2}}\right) \quad \text{Eq. 14}$$

$$[\text{Ca}^{2+}]^2 = K_{sp}\left(1 + \frac{[\text{H}^+]}{K_{a2}} + \frac{[\text{H}^+]^2}{K_{a1}\,K_{a2}}\right) \quad \text{Eq. 15}$$

$$S^2 = K_{sp}\left(1 + \frac{[\text{H}^+]}{K_{a2}} + \frac{[\text{H}^+]^2}{K_{a1}\,K_{a2}}\right) \quad \text{Eq. 2}$$

## 10.2. Supporting information Chapter 6

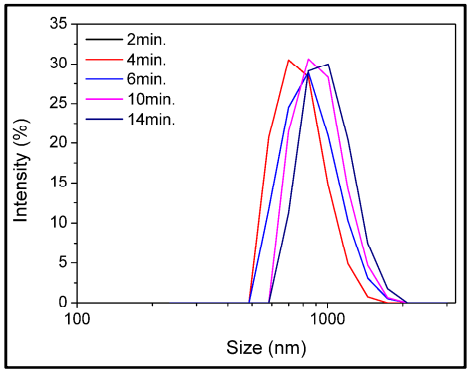


**Supporting Figure 6.1:** Size-distribution of the native coacervate droplets at different complexation time points. The tail is located at the large diameter side of the curve, which suggests the coalescence grow mechanism.

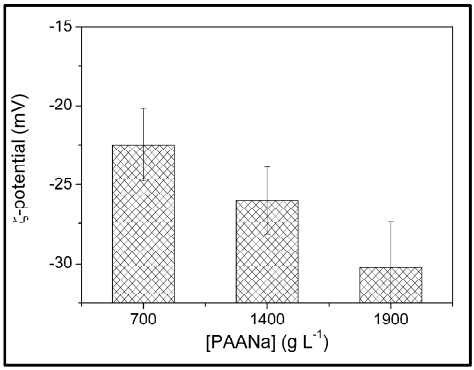


**Supporting Figure 6.2:** Zeta-potential of coacervates droplets at pH 9. The zeta-potential decreases with the increase of negatively charged PAA.

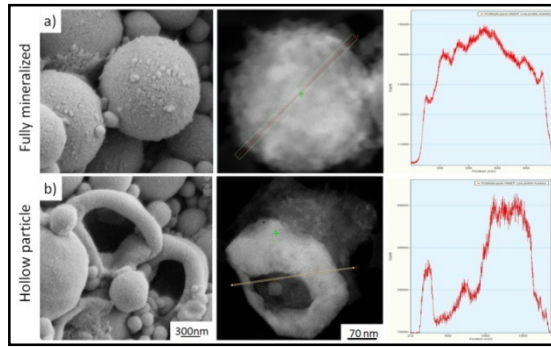


**Supporting Figure 6.3:** SEM, TEM and HAADF-STEM of fully mineralized microcarriers (a) and hollow capsules (b).

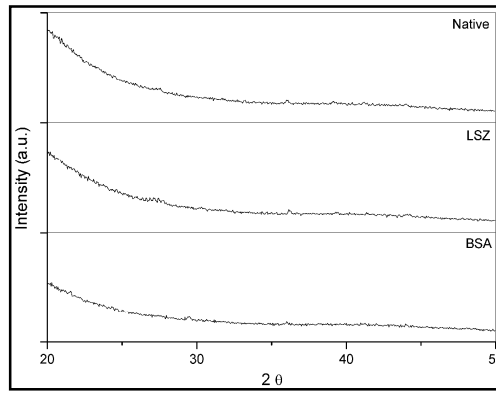


**Supporting Figure 6.4:** Comparison of X-ray diffraction patterns of native, BSA and LSZ-loaded microcarriers.

## 10.3. Supporting information Chapter 7

**Supporting Information 7.1:** Composition of Hank's balanced salt solution (HBSS).

| Ingredient | Concentration |
|---|---|
| NaCl | 136.90 mM |
| KCl | 5.40 mM |
| $NaHCO_3$ | 4.26 mM |
| $Na_2HPO_4$ 7 $H_2O$ | 0.34 mM |
| $KH_2PO_4$ | 0.35 mM |
| Glucose | 5.50 mM |
| HEPES | 10.00 mM |
| $CaCl_2$ | 1.26 mM |
| $MgCl_2$ $6H_2O$ | 0.50 mM |
| $MgSO_4$ $7H_2O$ | 0.40 mM |

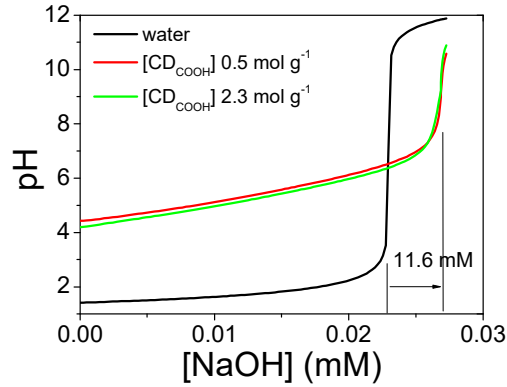


**Supporting Information 7.2:** Potentiometric titration of control (Millipore water), $[CD]_{COOH}$ 2.3 and $[CD]_{COOH}$ 0.5. For sample $[CD]_{COOH}$ 2.3, which carboxyl content is 11.6 mM, the yield is around 0.005 g/L. The carboxyl concentration can be calculated by diving these two values and results in 2.3 mol/g. Sample $[CD]_{COOH}$ 0.5, has the same 11.6 mM carboxyl content but much higher yield, 0.022 g/L, resulting in 0.5 mol/g $[CD]_{COOH}$. The solid content was measured by evaporating 1 mL of CD dispersion at 70°C for 3 days and weighting the resultant particles.

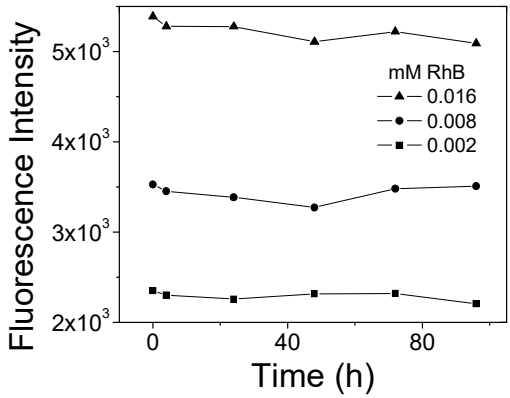


**Supporting information 7.3:** Fluorescence intensity of RhB as a function of time. For 96h the fluorescence intensity remained constant without appreciable variation.

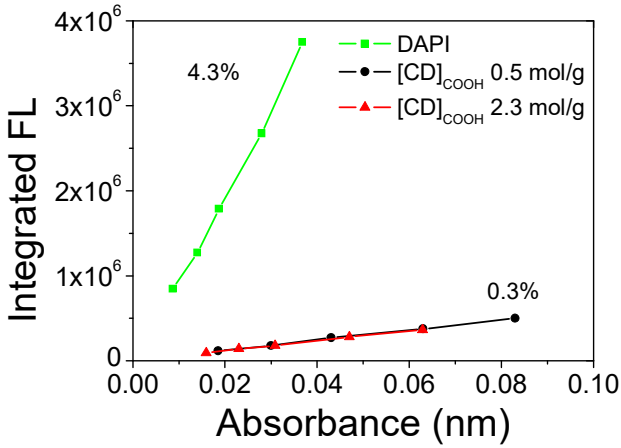


**Supporting information 7.4:** Quantum yield of both $[CD]_{COOH}$ 2.3 and 0.5 mol/g CDs in water when using DAPI as standard (~4%[1]).

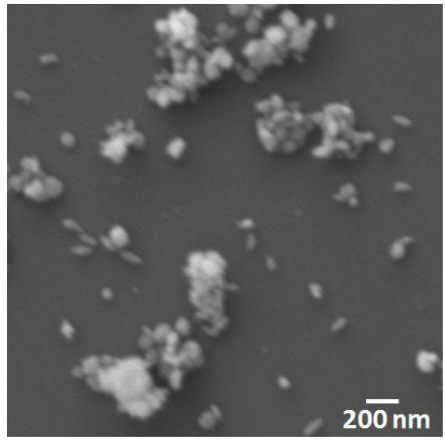


**Supporting information 7.5:** SEM of CD-$CaCO_3$ synthesized at 1.4 g/L PAA. Very small nanoparticles (under 90 nm) are stabilized by the high polymer concentration, which hinders aggregation.

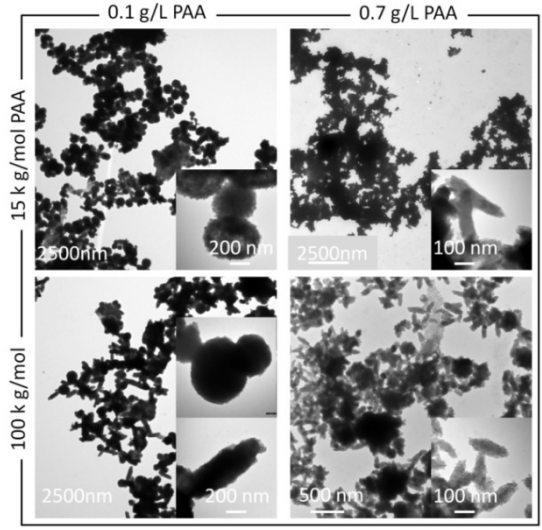


**Supporting information 7.6:** TEM micrographs as an overview of CD-$CaCO_3$ synthesized with 15k and 100k g/mol PAA at 0.15 and 0.7 g/L of PAA. Samples were mineralized using the $[CD]_{COOH}$ 2.3 g/mol.

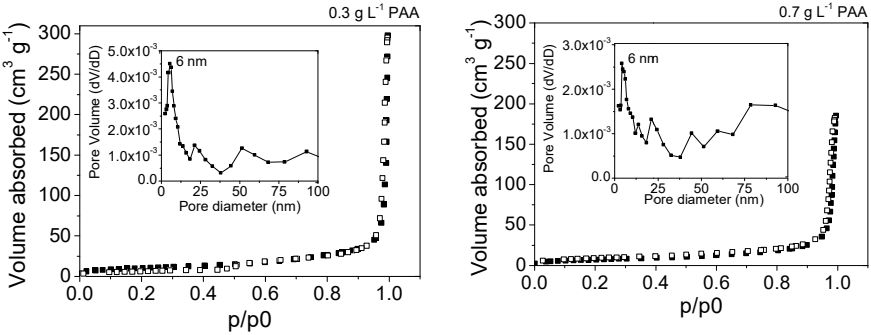


**Supporting information 7.7:** Nitrogen adsorption-desorption of 0.3 and 0.7 g/L PAA samples. Pore size distribution calculated by BJH shows a monomodal (about 6 nm) distribution of pores.

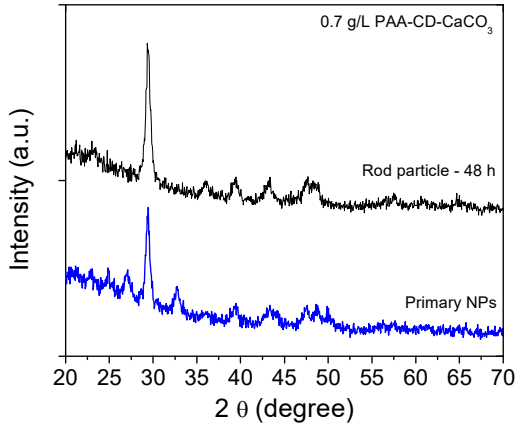


**Supporting information 7.8:** XRD patterns of PAA-CD-$CaCO_3$ immediately after synthesis and after 48 h. PAA concentration is 0.7 g/L.

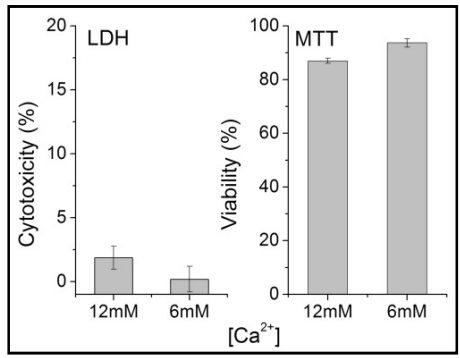


**Supporting information 7.9:** Evaluation of $Ca^{2+}$-induced cytotoxicity assessed by means of LDH and MTT assay.

**Additional reference:** (1) Li, M.; Wu, R. S.; Tsai, J. S. C. DAPI Derivative: A Fluorescent DNA Dye That Can Be Covalently Attached to Biomolecules. Bioorganic Med. Chem. Lett. 2003, 13, 4351–4354.

## 10.4. Supporting information Chapter 8

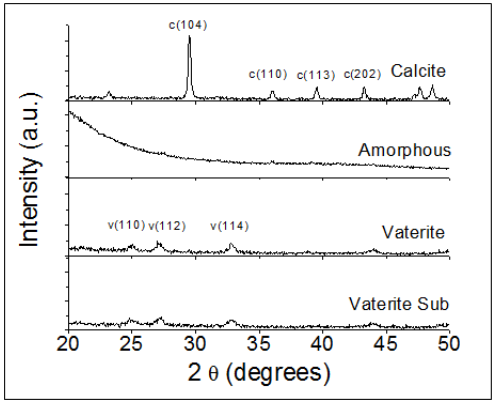


**Supporting Figure 8.1:** X-ray diffraction of calcite, amorphous, micrometer and sub-micrometer vaterite particles immediately after synthesis.

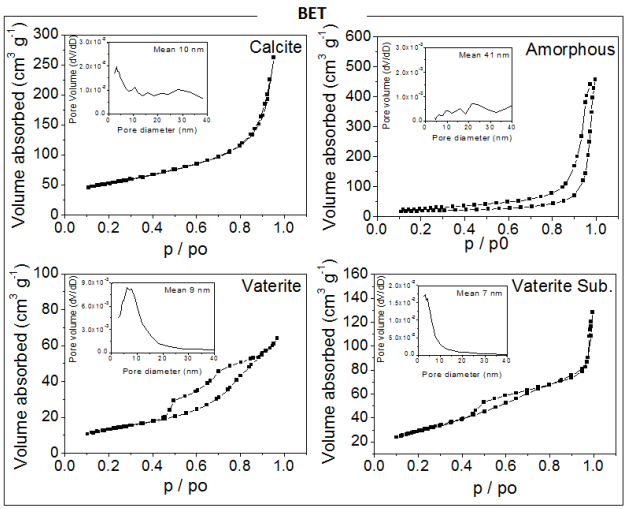


**Supporting Figure 8.2:** Nitrogen adsorption-desorption of calcite, amorphous, micrometer and sub-micrometer vaterite particles. Particles were dried for in absence of BSA overnight prior to the experiment. Inset: pore size distribution calculated by BJH.

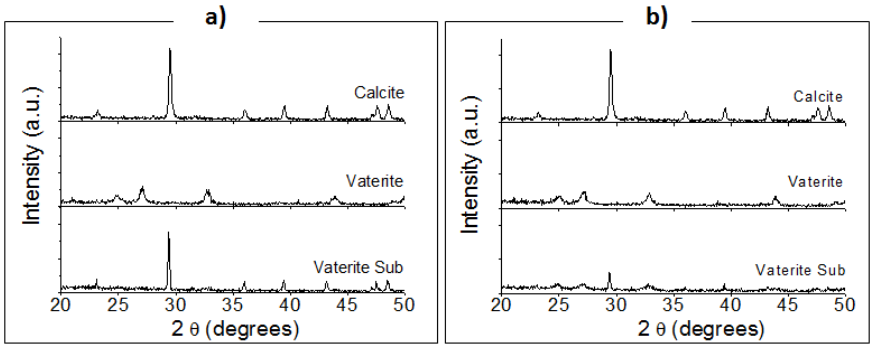


**Supporting Figure 8.3:** X-ray diffraction of calcite, vaterite micrometer and vaterite sub-micrometer particles after 96 hours incubation in DMEM. (a) bare particles in absence of BSA, (b) BSA-stabilized particles.

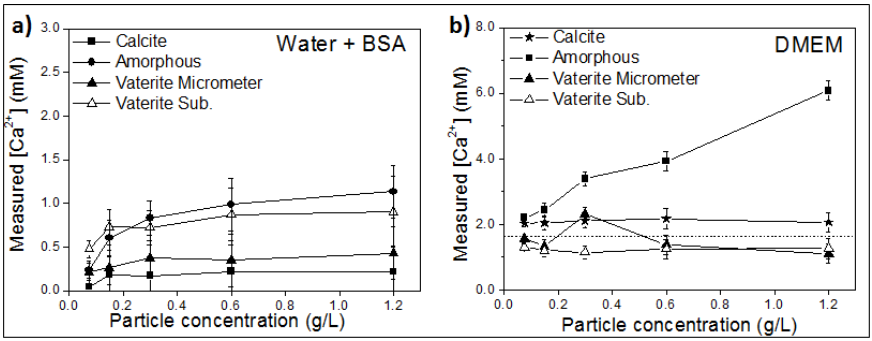


**Supporting Figure 8.4:** Dissolution of calcite, micro- and sub-micrometer vaterite and amorphous particles upon serial dilution in aqueous medium. (a) BSA-stabilized particles dispersed in Millipore water pH 7. (b) Bare particles dispersed in DMEM pH 7.4.

Protocol live/dead: HOB cells were seeded onto 6-well cell culture plates at a density of $2x10^4$ cells / mL in DMEM 10% FCS. After 24 h of incubation, the culture medium was replaced with 1 mL of BSA-stabilized particles with a particle concentration of 0.3 g/L in DMEM. After 24 h of incubation, the cells were washed with the PBS. A live/dead solution (5 mM Propidium Iodide (PI), 10 mM Hoechst 33342 in DMEM) was added and incubated for 15 min at 37 °C. The solution was removed and cells were washed twice with PBS. PI stains dead cells (red) while Hoechst live cells (blue).

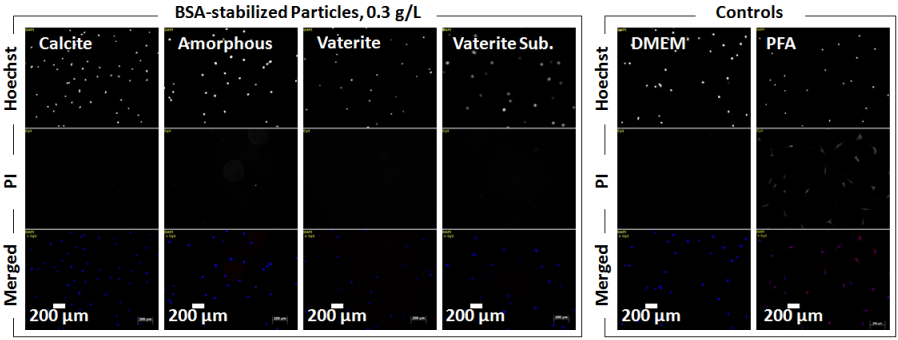


**Supporting Figure 8.5:** HOB cells stained with the live/dead assay kit after 24 hours incubation with calcite, amorphous, micrometer and sub-micrometer vaterite particles at particle concentration of 0.3 g/L. Left panel indicates the results obtained for positive control DMEM (incubation in DMEM without particles) and negative control PFA (fixation with paraformaldehyde, PFA). Live cells stained red by Hoechst and dead cells stained blue by propidium iodide (PI).

Protocol 2D staining:[1] After exposure to $CaCO_3$ particles, the HOB cells were rinsed twice with PBS, fixed for 15 min at RT with 4% PFA in PBS. After the washing steps, the cells were permeabilized with 0.5 % Triton X-100 in PBS for 3 min at RT. Fluorescent stain solution (DAPI 0.5 µg/mL, Phalloidin AF 488 10 µg/mL in PBS) was added to the cells, incubated for 45 min and rinsed a few times prior the microscopy. Positive control DMEM – cells incubation in DMEM and in the absence of particles. Negative control Triton – cells were incubated with triton.

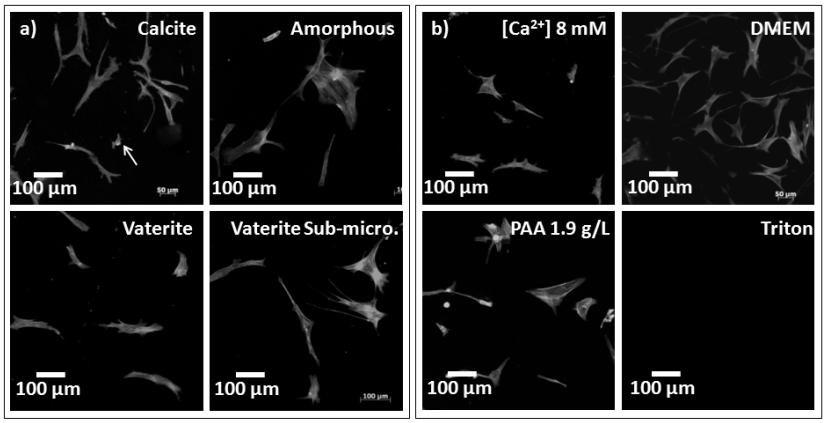


**Supporting Figure 8.6:** (a) 2D staining of HOB cells after 24 hours incubation with calcite, amorphous, micrometer and sub-micrometer vaterite particles at 0.3 g/L. (b) Controls: DMEM (positive control, incubation in DMEM without particles), Triton (negative control, cells treated with Triton X-100, 0.5%), high calcium levels (8 mM $CaCl_2$) and high PAA levels (1.9 g/L PAA).

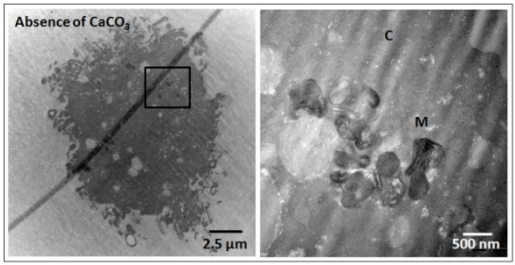


**Supporting Figure 8.7:** TEM of biological samples incubated in absence of particles for 24 h. Right panel is a high magnification image from selected area on left panel. Labels: C – cytosol, M - mitochondrion.

Protocol for intracellular calcium imaging with Fluo-3AM:[2] After exposure to $CaCO_3$, intracellular $Ca^{2+}$ was observed by fluorescence microscopy using Fluo 3-AM (1 mM in DMSO, ≥ 99.0 %, Sigma-Aldrich). A staining solution (10 µM Fluo 3-AM, 0.17 g/L Pluronic F127 (BioReagent, Sigma-Aldrich)) was added to the cells and incubated at 37 °C for 20 min. After incubation, DMEM 10% FCS was added to cells at the same volume as the staining solution, and incubated for 1 h at 37 °C. The cells were then washed once with PBS and observed at the microscope at Excitation 495 nm - Emission 519 nm. Control DMEM: absence of particles. Control Calcium 2 mM: DMEM supplemented with 2 mM $Ca^{2+}$.

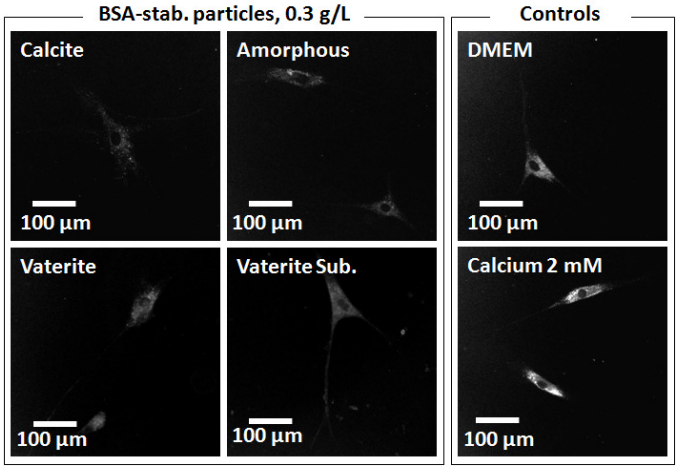


**Supporting figure 8.8:** Fluo-3AM imaging of intracellular calcium of HOB cells after 24 hours incubation with calcite, amorphous, micrometer and sub-micrometer vaterite particles at 0.3 g/L. Control DMEM: tested with DMEM in absence of particles. Control Calcium 2 mM: DMEM supplemented with 2 mM of calcium chloride.

**Additional references:**

1) S. Shahabi, S. Döscher, T. Bollhorst, L. Treccani, M. Maas, R. Dringen, K. Rezwan, Enhancing Cellular Uptake and Doxorubicin Delivery of Mesoporous Silica Nanoparticles via Surface Functionalization: Effects of Serum, ACS Appl. Mater. Interfaces. 7 (2015) 26880–26891.

2) M. Horie, K. Nishio, H. Kato, S. Endoh, K. Fujita, A. Nakamura, S. Kinugasa, Y. Hagihara, Y. Yoshida, H. Iwahashi, Evaluation of cellular influences caused by calcium carbonate nanoparticles, Chem. Biol. Interact. 210 (2014) 64–76.

## 10.5. List of students and projects

The following students were supervised during the doctoral studies and are here gratefully acknowledged.

| | |
|---|---|
| **Werner Augusto Schmidt**<br>Diploma thesis, 2014 | Study of complexation of poly(acrylic acid) with calcium based on the Donnan Model |
| **Kaio Gonçalves Pereira**<br>Diploma thesis, 2014 | Coacervate-directed mineralization of core/shell microcarriers for drug delivery applications |
| **Poku Oppong**<br>Master thesis, 2016 | Synthesis of calcium carbonate carriers based on the coacervate-directed method for controlled release of poorly soluble drugs |
| **Skrollan Beißbarth**<br>Bachelor thesis, 2016 | Synthese und Charakterisierung von funktionalisierten Nanopartikel- Komplexen |
| **Jennifer Muñoz**<br>Master thesis, 2016 | Biocompatible hydroxyapatite coatings deposited on $TiO_2$/SS302 substrates by HVOF |
| **James Ziemah**<br>Pre-master project, 2017 | The effect of polyols in the control of particle size and morphology of calcium carbonate |

## 10.6. Curriculum vitae

| | |
|---|---|
| Surname | Lauth |
| Name | Victor |
| Data and place of birth | December, 23rd 1989, Blumenau, Brazil |

**Education:**

| | |
|---|---|
| 02/2013 | Engineer's degree in Materials Engineering, Federal University of Santa Catarina - Florianópolis, Brazil |
| 12/2007 | Secondary school, Blumenau, Brazil |

**Professional and research experience:**

| | |
|---|---|
| 04/2013 – 05/2017 | Research assistant, Advanced Ceramics Group<br>University of Bremen, |
| 08/2012 – 02/2013 | Exchange student at Institute Advanced Ceramics<br>Hamburg University of Technology, Hamburg, Germany |
| 03/2012 – 08/2012 | Student assistant at CIMJECT<br>Federal University of Santa Catarina, Florianópolis, Brazil |

**Award and funding**

| | |
|---|---|
| 02/2013 | Diploma of Merit "Best average grade in Materials Engineering"<br>Awarded by Ministério da Educação, Brazil |
| 10/2013 – 11/2016 | Associate student of the research training group "Micro-, meso- and macroporous nonmetallic Materials: Fundamentals and Applications", Bremen, Germany |

## 10.7. List of publications

Kaempfe, P., **Lauth, V. R.**, Halfer, T., Treccani, L., Maas, M., & Rezwan, K. Micromolding of Calcium Carbonate Using a Bio-Inspired, Coacervation-Mediated Process. Journal of the American Ceramic Society, 2013, 96(3), 736-742. https://doi.org/10.1111/jace.12194

**Lauth, V.**, Maas, M., & Rezwan, K. Coacervate-directed synthesis of $CaCO_3$ microcarriers for pH-responsive delivery of biomolecules. Journal of Materials Chemistry B, 2014, 2(44), 7725-7731. https://doi.org/10.1016/j.msec.2017.04.037

Guglielmi, P. O., Blaese, D., Hablitzel, M. P., Nunes, G. F., **Lauth, V. R.**, Hotza, D., ... & Janssen, R. Microstructure and flexural properties of multilayered fiber-reinforced oxide composites fabricated by a novel lamination route. Ceramics International, 2015, 41(6), 7836-7846. https://doi.org/10.1016/j.ceramint.2015.02.120

**Lauth, V.**, Loretz, B., Lehr, C. M., Maas, M., & Rezwan, K. Self-Assembly and Shape Control of Hybrid Nanocarriers Based on Calcium Carbonate and Carbon Nanodots. Chemistry of Materials, 2016, 28(11), 3796-3803. http://dx.doi.org/10.1021/acs.chemmater.6b00769

**Lauth, V.**, Maas, M., & Rezwan, K. An evaluation of colloidal and crystalline properties of $CaCO_3$ nanoparticles for biological applications. Materials Science and Engineering: C, 2017, 78, 305-314. https://doi.org/10.1016/j.msec.2017.04.037

Salmoria, G. V., **Lauth, V. R.**, Cardenuto, M. R., & Magnago, R. F. Characterization of PA12/PBT specimens prepared by selective laser sintering. Optics & Laser Technology, 98, 2018, 92-96. https://doi.org/10.1016/j.optlastec.2017.07.044